Bangor University

DOCTOR OF PHILOSOPHY

Long-term morphological modelling of tidal basins

McCann, David

Award date:
2011

Awarding institution:
Bangor University

Link to publication

Long-term morphological modelling of tidal basins

Author:
David McCann

Supervisors:
Prof. Alan Davies
Prof. Colin Jago

A thesis submitted in accordance with the requirements of Bangor University for the degree of Doctor of Philosophy

University of Bangor
School of Ocean Sciences
Menai Bridge, Anglesey
Unitied Kingdom
LL59 5AB

October 2011

DECLARATION

This work has not been previously accepted in substance for any degree and is not being concurrently submitted in candidature for any degree.

Signed: . . . . (candidate)
Date: . . . .

STATEMENT 1

This thesis is the result of my own investigations, except where otherwise states. Other sources are acknowledged by footnotes giving explicit references. A bibliography is appended.

Signed: . . . . (candidate)
Date: . . . .

STATEMENT 2

I agree to deposit an electronic copy of my thesis (the Work) in the Bangor University (BU) Institutional Digital Repository, the British Library ETHOS system, and/or in any other repository authorized for use by Bangor University and where necessary have gained the required permissions for the use of third party material.

Signed: . . . . (candidate)
Date: . . . .

Abstract

Shallow coastal environments, particularly sandy tidal basins, are coming under increasing pressures due to human development and a changing climate. This has led to a demand for long-term predictions of sediment transport using deterministic, process-based coastal area models. Due to continually growing model complexity this has involved an increased computational cost, resulting in the development of a variety of methods to speed up computation time while having a minimal impact on model accuracy. The present body of work introduces one of the most popular speed-up methods, the Morphological Factor (MF) method, to the `TELEMAC` hydro-informatics modelling system.

Using the depth-averaged, shallow water hydrodynamic and sediment transport models, `TELEMAC 2D` and `SISYPHE` respectively, a long-term simulation of a schematised tidal basin system is conducted. From infinitesimal perturbations to an initially flat bed a highly regular morphological pattern is seen to evolve spontaneously through the processes of self-organisation, subsequently forming the basis of a dynamic and intricate tidal channel network. Due to the time-stepping nature of the model, the initial pattern is responsible for all future simulated morphologies, yet this linkage has received little attention in the literature. Further simulations identify the first stages of the bed pattern as a dissipative structure, requiring more energy from the flow to create and maintain than the initial flat bed itself, which is contradictory to a linear, mechanistic treatment of the system.

Dunes, sedimentary bed forms ubiquitous to the coastal zone, have a significant impact on flow speed (and therefore sediment transport and morphological change) through the roughness created by their geometry. Although the effects of dune-scale roughness on the flow and sediment transport are discussed in the literature the impact of a time-evolving roughness feedback between the bed and the flow in a coupled morphological model is poorly understood. In the present work a roughness feedback mechanism is implemented in `TELEMAC 2D` and `SISYPHE` and the predicted roughness is validated in a model of the Dyfi Estuary, Wales, using the results of a swathe sonar bathymetric survey. The model results show very promising agreement with the data given the simplifying assumptions made. The tidal residual sediment transport rate in a simplified model case is shown to not only change in magnitude, but also in sign, between cases with and without bed roughness feedback, showing that the method has significant implications for long-term morphological change.

Deterministic models are frequently used to predict changes in the long-term, yet their mechanistic nature forces the outcome to be sensitive to initial conditions. Natural systems, however, contain both deterministic and probabilistic elements that create structures and patterns at a variety of different scales, many of which can be captured by process based models such as `TELEMAC 2D` and `SISYPHE`. In the present work a stochastic, infinitesimal perturbation is introduced to three otherwise identical long-term model simulations, resulting in system divergence through three independent morphological system parameters. The sensitivity to initial conditions and the important role of self-organisation are seen to produce dynamic morphological behaviour that is inherent to the theory of open, dissipative systems.

Acknowledgments

I would like to thank my supervisor Prof. Alan Davies for all the years of support and gentle nudges in the right direction, without which this project would have never gotten far from the starting gun. Also thanks to my office companion Dr. Jonathan Malarkey for the endless chats and interrupting debates that kept everything in perspective and never ceased to provide new insights and avenues of investigation. The guidance of my supervisory panel (Prof. Colin Jago, Dr. Dei Huws and Dr. Jaco Baas) and Viva panel (Mr. Tim Chesher, Dr. Jaco Baas and Dr. Dave Bowers) are also gratefully noted.

The following data sources are gratefully acknowledged for contributing to this body of work: The National Oceanography Centre (NOC), Liverpool for the POLCOMS tidal constituent data (courtesy of S. Neill, Bangor), Tom Benson (H.R. Wallingford) for the ‘`telheadr`’ and ‘`telstepr`’ `Matlab` subroutines, Dr. Jim Bennell for the provision of swathe sonar bathymetric survey data (analysed by Dr. Richard Bates at the University of St. Andrews) and Dr. Peter Robins and Dr. Jennifer Brown for their Dyfi Estuary Grids and steering files that provided the basis for my model.

Finally, thanks to all the folks, friends and family alike, who have an impact on your work whether you (or they) know it or not.

This studentship was made possible by a grant from the Engineering and Physical Sciences Research Council (EPSRC). This body of work forms part of CCCR (Centre for Catchment & Coastal Research, part of the Aberystwyth University and Bangor University Research & Enterprise Partnership).

List of symbols

A	Tidal constituent amplitude	m
c	Advection velocity	ms^{-1}
C	Suspended sediment concentration	kgm^{-3}
C_D	Quadratic drag coefficient	—
C_{eq}	Equilibrium suspended sediment concentration	kgm^{-3}
C_{ref}	Suspended sediment concentration at height z_{ref}	kgm^{-3}
D	Deposition of sediment from suspension	m
D_{50}	Median sediment grain diameter	m
D_*	Non dimensional sediment grain diameter	—
E	Erosion of sediment into suspension	m
f_s	Granular coefficient	—
F_D	Drag force on a sediment grain	N
F_L	Lift force on a sediment grain	N
F_W	Submerged weight of a sediment grain	N
F_x	Momentum source and sink terms in the x direction	ms^{-2}
F_y	Momentum source and sink terms in the y direction	ms^{-2}
g	Acceleration due to gravity	ms^{-2}
G	Tidal constituent phase	rad
h	Total hydraulic flow depth	m
k	Wavenumber	radm^{-1}
k_s	Total bed roughness	m
$k_{s,d}$	Bed roughness due to dunes	m
$k_{s,m}$	Bed roughness due to megaripples	m
$k_{s,r}$	Bed roughness due to ripples	m
K_1	Principal Lunar diurnal tidal period	s
K_2	Lunisolar semidiurnal tidal period	s
M_2	Principal Lunar semidiurnal tidal period	s
M_4	Principal Lunar shallow water tidal period	s
n	Sediment bed porosity	—
O_1	Lunar diurnal tidal period	s
P_1	Solar diurnal tidal period	s
P_c	Channel pixel set	—
Q_1	Larger lunar elliptic diurnal tidal period	s
Q_b	Volumetric bed load sediment transport rate	m^2s^{-1}

Q_s	Volumetric total load sediment transport rate	m^2s^{-1}
Q_{ss}	Volumetric suspended load sediment transport rate	m^2s^{-1}
r	Circle radius	m
R	Uniformly distributed random number	—
R_{norm}	Normally distributed random number	—
s	Sediment relative density	—
S	Entropy	JK^{-1}
S_2	Principal Solar semidiurnal tidal period	s
t	Time	s
T	Absolute temperature	k
T_r	Tidal repeat period	s
u	Flow velocity in the x direction	ms^{-1}
u_*	Friction velocity direction	ms^{-1}
U	Depth-averaged flow velocity in the x direction	ms^{-1}
$\bar{U}$	Scalar depth-averaged flow velocity	ms^{-1}
U_{adv}	Scalar sediment advection velocity	ms^{-1}
U_{conv}	Sediment convection velocity in the x direction	ms^{-1}
v	Flow velocity in the y direction	ms^{-1}
V	Depth-averaged flow velocity in the y direction	ms^{-1}
V_{conv}	Sediment convection velocity in the y direction	ms^{-1}
w_s	Sediment settling velocity	ms^{-1}
W	Channel width	m
X_c	x component of the FFT wavelength spectrum centroid	m
Y_c	y component of the FFT wavelength spectrum centroid	m
z	Height above the bed	m
z'	Dimensionless height above the bed	—
z_0	Total bed roughness length	m
$z_{0,d}$	Bed roughness length due to dunes	m
$z_{0,m}$	Bed roughness length due to megaripples	m
$z_{0,r}$	Bed roughness length due to ripples	m
z_b	Bed elevation	m
z_{ref}	Reference height above the bed	m
z_s	Free surface elevation	m
α	Bed load flux direction relative to flow	deg
α_{tau}	Bed shear stress flux direction relative to flow	deg
β	Bed slope coefficient	—
γ	Along-flow coordinate	—

γ'	Across-flow coordinate	—
ϵ_s	Sediment diffusivity	m^2s^{-1}
η	Bed form height	m
θ	Shields parameter	—
θ'	Skin friction Shields parameter	—
θ_{cr}	Critical Shields parameter	—
κ	Von Karman's constant	—
λ	Bed form wavelength	m
ν	Fluid kinematic viscosity	m^2s^{-1}
ν_e	Momentum diffusion coefficient	m^2s^{-1}
ρ	Fluid density	kgm^{-3}
ρ_s	Sediment density	kgm^{-3}
σ	Tidal constituent frequency	rads^{-1}
τ	Shear stress	Nm^{-2}
τ_0	Bed shear stress	Nm^{-2}
τ_0'	Bed shear stress due to skin friction	Nm^{-2}
τ_0''	Bed shear stress due to form drag	Nm^{-2}
ϕ_s	Sediment angle of repose	deg
Φ_b	Non dimensional bed load transport rate	—
Φ_r	Non dimensional bed load transport rate due to stochastic θ_{cr}	—
ψ	Mobility parameter	—

Contents

6 Probabilism, history and divergent evolution in an open, dissipative system 103

7 Discussion 141

Chapter 1

Introduction

1.1 Background and rationale

With increased exploitation due to human industrial expansion and environmental pressures due to a changing climate and rising sea level, estuary and tidal basin research is gaining a growing amount of attention. Computer modelling, particularly at the coastal area-scale, has become one of the most important research tools available to coastal scientists and as such the development of process-based coastal modelling has developed significantly in recent decades.

Coastal area models operate by solving the equations of motion on a discrete grid that covers the area of interest. Physical parameters are then used to calculate various results such as the transport of sediment or the production of turbulence. Over time, these models have developed in accuracy of their predictions to the point where they are no longer tools of pure research but also used routinely for management and consultancy purposes in both the private and public domain. It is therefore of vital importance that the limits of process-based modelling are fully understood, not least because of the importance of the decisions that are made in light of their results.

The discrete nature of the computations central to numerical models results in a time-cost that scales on the size and complexity of the model grid and simulation length. There are numerous methods available to the numerical modeller to reduce this time-cost and therefore be able to make predictions of morphological evolution further into the future. The compatibility of a particular approach (the Morphological Factor method) with the `TELEMAC 2D` modelling package is assumed but previously untested.

Certain key physical parameters still remain to be fully included in coupled morphological models. The effect that sea bed roughness has on the flow is well known, yet a major component of bed roughness in much of the coastal zone (that due to sedimentary bed forms known as dunes) is not yet fully included in most models. The inclusion of a predicted roughness that varies in time and space to the hydrodynamic model is vital from a physical perspective but is difficult to validate, a problem that recent advances in field measurement techniques may provide the answer to.

Numerical modelling relies on computers that perform discrete operations in a deterministic, repeatable manner. Although this is a desirable property of numerical models it may not be entirely suited to the simulation of natural systems that contain both deterministic and probabilistic elements. It is also arguable that a purely deterministic system is predictable at all as the sensitivity of the model to initial conditions may completely alter the final outcome.

This thesis aims to answer three key research questions:

1. Can the finite element hydrodynamic and morphological modelling packages `TELEMAC 2D` and `SISYPHE` be used to simulate the long-term (i.e. 100 years) morphological evolution of a tidal basin?

2. What are the effects of introducing a more complete formulation for bed roughness prediction and feedback to `TELEMAC 2D` and `SISYPHE` and can the predictions be validated?

3. What are the effects of introducing probabilistic elements to a long-term morphological simulation and can these effects be measured and explained?

1.2 Thesis structure

Chapter 2 is a literature review introducing the field of morphological research modelling and some of the techniques pertaining to it.

Chapter 3 contains an introduction to morphological modelling within the environment of `TELEMAC 2D` and `SISYPHE`, including a description of the specific subroutines and modules employed within this body of work. A Brier Skill Score test is run on a pair of morphological simulations to ascertain the impact of the Morphological Factor method of bed update speed-up on simulation results, as well as a derivation for a stability criterion to address (and predict) the numerical instabilities found when using an Advection-Diffusion scheme for suspended sediment transport and the MF method.

The results from an initial 100 year morphological simulation are described in Chapter 4, highlighting the origin of a regular and robust spontaneously self-organised morphological pattern. The role of the initial morphology in the evolution of a complex tidal channel network is discussed using hydrodynamic and sedimentological results.

Chapter 5 introduces the problem of bed roughness feedback between `TELEMAC 2D` and `SISYPHE` and presents the results of a validation simulation and comparison with field data. The effect of bed roughness feedback on the magnitude of the calculated sediment transport rate is also discussed.

In Chapter 6 a stochastic implementation of the critical non-dimensional bed stress (the Shields parameter) is introduced into a bed load transport prediction equation and its subsequent effect on sediment transport bias discussed. The effect of random infinitesimal perturbations to otherwise identical systems is presented.

After a discussion of the results the final conclusions of the work are presented and future work is proposed to extend the research presented in this study.

Chapter 2

Literature review

2.1 Hydrodynamics for sediment transport

In the absence of waves, the vertical velocity profile (figure 2.1) of a free surface flow over a surface such as an erodible bed of sediment is often assumed to follow a logarithmic decay with depth (the so called 'law of the wall'). The flow speed u at a certain height above the bed z is found by

$$u(z) = \frac{u*}{\kappa} \ln \left(\frac{z}{z_0} \right) \tag{2.1}$$

where u^* is the friction velocity, κ is Von Karman's constant (equal to 0.4) and z_0 is the bed roughness length—the height above the bed at which velocity tends to zero. This is due to friction that creates shear stresses (τ) between vertical layers of the flow. z_0 can also be expressed as a Nikuradse roughness k_s, calculated as $z_0 = k_s/30$ (Soulsby, 1997). τ is a force per unit area (units of Nm^{-2}) which is generated by the transfer of momentum between two adjacent vertical layers of flow (Dyer, 1986). It follows that the highest stress (in this system of a steady current only) will occur between the stationary bed and the near bed flow—the total bed shear stress τ_0, defined as

$$\tau_0 = \rho u_*^2 \tag{2.2}$$

where ρ is the fluid density. The total bed shear stress is made up of contributions from the skin friction bed shear stress τ_0' (produced by and acting on the bed sediment grains) and the form drag shear stress τ_0'', produced by the varying pressure field around bed topography (Soulsby, 1997). The small-scale roughness contribution τ_0' is primarily important for sediment transport as it is this stress that is 'felt' by discrete grains on the bed. The stress τ_0'' induced by small-scale bed topography (ripples) can also effect sediment transport however, through its effect on near-bed flow. The shear velocity u^* can also be found from the slope of the line $u(ln[z])$. The profile of shear stress with depth is (in the absence of any stress at the free surface, e.g. from wind) assumed to be linear, with a maximum at the bed of $\tau = \tau_0$ and a minimum at the free surface of zero, so that

$$\tau(z) = \tau_0 \,(1 - z/h) \tag{2.3}$$

where h is the depth of the flow, measured from the elevation of the free surface z_s to the elevation of the bed z_b.

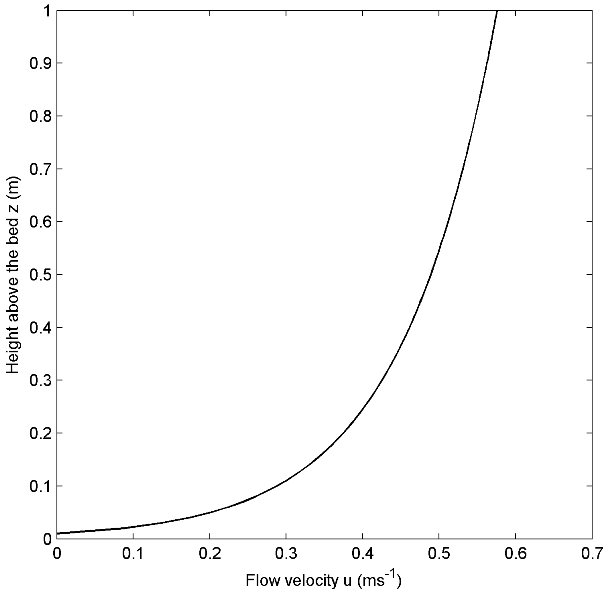

Figure 2.1 – The logarithmic profile of flow velocity with depth. The velocity tends to zero as $z \to z_0$ due to friction between the flow and the bed.

The sea bed is, more often than not, comprised of erodible sediments. In shallow coastal seas and tidal basins such as estuaries the bed sediment is often formed of quartz sands of varying grain diameters. Assuming the grains to have a spherical form, Shields (1936) studied the forces acting on bed sediments from the flow. The result was the Shields parameter θ which is the ratio of disturbing forces (from the bed shear stress) to the stabilising forces (submerged weight) acting on a single sediment grain, calculated as

$$\theta = \frac{\tau_0}{g\left(\rho_s - \rho)\right) D_g} \tag{2.4}$$

where g is gravitational acceleration, ρ_s is the sediment density and D_{50} is the median sediment grain diameter. The skin friction Shields parameter θ' is calculated using the skin friction component of the bed shear stress τ_0'. It follows that if the disturbing forces acting on a grain are greater than the stabilising forces then the grain will begin to move. The point at which a grain begins to move on the bed is delineated by a threshold (or critical) shear stress, characterised by the critical Shields parameter θ_{cr}. If $\theta' \leq \theta_{cr}$ there is no sediment motion and if $\theta' > \theta_{cr}$ sediment grains will begin to move—the onset of sediment transport.

2.2 Sediment transport

Sediment may be transported via two principal modes—while in contact with the bed ('bed load') or traveling as a suspension within the flow ('suspended load'). Bed load transport is defined as the fraction of the total transport load which is supported by inter-granular forces (Bagnold, 1956). Bed load transport formulae are numerous and varied in their form and applicability to different flow conditions. Commonly used formulae include those of Meyer-Peter & Müller (1948), Nielsen (1992) and Van Rijn (1984a). Most bed load formulae take the form of the available stress (characterised by $\theta' - \theta_{cr}$) raised to some power greater than unity. The resulting transport rate is expressed as a sediment flux Q_s in units of m^2s^{-1}. The suspended load is defined as the fraction of the total transport load which is supported by fluid drag forces (Bagnold, 1956). Here the nature of grains to settle towards the bed (with velocity w_s) is balanced by the vertical profile of suspended sediment concentration $C(z)$ due to finer particles being transported higher up into the water column than coarser ones. Assuming turbulent eddy diffusivity to vary parabolically with height above the bed the vertical concentration profile is often assumed to follow the so-called Rouse profile which can be written as (Soulsby, 1997)

$$C(z) = C_{ref} \left[\frac{z}{z_{ref}} \frac{h - z_{ref}}{h - z} \right]^{-\left(\frac{w_s}{\kappa u^*}\right)} \tag{2.5}$$

where C_{ref} is a reference concentration at height z_{ref} above the bed. The depth-averaged suspended sediment transport rate is given as the depth averaged sediment concentration C, multiplied by a convective velocity.

2.3 Bed forms and bed roughness

The roughness of the bed has an effect on the vertical profile of velocity above the bed and therefore the shear stress both at the bed and within the flow. However the sea bed is rarely, if ever, flat. Bed forms—sedimentary structures generated by the interaction between bed and flow—are often present on the bed. Bed forms (figure 2.2) vary in scale from ripples with wavelength (crest-to-crest dimension) $\lambda << h$ to megaripples ($\lambda \leq h$) to dunes ($\lambda \geq h$). Current generated bed forms tend to be asymmetric in profile with steeper lee slopes, created by the presence of turbulent eddies (the consequence of flow separation over the bed form crest). The effect of bed forms is to intensify friction with the flow through increased form drag (the variation in the pressure field over a bed form) and turbulence due to the bed form geometry. However the effect on the flow is dependent on the scale of the bed form (figure 2.2). Larger features such as megaripples and dunes create turbulent vortices which can scale on the flow depth, thus affecting the distribution of total bed shear stress and the mean flow velocity (Yalin, 1977). However smaller features, such as ripples or even individual grains, affect only the bottom boundary layer and are therefore important for skin friction processes which are important for sediment transport. The effect of dune-scale bed forms on the mean flow also has a direct impact on sediment transport through the stress available at the bed and is therefore an important parameter for numerical models (Villaret et al., 2011). The impact of the roughness lengths of ripples $z_{0,r}$, megaripples $z_{0,m}$ and dunes $z_{0,d}$ is displayed diagrammatically in figure 2.3. Depending on the height above the bed a different roughness element is 'felt' by the flow. However the total bed shear stress and the mean flow are affected by all roughness elements combined.

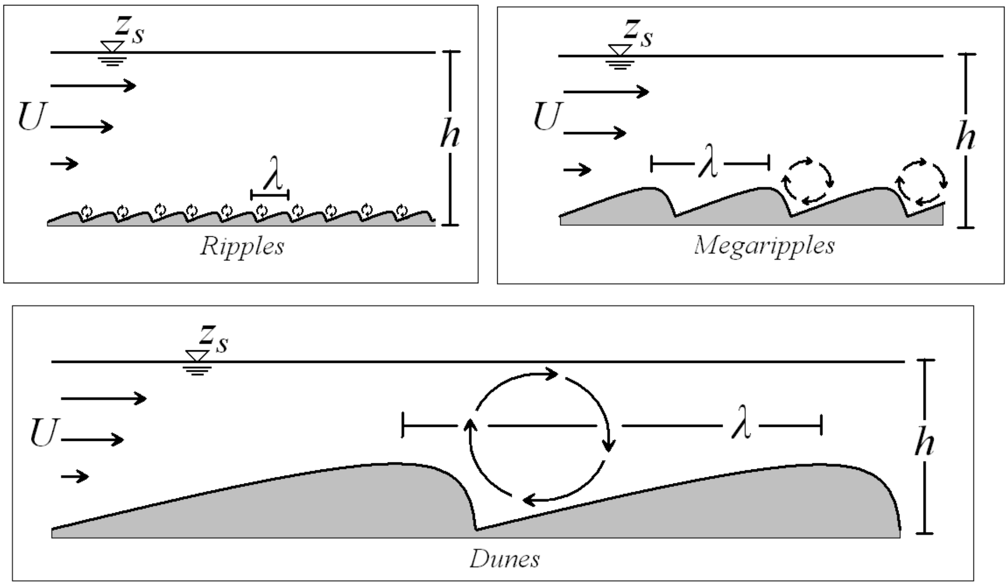

Figure 2.2 – Schematic examples (slices through the bed) of ripples, megaripples and dunes and the relative scale of macro-turbulent eddies that are formed on the lee side of the asymmetric bed form geometry

The Nikuradse hydraulic roughness k_s can be related to the total shear stress τ_0 through the drag coefficient C_D by

$$\tau_0 = \frac{1}{2}\rho C_D \bar{U}^2 \tag{2.6}$$

where $\bar{U}$ is the depth-mean flow velocity and C_D can be obtained (assuming

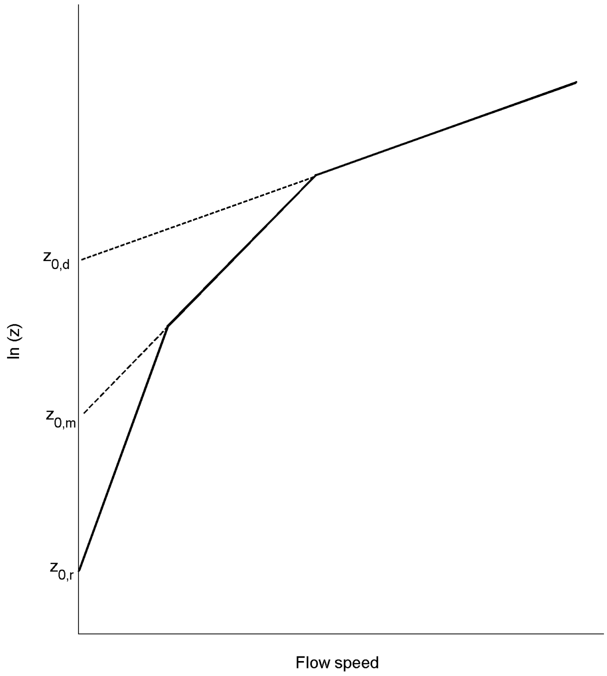

Figure 2.3 – Example of the effect on the vertical velocity profile (solid line) by the roughness length contributions of ripples ($z_{0,r}$), megaripples ($z_{0,m}$) and dunes ($z_{0,d}$)

a Nikuradse roughness relation) from

$$C_D = 2 \left[\frac{\kappa}{\ln\left(\frac{12}{k_s}\right)} \right] \tag{2.7}$$

The relationship between bed form geometry (principally their height η or steepness η/λ) and the hydraulic roughness k_s is complicated and, in practice, requires the prediction of bed form dimensions first (a two-stage approach). Van Rijn (1984b; 2007) presented a formulation for k_s based on the contributions of ripples, megaripples and dunes directly, without the need to predict bed form geometry separately. The method has been validated and performs reasonably well (Van Rijn, 2007).

2.4 Estuaries

Estuaries are tidal basins, defined as "semi-enclosed coastal bodies of water which have free connection with the open sea and within which sea water is measurably diluted with fresh water" (Pritchard, 1964). Present-day estuaries and tidal basins along the world's coastlines are relatively recent features on the Earth's surface. Their formation is attributed to the drowning of river valleys during the last marine transgression, caused by sea level rise after the end of the last glacial maximum (Russell, 1964). Since the last high-stand in sea level ($\sim$ 3000 years ago), tidal basins have been slowly infilling with both marine and terrestrial sediments. This prompted the theory that tidal basins, and estuaries in particular, are ephemeral phenomena in the history of the earth and will eventually totally infill with sediment so that their rivers will discharge directly into the sea (Meade, 1972). However evidence suggests that estuaries may be more permanent features of the Holocene. For example, recent net sedimentation rates in the Taf estuary, S. Wales UK, suggest that if this hypothesis was true the estuary should have in-filled long ago (Jago, 1980). The morphological evolution of estuaries remains a critical area of ongoing research, especially as the land around them faces increasing exploitation while sea level is predicted to rise and a changing climate alters many of the forces controlling morphodynamics. Estuaries have been focal points for much of Man's civilised development. As such, estuaries have become highly stressed environments as man's requirements of them became greater and ever more complicated. An example of one such pressure, land reclamation, can be found in the Dee Estuary, N.E. England. Here over 2000 acres of the estuary's intertidal area ($\sim$ 26%) was reclaimed in the early 1900's (Webster, 1929), resulting in an energy disequilibrium which caused unmanageable siltation and shifting of tidal channels leading to the port of Chester. The study of the morphological response (i.e. the change in the level of the bed in time) of tidal basins is therefore an important field of research.

2.5 The Dyfi Estuary

Situated on the shores of West Wales and emptying into Cardigan Bay is the Dyfi Estuary (Figure 2.4). Classed as macrotidal with an extreme spring tidal range of 4.88m, the Dyfi is a dynamic sandy tidal basin with frequently shifting channels and sand-banks. At the mouth of the estuary is a permanent spit of sandy sediments, anchored on ship's ballast from around the 18^{th} Century. The stability of the spit is attested by its extensive covering of aeolian dunes. The spit also provides a stable headland for a deep scour pit at the estuary's mouth which is believed to be self-sustaining due to the convergence of tidal currents (Brown & Davies, 2007). Occupying a deltaic-estuarine plain area of around $45km^2$ (figure 2.5), over $17.3km^2$ is submerged by the extreme spring tide (Shi & Lamb, 1991).

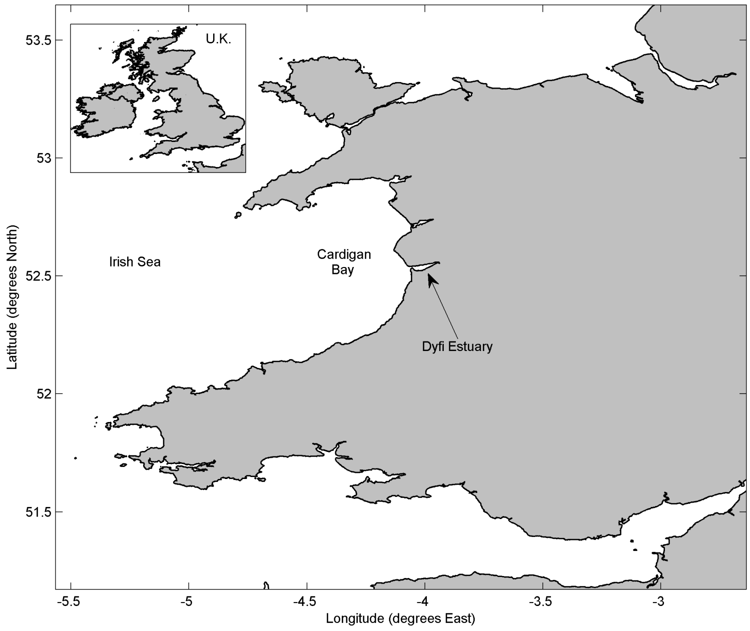

Figure 2.4 – Location of the Dyfi Estuary with regards to the U.K. mainland

In 1968 over 2,000 hectares of the estuary were designated as a National Nature Reserve (NNR) by the Nature Conservancy Council. This is mostly due to the importance of the dune system at Ynyslas which is home to an abundant population of protected wildlife (Nature Conservancy Council, 1983).

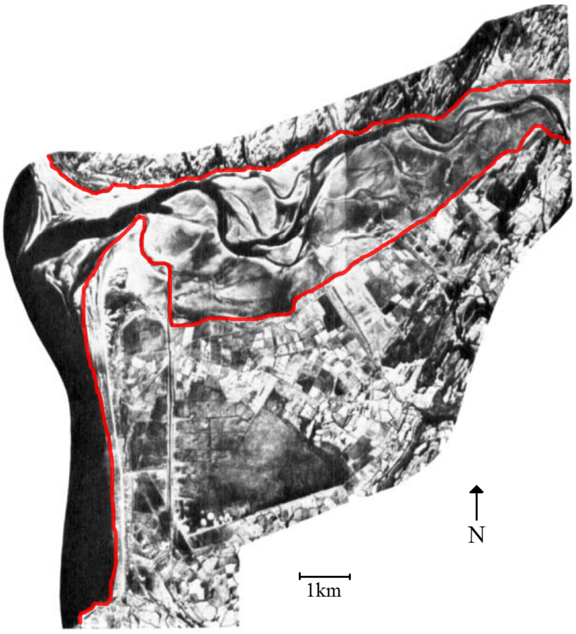

Figure 2.5 – Aerial photograph mosaic of the estuary as it was in the late 60's, taken at low slack water. Red line marks the position of the coastline. Adapted from Jones, 1969.

The River Dyfi, translated from Welsh as "fluid, peaceful and smooth-running", is a relatively small river with yearly average flow rates of $\sim 23m^3s^{-1}$ and peak flood rates rarely exceeding $100m^3s^{-1}$. The river source lies 30 miles from its mouth at the mountain lake of Craiglyn Dyfi in the Aran mountains, meandering through the southernmost limb of the Snowdonia National Park and separating the Welsh counties of Gwynedd and Powys.

There have been numerous studies into the post-glacial sedimentary history of the estuary (Wilks, 1979; Haynes & Dobson, 1969; Shi & Lamb, 1991) and the sedimentation (Shi, 1991; 1993) and channel dynamics (Shi et al., 1995) of intertidal saltmarshes in the area. The estuary has also been the focus of recent numerical modelling with studies into flood event management (Robins, 2008a; 2008b, Robins et al, 2011) and estuarine sediment transport with respect to the influence of tidal flats (Robins & Davies, 2010) and flood-ebb dominance (Brown & Davies, 2010).

2.6 Morphology of tidal basins

Morphology is a consequence of the residual sediment transport pattern arising from the relative strength and duration of flood and ebb tidal currents (Dronkers, 1986). However, it is also true that the residual sediment transport pattern is a consequence of the morphology itself (Prandle, 2006). The residual sediment transport pattern is primarily based on the asymmetry of the tidal wave as it propagates over a rough bed and dissipates energy via friction. As the frictional effect on the tidal wave is greater towards low water (due to the reduced depth) than towards high water the propagation speed of the tidal wave trough slows relative to the speed of the wave crest (Pugh, 1987). This has the effect of changing the relative strength of the flood (in-basin) and ebb (out-basin) tidal currents. Due to the shorter, stronger flood tidal currents and the quadratic relationship between velocity and bed shear stress, the effect of tidal asymmetry is to introduce a dominance to flood sediment transport over that on the ebb. The ratio between tidal amplitude and channel depth has been found to be one of the primary controls on tidal asymmetry (Speer & Aubrey, 1985). The presence and extent of intertidal flats has been found to force ebb-dominance in estuaries (Fortunato & Oliveira, 2005), with tidal channels (both a consequence and determinant of tidal flats) concentrating ebb tidal currents and thus increasing their velocity and ability to export sediment (Dronkers, 2005). There is therefore a dynamic competition between morphology and sediment transport in estuaries, arising from the non-linearities of the physical processes involved and differences in time scales between hydrodynamics and morphological change.

2.7 Long term morphological modelling techniques

Simulating morphological development with a coastal area scale, process-based model often requires a computation to be carried out over a great number of model grid nodes and over relatively short time steps (for the purpose of data resolution). In a tidal setting it is important to simulate the constantly changing free surface elevation (and associated tidal currents) which increases computational effort significantly.

In its simplest form, a morphological model consists of input conditions, a flow computation, a sediment transport computation and then an update to the model bathymetry based on the calculated sediment fluxes. However, updates to the bed level are generally much faster than the time needed to compute a hydrodynamic time step (Roelvink, 2006). With the assumption that bed level changes occur much more slowly than changes to the flow field (typically one to two orders of magnitude longer, Van der Wegen et al., 2008) it is possible to speed up the computation by splitting the hydrodynamics and morphology into separate reference frames—i.e. recognising that the morphology ‘experiences’ time more slowly than the hydrodynamics.

One solution to this problem is the tide averaging method. Here the morphology is assumed to remain static during a tidal cycle. At the end of the tidal simulation, the residual sediment transport field is computed and used to update the bed—therefore simulating many tides of morphological development through one tidal cycle of hydrodynamics. However the flow field is unable to adjust to the changing bathymetry and thus incontinuities will develop. A continuity correction (Latteux, 1995) can be applied to the flow field (changing the magnitude of flow rate assuming the direction remains the same), however the problem remains that small changes in the bed are unable to affect the flow field as there is no real-time feedback to the flow computation. Examples of the tide-averaging method in use can be seen in De Vriend et al. (1993), Roelvink et al. (1994) and Cayocca (2001).

The tide-averaging method is flawed in the sense that it does not properly take into account the feedback between morphology and hydrodynamics. This can be overcome by the use of the Morphological Factor (MF) method, first discussed (albeit with a continuity correction) by Latteux (1995), and later by Roelvink (2006). The MF method takes the same assumption that morphology exists in a different (and longer) reference frame than the hydrodynamics. However, here the sediment fluxes and subsequent bed level change are computed every time step. The bed level change is then multiplied by a coefficient before being fed back into the subsequent hydrodynamic computation (figure 2.6). In this way the MF coefficient equal to N speeds up the computation by N times while allowing the flow field to respond to changes in bathymetry relatively frequently. Examples of the MF method in use can be seen in Lesser et al. (2003), Hibma et al. (2003; 2004a), Van der Wegen et al. (2008) and Van der Wegen (2010). Ranashinghe et al. (2011) evaluated the MF method and its affect on morphological predictions, concluding that the choice of MF coefficient should be based on the hydrodynamic conditions and resolution of the model grid.

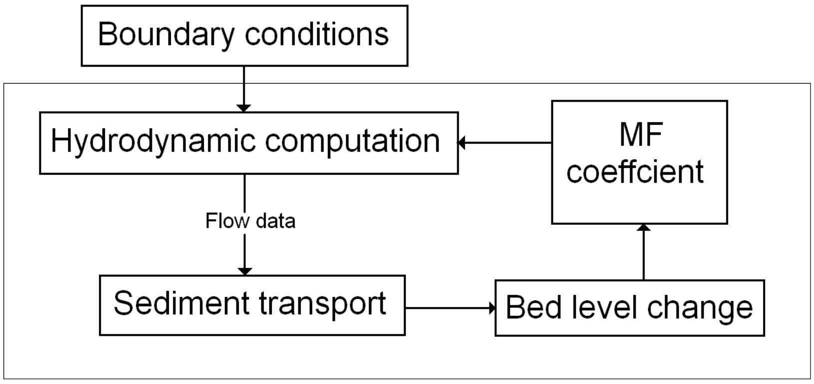

Figure 2.6 – Schematic representation of the Morphological Factor (MF) method of Roelvink (2006)

2.8 Channel-bank systems and pattern formation

Patterns exist everywhere in nature and at almost all scales. The initial formation of tidal channel networks from a flat bed has been extensively modelled (Schuttellaars & de Swart, 1999; Hibma et al., 2003; Hibma et al., 2004a; Marciano et al., 2005) and some of the key processes behind the pattern formation have been identified (Coeveld et al., 2003; Hibma et al., 2004b). Principally there exists a positive feedback between morphology and tide-averaged sediment transport so that initial instabilities in the bed have a tendency to grow (Seminara & Tubino, 1998; 2001). It is also interesting that tidal channel networks that look remarkably like those studied by van Veen et al. (2005) in the estuaries of the Netherlands (figure 2.7) were produced by a 2-D process based model (Hibma et al., 2003; 2004a), yet with no river input and only simple M_2 harmonic tidal forcing at the mouth (figure 2.8). Two distinct stages of the morphological development of tidal basins over the long term have been identified—firstly, the formation of complex tidal channel networks (over decades to a century) and later the adjustment of the mean along-basin bed slope over the order of 1000 years (Van der Wegen & Roelvink, 2008).

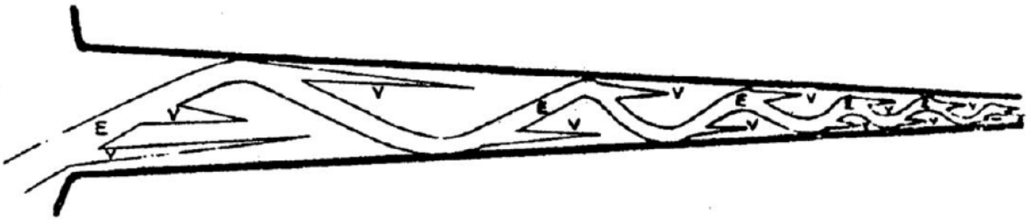

Figure 2.7 – Schematic representation of a Dutch tidal basin, highlighting flood- and ebb-dominant channels in the network ('V' and 'E' on the figure, respectively). From Van Veen et al. (2005)

2.9 Theory of open, dissipative systems

A system is defined as a set of interacting processes that are isolated, in whole or in part, from the surrounding environment. An open system is one that is able to exchange both mass and energy freely across one or more of its boundaries with the surrounding environment (Von Bertalanffy, 1950; Huggett, 2007) and that acts as a sink to energy through dissipation within the system boundary. Systems are defined as dissipative when they are removed from thermodynamic equilibrium with their environment—i.e. the along-system gradients in the dissipation of energy are non-zero. Close to equilibrium, responses to change (e.g. a change in the energy input to the system) are linear and relatively slow. However when a system is considered far from thermodynamic equilibrium small forces or gradients can have non-linear effects (Prigogine & Stengers, 1984). It is in this far from equilibrium, dissipative state that systems are prone to spontaneous self-organisation (Phillips, 1999) as infinitesimal disturbances are amplified and cause the system to evolve towards a new form of order.

Coastal area numerical models are examples of systems that are partly isolated from the outside environment. The boundary condition that encases the model interior acts as a barrier that is permeable or impermeable to the flow of mass and energy. For example a model of a section of coastline under the influence of tidal action could allow the transfer of tidal energy and fluid flow (mass) across the sea-ward boundary, with energy being dissipated along the coast. Such a model can be viewed as an open, dissipative system and as such may display some of the dynamic behavior that natural systems exhibit.

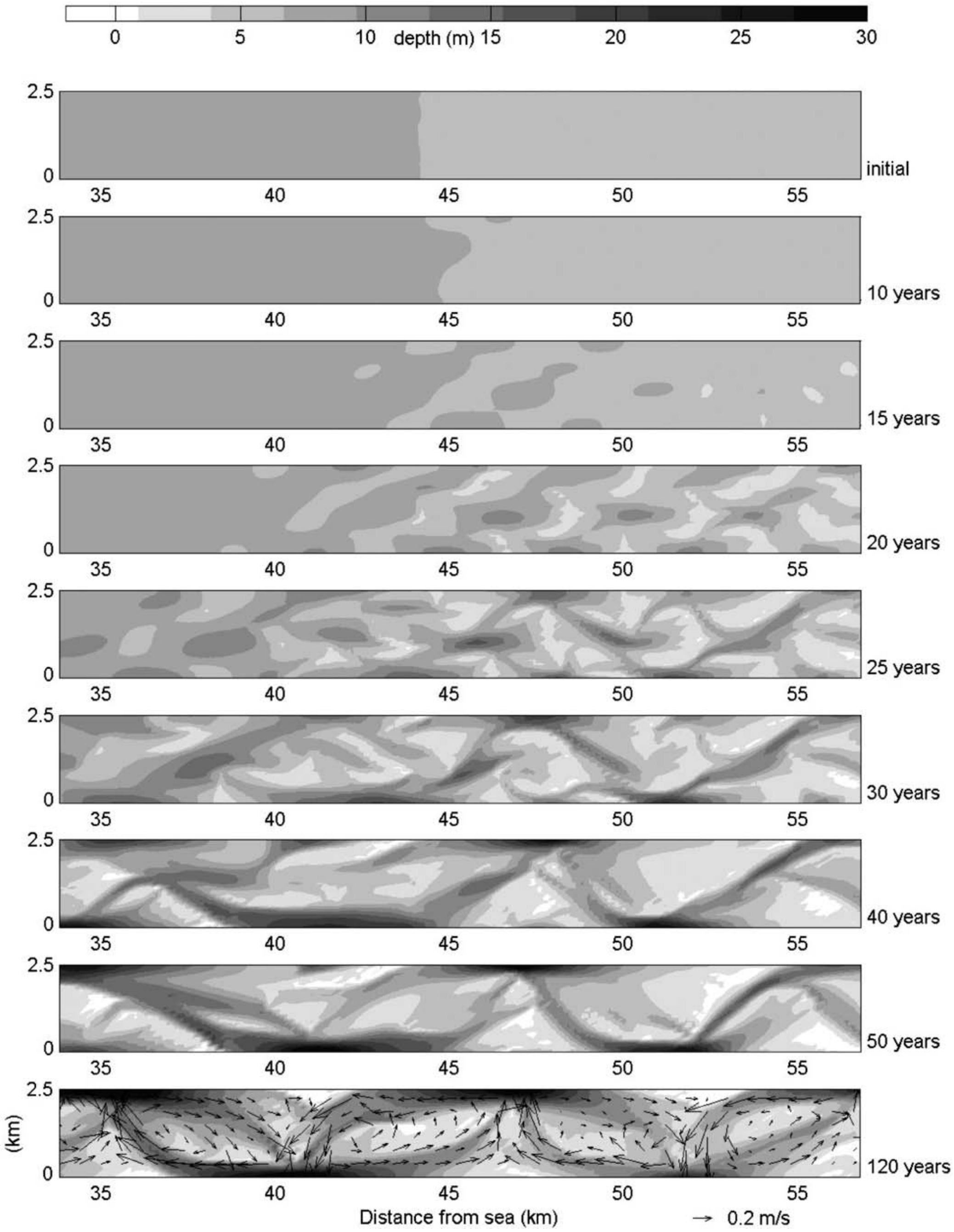

Figure 2.8 – Complex tidal channel network produced by a 2DH morphological model using the MF method. From Hibma et al., 2003

Chapter 3

Long-term morphological modelling in `TELEMAC 2D` and `SISYPHE`

3.1 Introduction

The challenge involved in the morphological modelling of complex coastal environments over the medium to long term (decades to centuries) is two-fold. Firstly the treatment and complexity of the modelled processes and input conditions has a direct and significant effect on the final morphological outcome. The addition of waves, treatment of suspended sediments, flood and storm events will each give rise to a different result from a model which does not include them. Secondly, the nature of numerical, process-based modelling requires the use of a time-stepping approach to solving the hydrodynamic and sedimentological equations. As such an increase in model complexity (e.g. grid resolution, inclusion of waves etc.) or simulation length will require an increasing amount of processor time to arrive at an answer.

There are two main approaches to this problem. The simplification of the input parameters (so-called 'input reduction') where complex events are schematised into step changes; for example a continuous change in free surface elevation due to the tide can be represented by a series of step changes in free surface elevation, the number of which will determine the speed of the total simulation (as opposed to continuous modelling of a changing free surface). Input reduction techniques are often used when the simulation requires a number of input conditions which can cause a simulation to take an unfeasible amount of time to run. An example is the inclusion of an annual wave field at the open boundary of the model. The wave data may consist of many different wave conditions throughout the year—each of which will have to be modelled separately. Here input reduction could take the form of a few wave fields given a weighted average to represent the annual wave climate (Brown, 2007). The second approach is to simulate every process in real-time, but to split the hydrodynamic and morphological components of the system into two separate reference frames. It is this approach that will be explored in the following chapter and the method which is applied to all work described in this thesis.

3.2 The `TELEMAC 2D` Hydrodynamic modelling system

Launched in 1987 by the research and development department of Electricité de France (EDF), the `TELEMAC` hydro-informatics project has grown to become one of the leading numerical modelling suites for free-surface flows in shallow-water environments. `TELEMAC 2D` solves the depth-averaged Saint-Venant shallow water equations on an unstructured, triangular mesh (Galland et al, 1991; Hervouet & Bates, 2000). The shallow water equations are solved in their non-conservative form with the total depth of water h and velocities u and v (components of velocity $\vec{U}$ in x and y respectively) as unknowns. The free surface z_s is defined as the free surface elevation around some datum (for example mean sea level MSL), with the total depth h defined as the distance from the free surface to the bed z_b (figure 3.1). The continuity equation (equation 3.1) and depth-integrated versions of the

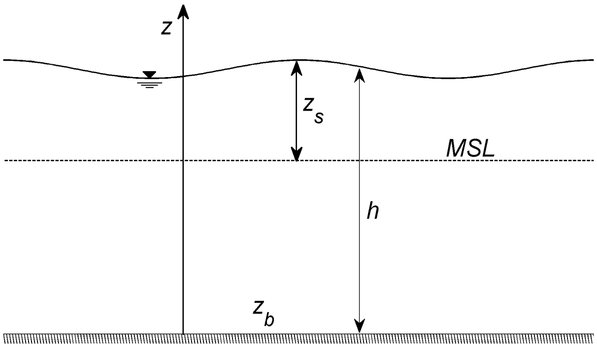

Figure 3.1 – Definition of the free surface elevation z_s, bed elevation z_b, total depth h and vertical coordinate z over which the shallow water equations are integrated.

equations of motion (equations 3.2 and 3.3) can be written as

$$\frac{\partial h}{\partial t} + \vec{U}\vec{\nabla}\left(h\right) + h\mathrm{div}\left(\vec{U}\right) = 0 \tag{3.1}$$

$$\frac{\partial u}{\partial t} + u\frac{\partial u}{\partial x} + v\frac{\partial u}{\partial y} = -g\frac{\partial z_s}{\partial x} + F_x + \frac{1}{h}\mathrm{div}\left(h\nu_e\,\overrightarrow{\mathrm{grad}}\left(u\right)\right) \tag{3.2}$$

$$\frac{\partial v}{\partial t} + u\frac{\partial v}{\partial x} + v\frac{\partial v}{\partial y} = -g\frac{\partial z_s}{\partial y} + F_y + \frac{1}{h}\mathrm{div}\left(h\nu_e\,\overrightarrow{\mathrm{grad}}\left(v\right)\right) \tag{3.3}$$

where F_x and F_y are momentum source and sink terms (friction, Coriolis force etc.) and ν_e is the momentum diffusion coefficient (Hervouet, 2007). The variables h, u and v are solved for in two steps: 1) Advection and 2) Propagation + diffusion + source terms. The equations are linearised in `TELEMAC 2D`, such that the pressure is assumed to be due to hydrostatics. This method has the advantage of being relatively light on computational resources but runs into difficulties when considering large gradients in depth.

The numerical implementation of `TELEMAC 2D` is written in `FORTRAN 90` and solved variables are saved as numerical arrays (size consistent with the number of grid nodes) and passed between various subroutines responsible for the calculation of computational variables. `TELEMAC 2D` is available under open source GNU licensing via SOGREAH, France. Much of the model code may be used as it is supplied in a default setting, however there are a number of steps that must be taken and specific files that must be created (some specific to `TELEMAC` and others universal to numerical models) in order to set up a working (and stable) hydrodynamic model, as outlined in the following sections.

3.2.1 Finite element mesh and mesh generation

The momentum and continuity partial differential equations 3.1–3.3 are solved on an unstructured mesh of triangular 'elements' (of number NELEM), defined as a sequentially numbered set of mesh node vertices (of number NPOIN) with coordinates in (x, y, z_b) space. The mesh file ('geo' file) is ordered in BigEndian binary and also contains elements listed as an interconnectivity array of grid nodes 'IKLE' (i.e. each triangle listed by its three grid node vertices) and an array of grid boundary nodes 'IPOBO', listing the boundary nodes as sequential integers numbered anti-clockwise from the most bottom-left hand point in the grid (i.e. $\min(x), \min(y)$).

One of the main benefits of the use of finite element grids over the simpler, finite difference approach is that the unstructured mesh is more readily able to approximate complicated shapes (e.g. coastlines) as well as lend greater grid resolution to certain areas over others. Although a universally high grid resolution is often the most favourable, the computational cost (time to complete an iterative time-step) increases with the number of grid points in a domain. The aim of successful finite element mesh generation is to create a mesh fine enough to resolve present or anticipated features (in both the bed and the flow), but coarse enough to avoid computational redunandcy—particularly in less active areas of the domain.

To construct a viable grid there are a number of mesh generation packages available, some of which require purchase and others which are publicly available under GNU licensing. One such openly-available package is the pre- and post-processor 'BlueKenue', developed by the Canadian National Research Council. Version 3.1.1 incorporates an advanced mesh generation interface including channel meshing, inclusion of sub-meshes and the ability to hold a greater amount of data in memory than, for example, the now retired software package Matisse previously bundled with `TELEMAC 2D`. BlueKenue was used to generate all model grids described subsequently.

3.2.2 Example model grid of the Dyfi Estuary

Mesh generation involves three main steps: identification and input of the domain boundary, populating the domain with mesh nodes and elements, and the interpolation of bathymetry onto the model grid. For the mesh to be viable in `TELEMAC 2D` one also needs to convert the mesh into `SELAFIN` (`TELEMAC 2D` proprietary) binary file format and assign liquid boundary conditions in a proprietary ASCII file format. However only the former is possible in BlueKenue at present (see section 3.2.3).

The first step in the mesh generation process is the identification and choice of the domain outer boundary, i.e. the area covered by the model. In an intertidal area this can be a speculative operation as the position of the 'dry' coastal boundary line is a trade-off between being far enough above extreme high water to remain dry and low enough not to include too many extraneous landward points in the model simulation (redundant point that will needlessly increase computation time). For the case of the Dyfi Estuary it was decided that the 4m contour line would suffice (extreme high water never exceeds 3m above ODN in the Dyfi due to the regular tide alone), with the landward boundary following the railway line to the south over part of its route (Figure 3.2). The boundary extends to cover the spit at the mouth of the estuary—this was to force the spit to be non-erodible (a permanent feature of the estuary, Brown & Davies, 2007). For the most part the choice of coastal contour in the Dyfi is not critical as the railway forms a tidal flood barrier and on the northern coast the estuary is banked by steep, mountainous terrain. However, more generally, it is important to include terrain which is regularly flooded by high spring tides so as not to exclude a potentially important component of the tidal prism. Elevation data from a 2004 LiDAR aerial survey of the area (courtesy of the Environment Agency) was used to determine boundary position, which was then traced by hand through the contours.

As the LiDAR survey data only covered the estuary interior, the grid

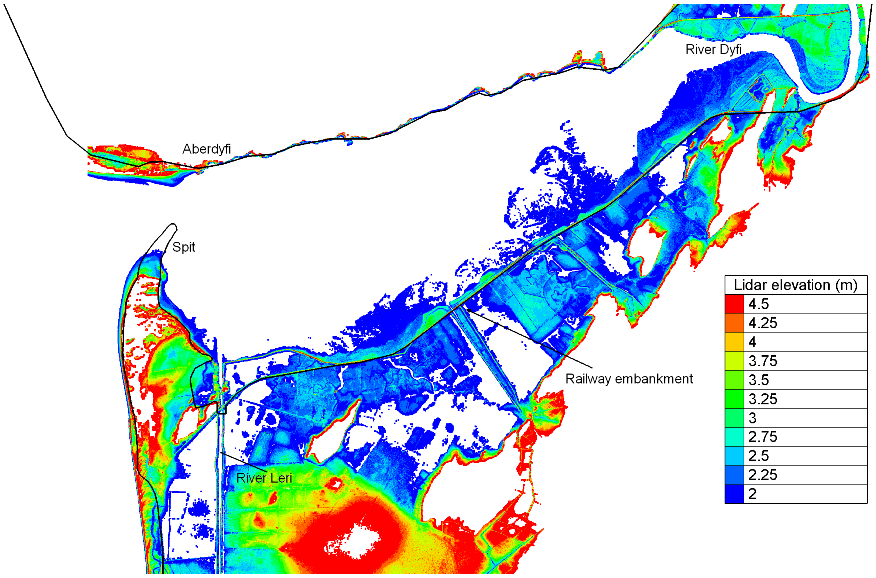

Figure 3.2 – LiDAR elevations above mean sea level in the 2-4.5m range used to determine coastal boundary placement (solid black line). The positions of the town of Aberdyfi, the two rivers (the Dyfi and Leri) and the railway embankment are marked.

boundary of Robins (2008a; 2008b) was used for the model extension offshore into Cardigan Bay (Figure 3.3). A grid resolution of 1000m offshore, reducing to 15m for the interior of the basin was chosen to maximise resolution within the estuary while keeping the total node count (and therefore CPU cost) to a minimum, giving a final node count of 91,122. To include the River Dyfi up to the extent of tidal influence (and thus a significant contribution to the basin tidal prism) it was decided to include the river as a canalised channel mesh with a set number of cross- and along-stream channel nodes, utilising the channel-mesh function of BlueKenue.

Bathymetry mapping

The 2004 LiDAR survey was used for grid bathymetry where coverage existed. The original data set was thinned from 1m to 5m ground resolution and any elevations greater than 10m above mean sea level were automatically excluded. As LiDAR is only effective in dry areas above 0m ODN (Laser attenuation and absorption through water causes inaccuracies and disconti-

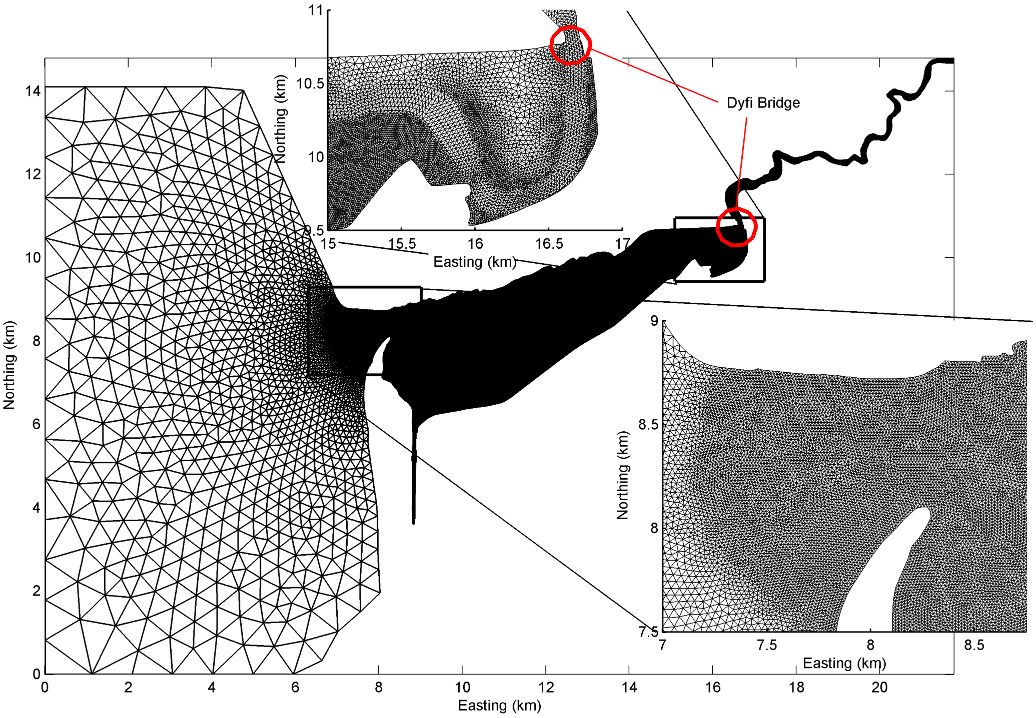

Figure 3.3 – The final Dyfi Estuary mesh with insets around the spit and River Dyfi areas and the location of Dyfi Bridge (red circles). The mesh resolution fines from 1km at the outer boundary to 15m in the estuary interior. Channel meshes for the Rivers Dyfi and Leri are treated separately. The total mesh node count is 91,122 (179,580 elements).

nuities in the data) any elevations below mean sea level were also excluded. Unfortunately, this created extensive areas without usable data within the main channel as well as the entire offshore domain. To fill in bathymetric data for these areas the thinned LiDAR data set was merged with the model of Robins (2008a; 2008b). To minimise the total number of grid nodes and as river flood events were not the focus of this particular investigation, the River Dyfi was schematised into a channel of constant cross section. The upland slope (i.e. up-stream of the head of the estuary at Dyfi Bridge, figure 3.3) of the Dyfi was extracted from the original LiDAR survey and used to create the schematised river bathymetry. A constant depth of 1m below this upland slope was used to carve out the river channel, producing a smooth and regular river. This is important as initial tests with uneven river bathymetry and a triangular mesh produced numerical instabilities during model spin-up. In this way, the upstream tidal volume of the river is approximated and a more realistic river input is achieved. Once the bathymetric data set was complete and free from discontinuities it was linearly interpolated onto the domain mesh to produce the final grid (Figure 3.4).

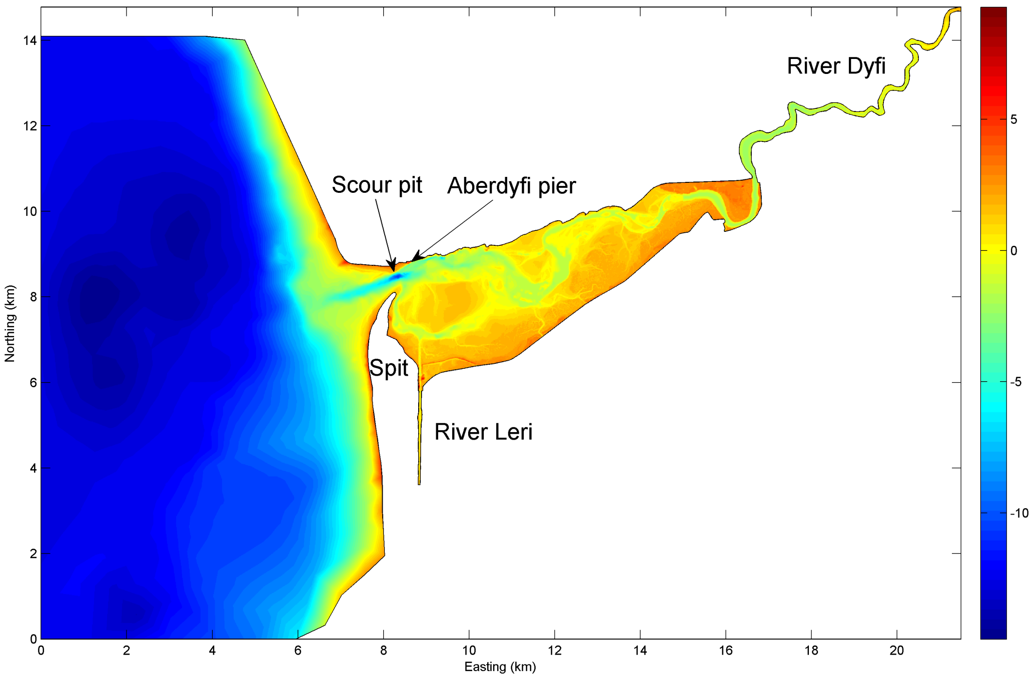

Figure 3.4 – Bathymetric map of the Dyfi Estuary grid. Bed elevations are in m relative to ODN

3.2.3 Boundary conditions

The outer-most points of a model domain, the boundary nodes, hold an important role in a numerical model as they represent the spatial limit of the computation. As mentioned in the previous section, boundary nodes are numbered sequentially around the outer boundary, anti-clockwise from the bottom-left node of the domain. At each node the behavior of the free surface, and the two components of velocity (or flow rate) are set using an integer identifier. There are three main conditions, namely:

- Closed condition (value 2)—represents a closed 'wall' condition with no slip or flux along or through the boundary
- Free variable (value 4)—allows a free flux or depth
- Prescribed variable (value 5)—value of free surface, fluid flux or tracer is set to a prescribed value

Boundary conditions are entered into the model via a boundary conditions ('conlim') file (Appendix I), which lists the boundary points and their conditions in order. The generation of the conlim file is often handled by the pre-processing software, however at present BlueKenue is unable to perform this action. To this end, a simple boundary tracing and node numbering algorithm was written in `Matlab` (BOundarY COndiTions for Telemac, BOYCOTT) which contains a simple graphical user interface and is able to assign simple boundary conditions as well as automatically detect islands (interior closed boundaries) in the grid. A full description of the algorithm can be found in Appendix II. Two main forms of boundary can be described for a hydrodynamic simulation; solid (e.g. a coastline or other solid, impermeable structure) and liquid (e.g. the open sea, a river inflow etc.) For the most part (and within the scope of this work), solid boundaries are closed to the fluxes of fluid and act as an impermeable wall. As such the conditions on solid boundaries are static and permanent in time. Liquid boundaries however, may have conditions that vary in time, allowing variables such as the free surface or fluid flux across the boundary to follow time-dependent curves or specific events.

3.2.4 Steering files

The user front-end is handled by a steering file ('cas' file) which the user may edit to assign values to key variables and activate various features and modules (an example of a steering file can be seen in Appendix III). The steering file is essentially just a user-edited text file that is interrogated by the `TELEMAC` code. The names of the grid file, boundary conditions file and user `FORTRAN` files are all specified in the steering file as well as other important high-level variables such as `TELEMAC` version number and number of parallel processors. However the majority of the steering file comprises instructions for how the simulation is to be run, for example the setting of computation time-step, the number of iterations the computation is to last for, the choice of output variables to be saved to the results file, the choice of turbulence scheme and choice and settings for the numerical solvers.

3.2.5 Implemented schemes and subroutines

The flexibility of `TELEMAC 2D` lies in the significant amount of choice available to the user with regard to the presence and form of a large number of numerical schemes. It is important, then, to outline the ‘form’ of `TELEMAC 2D` utilised within the present body of work. All models described in subsequent chapters were run with this set-up of numerical options unless specifically highlighted otherwise.

Bottom friction

Bottom friction is one of the core sink terms in the momentum equations and thus has a significant impact on flow rates—especially in shallow water environments. A complex coupling and update scheme for total bed roughness is outlined in Chapter 5. However for standard cases a simple Nikuradse roughness k_s of 0.01m, constant in both time and space, has been adopted for simplicity. `TELEMAC 2D` (currently) uses a separate bed roughness to calculate flow conditions than that used in `SISYPHE` to calculate the near-bed (skin friction) shear stress and subsequent sediment transport rate. The issues surrounding this disparity are addressed and explored in Chapter 5.

Turbulence

The modelling of turbulence in shallow water environments is an active and much-discussed area of research of which this work is not a part. `TELEMAC 2D` includes a number of options for the treatment and calculation of turbulent energy which not only have various impacts on the momentum equations but also introduce increases in computation time due to the extra iterations required. For simplicity's sake and to keep complicating variables to a minimum a constant viscosity approach was chosen for the implementation of turbulence, with a single viscosity coefficient representing molecular and turbulent viscosity as well as dispersion.

Coriolis force

Due to the relatively small-scale (i.e. smaller than the Rossby radius) of model grids used in this body of work it was decided to omit the Coriolis force from the source terms for simplicity in respect of the input variables.

Tidal flats

The treatment of tidal flats—areas of the domain which become 'dry' during a computation—is a critical consideration when modelling flows in a shallow, tidal environment. Dry elements are defined as those with a constituent mesh node (vertex) with bottom elevation greater than the free surface of another mesh node within the same element. The free surface is then reduced on the 'high' node by the difference between its bottom elevation and the free surface elevation of the 'low' node. This helps to conserve real free surface gradients (for example on elements with two wet and one dry node).

It is often useful to declare a minimum depth in 2DH models below which any flow variables are set to zero. However any arbitrary minimum depth invalidates the conservation of mass (Hervouet, 2007). It was also noted during preliminary tests with morphological coupling that minimum depth thresholds often created morphological instabilities in very shallow areas. Therefore no minimum depth threshold has been adopted here; instead the free surface correction in the tidal flats subroutine removes flow rates over dry elements. In this way the computation is solved for all points in the domain and then adjustments are made (u,v and h set to zero) on dry nodes only.

3.3 `FORTRAN` subroutines

Any model subroutines that have been altered by the user must be concatenated into a single `FORTRAN` script and listed in the steering file. Upon start-up and initialisation `TELEMAC 2D` replaces any subroutines within its subsequently compiled executable with those present in this script. Two key subroutines which were utilised here—`BORD` and `STRCHE`—are now discussed.

3.3.1 Time-varying liquid boundary conditions with `BORD`

Coastal hydrodynamic models often include time-varying liquid boundary conditions, one of the most important in the coastal environment being the variation of free surface due to the tide. In all of the simulations described in this work it is this variation of liquid boundaries due to the tide that is the main source of energy, from which all subsequent modelled effects in the interior of the model are derived. In this way the tide is modelled initially at the liquid boundary and then propagates into the rest of the domain.

To model the time-dependent free surface elevation at the boundary the subroutine `BORD` was applied, which takes each liquid boundary point with prescribed free surface (value 5 in the conlim file) in turn and calculates the free surface elevation z_s at each time step using the formula

$$z_s = A_0 + A_1 \cos(\sigma_1 t + G_1) + A_2 \cos(\sigma_2 t + G_2) + \cdots A_n \cos(\sigma_n t + G_n) \quad (3.4)$$

where for each of n tidal constituents A is the tidal amplitude, σ is the tidal frequency, t is time and G is the tidal phase. Any number n of tidal constituents (denoted by subscripts) may be added together to model a specific tidal elevation at a specific time. Tidal constituents may also vary in space, being set as an array of constituents through which `BORD` cycles to represent the surface elevation at each of the liquid boundary points. Nodes along the liquid boundary are iterated through in the same counter-clockwise order in which they are numbered, beginning from the bottom-left hand node in the grid.

3.3.2 Bed roughness array `STRCHE`

The bed roughness k_s may be initialised as an array of values representing the bed roughness at each point in the domain. Grid nodes are cycled through and the appropriate bed roughness is applied to the indexed array either from a value specified within the iterative loop or read in from an external file containing roughness lengths in the sequential order 1:NPOIN. Although bed roughness is primarily generated by the presence of sedimentary bed forms such as ripples and dunes (Van Rijn, 2007) there is at this time (version `v5.9`) no direct link between `TELEMAC 2D` and `SISYPHE` concerning the roughness generated by bed forms which may be significant regarding the calculation of depth averaged currents in `TELEMAC 2D` (Villaret et al, 2009; Villaret et al, 2011), although it is a planned addition to future releases of the code. The impact of a shared bed roughness between `TELEMAC 2D` and `SISYPHE` on flow calculation and the resulting sediment transport is addressed in Chapter 5.

3.3.3 The `TELEMAC 2D` results file

Output variables from a successful simulation in `TELEMAC 2D` (or `SISYPHE`) are formatted for sequentially populated BigEndian binary data. The file begins with a header containing data pertaining to the grid such as number of nodes (NPOIN) and elements as well as the connectivity table IKLE. Saved output variables are then entered as rows of continuous data NPOIN long. The format of the results file is the same for `TELEMAC 2D` as for `SISYPHE`, however the available output variables can vary as `SISYPHE` calculates certain variables that `TELEMAC 2D` does not (e.g. bed shear stress, sediment transport rate, bed sediment composition). Full lists of the available output variables can be seen in the example steering files in Appendix III.

3.4 Modelling sediment transport with `SISYPHE`

One of the larger suites of subroutines is the sediment transport module `SISYPHE`, developed as both a stand-alone model (with suitable input result files from previous runs of `TELEMAC 2D`) and as an internally-coupled module which can be run alongside `TELEMAC 2D` simultaneously. In coupled mode depth and velocity data arrays are passed internally (i.e. within the system's RAM) to `SISYPHE` and its subroutines where they are used to calculate sediment transport magnitudes and directions. `SISYPHE` is able to calculate sediment transport as bed-load or total-load (in an equilibrium, sediment continuity mode) via a choice of seven transport formulae, or as suspended load via the implicit calculation of a suspended sediment concentration profile and the use of an Advection-Diffusion (A-D) transport algorithm. Just as in `TELEMAC 2D`, `SISYPHE` is controlled at the front-end via a steering file where the choice of transport algorithm, variables such as grain size and bed composition as well as various extra features such as bed slope effect and avalanching may be altered or activated.

Morphological changes are modelled by coupling `TELEMAC 2D` and `SISYPHE` so that data are passed between both modules at each time-step (figure 3.5). Tidal and river flow data generated by `TELEMAC 2D` are passed at each time-step (or at an interval set by the user) to `SISYPHE` where they are used to calculate local sediment transport rates and directions. The resulting local convergence or divergence of sediment flux results in bed accretion or erosion respectively. The updated bed level data are then passed back to `TELEMAC 2D` for use in the next flow computation. In this way the bed evolves dynamically with a feedback between the bed morphology and the hydrodynamics.

Bed level update

There are two morphological models available in `SISYPHE`—an equilibrium, local bed evolution model and a model incorporating an advection-diffusion scheme wherein suspended sediment may bypass grid cells and contribute to non-local morphological evolution. The equilibrium model is simply a statement of local sediment continuity (Exner's equation) so that (Hervouet, 2007)

$$(1-n)\frac{\partial z_b}{\partial t} + \mathrm{div}\left(\vec{Q_s}\right) = 0 \tag{3.5}$$

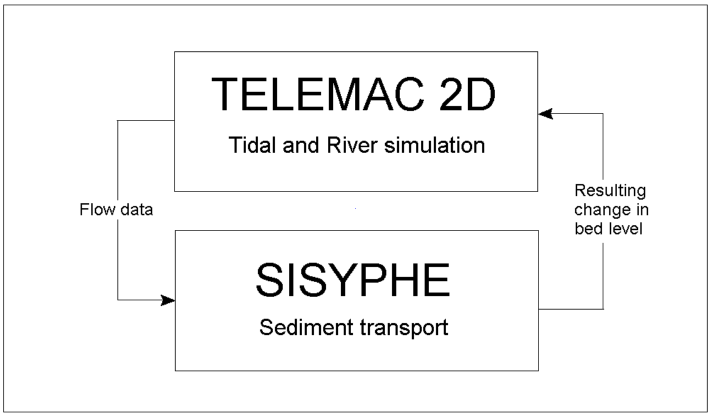

Figure 3.5 – Schematic representation of the flow of data between `TELEMAC` and `SISYPHE` during internal coupling.

where $\vec{Q_s}$ is the total load sediment flux vector (units $m^2 s^{-1}$) and n is the bed porosity. In a schematic sense the equilibrium model assumes that all sediment entering or leaving a discrete area of bed (i.e. a grid node) will contribute to bed-level change. However when suspended sediment transport is enabled, `SISYPHE` solves an advection-diffusion scheme for suspended sediment concentration C. The advection-diffusion scheme is more desirable for morphological modelling as it provides a more complete description of the physical processes involved in sediment transport and allows a realistic bypassing of grid notes by suspended sediments. However, its effect on stability when coupled with concepts included in this work (discovered during preliminary testing) led to its omission from all of the simulations presented in this thesis. Section 3.7 gives a full description of the advection-diffusion scheme and its associated stability effects on bed morphology.

Bed shear stress calculation

`SISYPHE` calculates the bed shear stress τ_0 locally using depth-averaged velocities passed from `TELEMAC 2D`. τ_0 is calculated within `SISYPHE` using a quadratic friction coefficient C_D so that

$$\tau_0 = \frac{1}{2}\rho C_D \bar{U}^2 \tag{3.6}$$

The determination of C_D is based on the law of bottom friction (for which there are various options). In the present work a Nikuradse bed roughness relationship between k_s and C_D is assumed, where C_D can be calculated as

$$C_D = 2\left[\frac{\kappa}{\log\left(\frac{12h}{k_s}\right)}\right]^2 \tag{3.7}$$

The bed roughness k_s can either be used as a constant (entered in the steering file) or variable in space (using the subroutine `STRCHE`). For the simulations described in this Chapter and Chapters 4 and 6 a constant k_s is used with a value of $0.05m$. However in Chapter 5 a method is implemented that calculates a varying k_s both in space and time, applying the predictive formulae of Van Rijn (2007).

Bed-load sediment flux

In simulations where the bed load sediment flux Q_b was calculated (Chapters 4 and 6) the formula of Van Rijn (1984a) was adopted, which reads

$$\Phi_b = 0.053{D_*}^{-0.3}\left(\frac{\theta' - \theta_{cr}}{\theta_{cr}}\right)^{2.1} \tag{3.8}$$

where Φ_b is the non-dimensional bed load sediment transport rate, related to the volumetric bed load transport rate Q_b by

$$\Phi_b = \frac{Q_b}{\left[g(s-1){D_{50}}^3\right]^{1/2}} \tag{3.9}$$

where s is the sediment relative density ρ_s/ρ and D_* is the non dimensional grain size, calculated from

$$D_* = \left(\frac{g(s-1)}{\nu^2}\right)^{1/3} D_{50} \tag{3.10}$$

where ν is the fluid viscosity and D_{50} is the median grain size. The critical Shields parameter θ_{cr} is calculated by `SISYPHE` using the method of Van Rijn (1993). Here the value of θ_{cr} is set based on D_* so that

$$\begin{aligned} \theta_{cr} &= 0.24D_* & D_* &\leq 4 \\ \theta_{cr} &= 0.14{D_*}^{-0.64} & 4 < D_* &\leq 10 \\ \theta_{cr} &= 0.04{D_*}^{-0.1} & 10 < D_* &\leq 20 \\ \theta_{cr} &= 0.013{D_*}^{0.29} & 20 < D_* &\leq 150 \\ \theta_{cr} &= 0.045 & 150 &\leq D_* \end{aligned} \tag{3.11}$$

Van Rijn's formula was adopted firstly due to the appropriateness of the formula for use in sandy sediments ($0.2mm \leq D_{50} \leq 2mm$) and secondly due to its explicit use of the critical Shields parameter θ_{cr}, which was utilised in the setting of a probabilistic threshold of motion (described in Chapter 6).

Total-load sediment flux

In simulations where the total load sediment flux was calculated (Chapter 5) the formula of Bijker (1968) was adopted. The formula is able to take into account the effect of waves through an enhanced bed shear stress τ_{cw} so that

$$\tau_{cw} = \tau_c + \frac{1}{2}\tau_w \tag{3.12}$$

where τ_c is the bed shear stress due to currents alone and τ_w is the bed shear stress due to waves. For the present body of work no wave-current interaction was simulated, so that $\tau_w = 0$ and $\tau_{cw} = \tau_c = \tau_0$. The total load transport rate Q_s is split into the bed load Q_b and suspended load Q_{ss} with each calculated separately. The volumetric bed load transport rate is calculated as

$$Q_b = 2\theta' \exp\left(-0.27\frac{1}{\mu\theta'}\right)\left[g(s-1){D_{50}}^3\right]^{1/2} \tag{3.13}$$

where μ is a ripple correction factor, calculated as $\mu = C'_D/C_D$ where C'_D is the small-scale (i.e. ripple) component of the drag coefficient. The suspended load contribution is calculated assuming a Rouse sediment concentration profile and a logarithmic velocity profile so that $Q_{ss} = Q_b I$, where

$$I = 1.83 \times 0.216\frac{B^{A-1}}{(1-B)^A}\int_B^1 \left(\frac{1-z'}{z'}\right)^A \ln\left(\frac{33z'}{B}\right)dz' \tag{3.14}$$

where z' is the dimensionless height. For the case of currents alone, A and B are calculated from

$$A = \tfrac{w_s}{\kappa u_*} \quad B = \tfrac{k_s}{h} \tag{3.15}$$

Equation 3.14 is solved in `SISYPHE` via an Einstein integral and combined with Equation 3.13 to calculate the total load sediment transport rate Q_s.

Bed slope and sediment slide effects

The bed-slope correction of Koch & Flokstra (1981) to the magnitude and direction of Q_b was implemented to help smooth out bed evolutions which become steeper than the angle of sediment repose ϕ_s so that

$$Q_b = Q_b\left(1 - \beta\frac{\partial z_b}{\partial \gamma}\right) \tag{3.16}$$

where β is a slope coefficient (set here to $\beta = 1.3$) and γ is the along-flow coordinate. The effect of equation 3.16 is to increase the rate of bed load transport down-slope (for $Q_s > 0$) and to decrease the transport rate up-slope due to the force of gravity. The direction of the bed load sediment flux is modified by

$$\tan\alpha = \tan\alpha_\tau - T\frac{\partial z_b}{\partial \gamma'} \tag{3.17}$$

where α and α_τ are the directions of Q_b and τ_0 in relation to the flow direction respectively and γ' is the coordinate along an axis perpendicular to the flow. T is a scaling parameter which in this case is

$$T = \frac{4}{6\theta'} \tag{3.18}$$

The effect of this modifier is to veer the direction of the bedload flux in the down-slope direction depending on the magnitude of the bed slope and the flow conditions (represented by the Shields parameter through T). To ensure that the bed slope does not exceed the angle of sediment repose an iterative process is undertaken at each time step to ensure the validity of the condition

$$\left\| \overrightarrow{\mathrm{grad}}(z_b) \right\| < \tan(\phi_s) \tag{3.19}$$

where $\phi_s \approx 32°–40°$

3.5 Parallel processing

Since `TELEMAC 2D` version `5.9` an option for parallel processing of the model run across multiple computer processor cores has been possible, allowing for significantly increased computation speed. The option is activated with the steering file keyword `PARALLEL PROCESSORS` which contains an entry for the number of processor cores to be used. A multiple processor implementation (MPI) subroutine then splits the `FORTRAN`, geo, conlim and formatted input files (e.g. previous results files, spin-up run, etc.) into a number of segments coincident with the number of processors used. The grid is split into sections with a relatively equal number of grid nodes (figure 3.6) which upon the end of a simulation are combined into a single, original grid. To test the effect of increasing numbers of parallel processors on computation speed a simple, arbitrary model was constructed with a domain 100m long and 10m wide with a constant depth of 5m (flat bed). The boundary conditions consisted of a free surface at both liquid boundaries (left and right-hand edges of the rectangular domain) and fixed hU and hV fluid flux components of 10 and

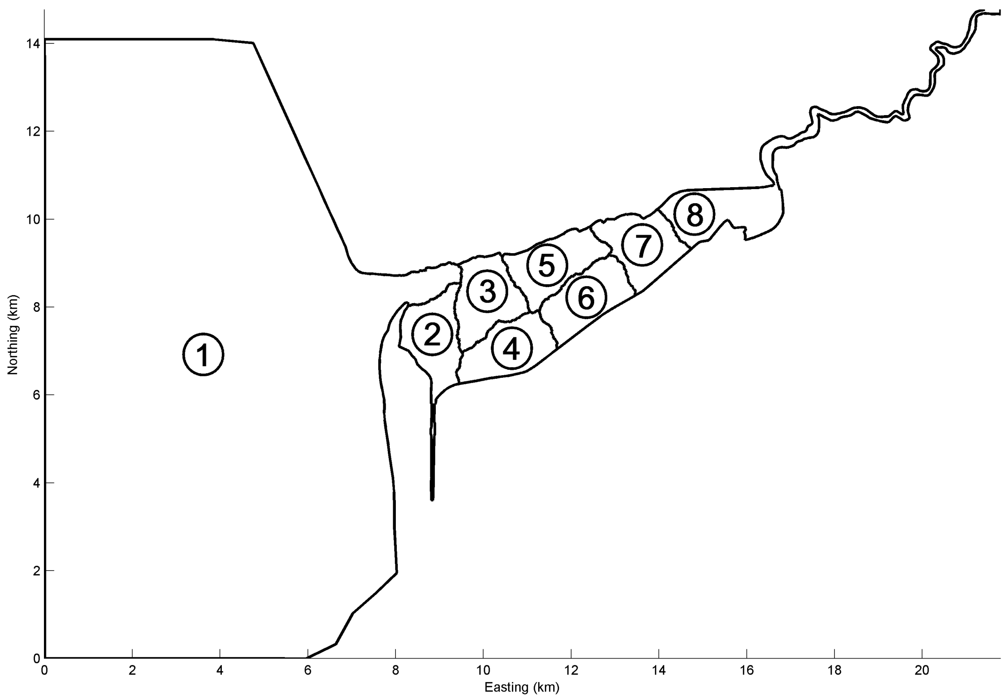

Figure 3.6 – Example of a grid segmented for the use of 8 parallel processors. The region governed by each processor contains a relatively equal number of grid nodes, but as can be seen in this particular example the areas governed may not be equal due to differences in mesh resolution across the model domain.

$0m^3s^{-1}$ respectively at the left-hand boundary (i.e. flow into the domain) and -10 and $0m^3s^{-1}$ respectively at the right-hand boundary (flow out of the domain). This produced a constant flow velocity of $0.5ms^1$ throughout the domain after spin-up.

The model was run for 1,000 iterations and the time to run completion was recorded for increasing numbers of parallel processors (figure 3.7). The speed-up (reciprocal of the time to completion relative to the run time for a single processor) is seen to keep pace with the number of processors at low numbers (i.e. two cores halves the run time, three cores gives 1/3 of the run time). However as the number of parallel processors is increased so are the number of calls that are made between the processors and the computer memory (both RAM and hard disk) which become increasingly significant. As these calls to memory require time to execute, the relative speed-up is decreased so that for 8 processors only around 1/5th of the run time was observed. This is not to be taken as a universal figure however, as different grids (both in size and in complexity) will behave differently in terms of parallel speed-up—for example a change in the point of inflection from the 1:1 speedup curve. However due to the fact that computer architecture demands an increasing number of calls to memory for larger numbers of processors involved in a computation it is expected that a speed-up curve like that in figure 3.7 provides a good general representation for parallel computation in `TELEMAC 2D`.

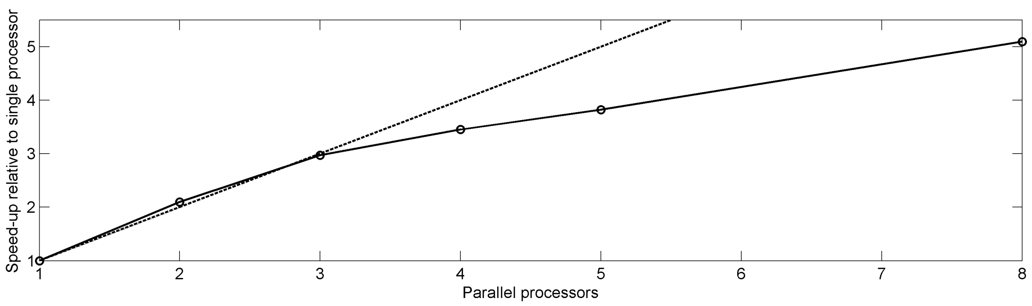

Figure 3.7 – Speed-up in computation time (solid line) for increasing numbers of parallel processors for a simple, arbitrary model case. Dashed line represents a 1:1 speed-up/processor rate. The rate of speed-up decreases with increasing numbers of processors as communication time between cores and the disk becomes increasingly significant.

3.6 Long-term morphological modelling with `SISYPHE`

Before version `SISYPHE v5.8`, long-term, coupled morphological runs could be implemented by the use of so-called 'Tide lengthening' whereby the time-step of `SISYPHE` was increased relative to that of `TELEMAC 2D`. This had the effect of increasing sediment transport fluxes for a given flow speed and therefore increasing bed evolution per time-step.

After the Tide lengthening scheme was removed in `v5.8`, `SISYPHE` was essentially left without a robust and simple method to reduce the time needed for coupled morphological runs while avoiding input reduction techniques. It was decided, therefore, to adapt the `SISYPHE` code to follow the Morphological Factor method of Roelvink (2006). This was a simple change to the code, as the only requirement is that the bed evolutions calculated at the end of the coupling period are multiplied by some factor MF before the updated bed evolutions are passed back to `TELEMAC 2D` prior to the next time-step. The MF method is coded into `SISYPHE` immediately after bed-load and suspended load transport rates have been calculated and their respective contributions to the bed evolution have been combined (for the `SISYPHE` code, see Appendix IV).

3.6.1 MF method considerations

It is important at this stage to highlight some considerations concerning the use of the MF method in morphological modelling—especially with respect to its use in making predictions of morphology over the medium to long term.

The core concept of the MF method is that morphology exists in a different and longer reference frame than that of the hydrodynamics—or in other words, morphology 'experiences' time at a slower rate relative to the hydrodynamics. For example the number of tides required to create a morphological feature such as an intertidal sand bank may be much greater than one, whereas the flow over that morphological structure will experience constant and dynamic change during a single tidal period. An alternative way of describing this phenomenon is that the hydrodynamics react almost instantaneously to a change in morphology, while morphological evolution is the product of *cumulative* hydrodynamic forcing. In this way the MF method should not be viewed as a simple and arbitrary 'speed-up' but a way of 'stretching' a morphological reference frame with regard to its coupled hydrodynamics. A good example of this is the use of the MF method in a tidal situation. If the MF coefficient is to represent N tidal cycles then it is effectively assumed that the morphological evolution with $MF = N$ will be equal to that of N tides of evolution in real-time.

In principle it is therefore important (especially with high MF coefficients) that the length of simulation corresponds precisely to an integer number of tidal wave repeat periods—that is to say the simulation should end on exactly the same tidal elevation and phase as that on which it began. If this is not the case the MF method 'speed-up' will be applied unequally on different stages of the tide, i.e. the final result may have been the result of more flood tides than ebb tides. In the case of a single harmonic tide the simulation length should simply be a multiple of the tidal period. However for multiple tidal constituents (as is common in full-scale, natural tidal basin models) the repeat length will be much greater. For two constituents (eg the principal lunar and solar tidal periods M_2 and S_2) the repeat period T_r is

$$T_r = \frac{M_2 S_2}{M_2 - S_2} \tag{3.20}$$

In the case of $M_2 + S_2$ (a spring-neap tide) this corresponds to approximately 14.5 days. Therefore for a spring-neap simulation with the MF method applied the simulation must be *at least* T_r long or a multiple of it. This may not be such a limiting constraint, however with more tidal constituents the repeat length becomes longer, and in the case of a tidal simulation with 9+ tidal constituents the repeat period may be unacceptably long.

3.6.2 The use of waves

`TOMAWAC`, the wave module of `TELEMAC 2D`, has been implemented successfully in the past to perform medium-term morphological simulations (Brown & Davies, 2009). However the current release of `TELEMAC 2D` (v6.1 at the time of writing) is unable to internally couple `TOMAWAC` alongside `TELEMAC 2D` and `SISYPHE`. `TOMAWAC` is at present only capable of simulating a wave field for a given hydrodynamic situation - i.e. the water depth and flow velocities are static. Therefore to use `TOMAWAC` in a tidal setting the hydrodynamic simulation must be interrupted periodically in order to re-calculate the wave field, a process which carries a heavy time cost. For morphological simulations consisting of many hundreds of tidal periods this module chaining method would be unacceptably long. Wave simulations have for this reason been omitted from this body of work. This raises many interesting and critical points, not least on the validity of predictions in areas where waves may have a significant impact on sediment transport. The implications of this omission are explained in more detail in subsequent chapters.

3.6.3 MF method testing

To test the effect of the MF coefficient on morphological evolution a simple test case was set up. The model grid was $100m$ in x and $10m$ in y with a constant grid resolution of $1m$, producing a grid with 5,000 mesh nodes. The average depth was $2.5m$ with a $1m$ high 'hump' in the centre of the domain with symmetrically sloping sides (facing the flow) and a constant cross-section in y (figure 3.8). Two models (low- and high-flow cases) were spun-up with a time-step of $0.1s$ for 50,000 iterations to a steady current driven by inflows of $10m^3s^{-1}$ and $20m^3s^{-1}$ respectively, creating depth averaged flow speeds of $0.4ms^{-1}$ over the flat section and $0.67ms^{-1}$ over the hump crest for the low-flow case and $0.8ms^{-1}$ and $1.4ms^{-1}$ respectively for the high-flow case (figure 3.9). `SISYPHE` was run in internally coupled mode with a constant grain size of $200\mu m$ and sediment transport calculated by Van Rijn's bed-load transport equation with 'sediment slide' and bed-slope effects activated.

For the benchmark cases (MF = 1, i.e no speed-up), the models were run for 1,000,000 iterations (appx. 27 hours of hydrodynamic time), taking over 3.5 hours of run time with 4 parallel processors. The simulations were then repeated with increasing MF coefficients, each time reducing the number of iterations accordingly, i.e. stretching the hydrodynamic reference frame so that an iteration represents a greater length of morphological time. For example at MF = 5 the number of iterations reduced to 200,000 and for MF = 500 to 2,000. The two test cases were run for MF coefficients of 1, 5, 10, 50, 100, 200, 500, 800, 1000, 2000, 5000 and 10,000.

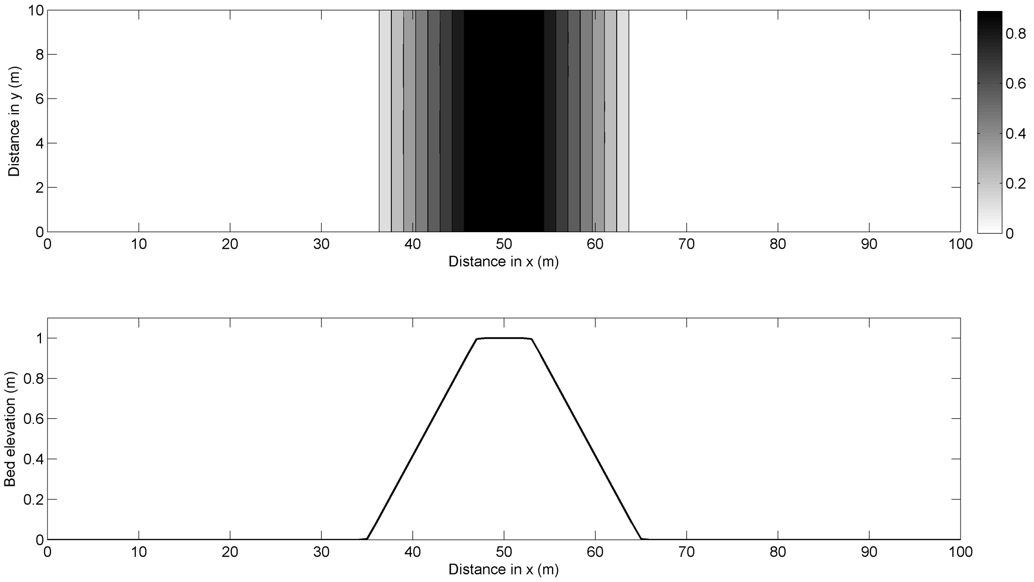

Figure 3.8 – Contour plot of the plan-form bathymetry of the test case model grid with bed elevation contours in m (top) and a profile of grid bathymetry through the centreline $y = 5m$ (bottom)

Results

The relative accuracy of each MF case was evaluated by its difference to the benchmark case. To do this the grid was reduced to a 1D slice through the centreline $y = 5$ and the bed elevation profile z at the end of the model run (which in each case corresponded to the same morphological time) compared (figure 3.10). In both cases the general morphodynamic trend was for the 'hump' to migrate downstream and become more asymmetrical in shape, with evolution in the high-flow case significantly greater than that in the low-flow case. Interestingly, the total evolution and migration of morphology decreased for increasing MF coefficient (especially the MF $= 10,000$ run in the high-flow case). This is due to the fact that although evolution per time step is increasing with MF coefficient the total number of iterations modelled is decreasing. Morphological evolution and hydrodynamics exist in a feedback relationship—morphological change drives changes in hydrodynamics which further affect morphological development.

To quantify the error in prediction for increasing MF coefficient the Brier

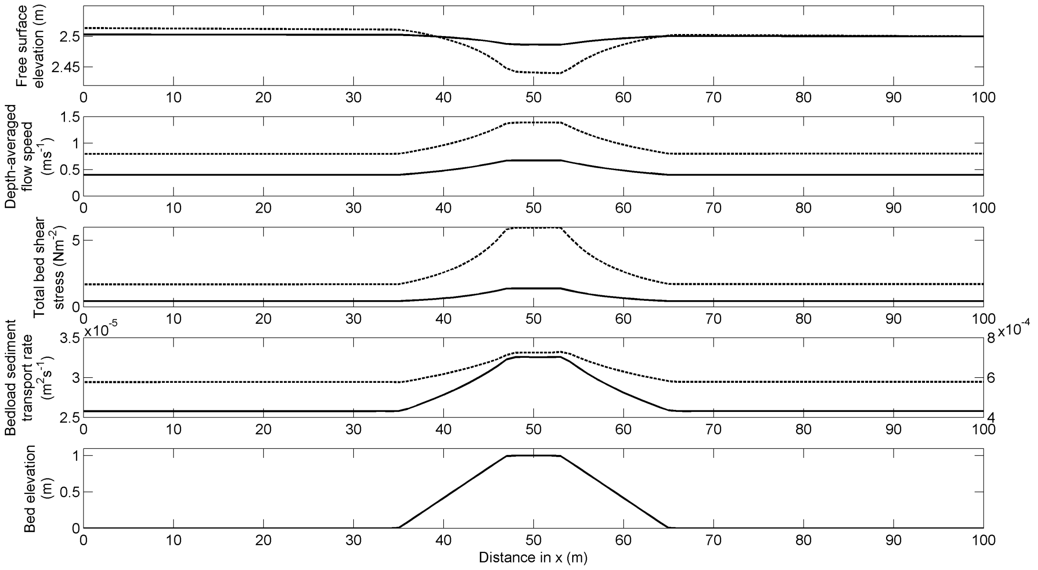

Figure 3.9 – Initial plots of hydrodynamic variables and the resulting sediment transport from the low-flow (solid lines) and high-flow (dashed lines) cases. Data obtained from the first time step after spin-up. From top to bottom: Free surface elevation, depth-averaged flow speed, bed shear stress, sediment transport magnitude and the underlying bathymetry. Bed-load sediment transport varied by an order of magnitude between the two test cases - the y axes show magnitudes for the low-flow case on the left and high-flow case on the right.

Skill Score (BSS) was implemented, calculated from the definition of Van Rijn et al (2003), so that

$$\mathrm{BSS(MF)} = 1 - \frac{\left\langle \left(z_b - z_{b,MF=1}\right)^2 \right\rangle}{\left\langle \left(z_{b,0} - z_{b,MF=1}\right)^2 \right\rangle} \tag{3.21}$$

where z_b is the final bathymetry predicted for each MF case, $z_{b,MF=1}$ is the final bathymetry predicted by the benchmark case, $z_{b,0}$ is the initial bathymetry and the angle-brackets denote averaging across all mesh nodes. A BSS value of 1 indicates an identical match between predictions, any deviation from this value indicates an increasing degree of error. The BSS was calculated for each MF coefficient over both cases (figure 3.11) and a general divergence away from unity was observed in both high-flow and low-flow cases. The degree of error was generally greater in the high-flow case with

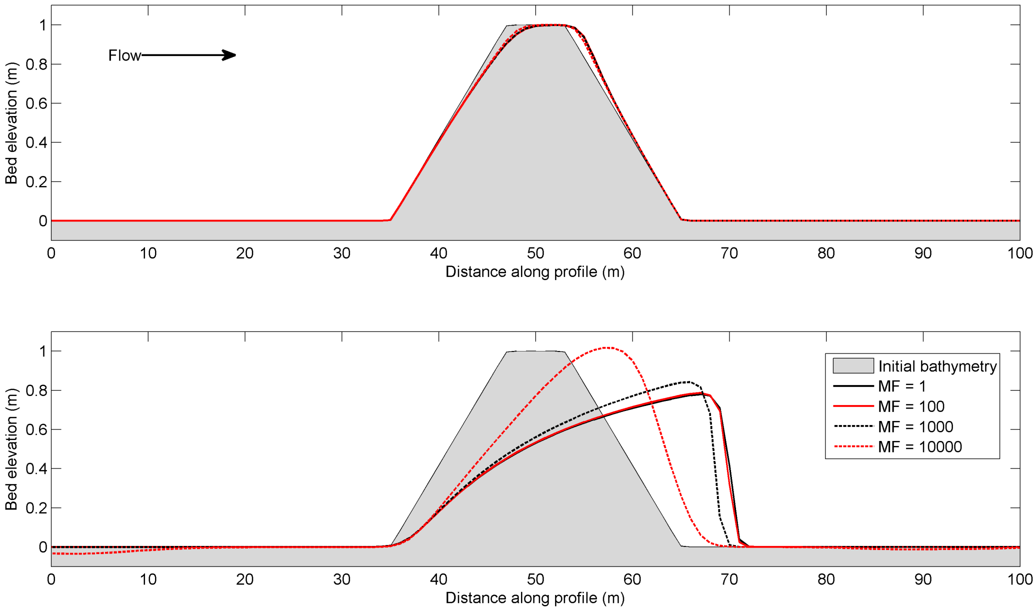

Figure 3.10 – Initial and final bathymetries for the low-flow (top) and high-flow (bottom) cases. The initial bed elevation profile (grey, shaded area) is in each case modified and transported downstream (to the right). The final bathymetries (solid and dashed red and black lines) show different magnitudes of evolution for increasing MF coefficient.

a larger divergence from unity at high MF coefficients. The use of the BSS here could be to determine the maximum MF coefficient which can be used at a given minimum BSS. The minimum acceptable BSS value varies between applications, from as low as 0.5 (Van Rijn et al, 2003) and as high as 0.99 (Ranasinghe et al, 2011). Taking a BSS of 0.99 as an indication of the maximum acceptable error, the maximum MF coefficient varies between 125 (high-flow) and $\approx 2,000$ (low-flow). It is clear that the relative activity of the system being modelled has a significant influence on numerical stability when using large MF coefficients. In a tidal environment it would not be uncommon for the mean flow to vary between the two flow states modelled here. It is therefore assumed that the maximum MF coefficient for a tidal morphological model should lie somewhere in the region $100 \leq \text{MF} \leq 2,000$. However to fully ascertain the maximum MF coefficient for a given model, runs must be made consisting of a great number of iterations (for the $\text{MF} = 1$

case especially) which may not be feasible for large and complicated grids. In the case of the simulations in the present body of work, a MF coefficient of 705.3456 was implemented. Firstly, this ensured a M_2 tidal period of $44712s$ equated exactly 1 year of morphological time. Secondly, the equivalent BSS score of the low- and high-flow states depicted in figure 3.11 fall above 0.9 which was deemed sufficiently high enough not to introduce significant changes of morphological evolution over a simulation without MF speedup.

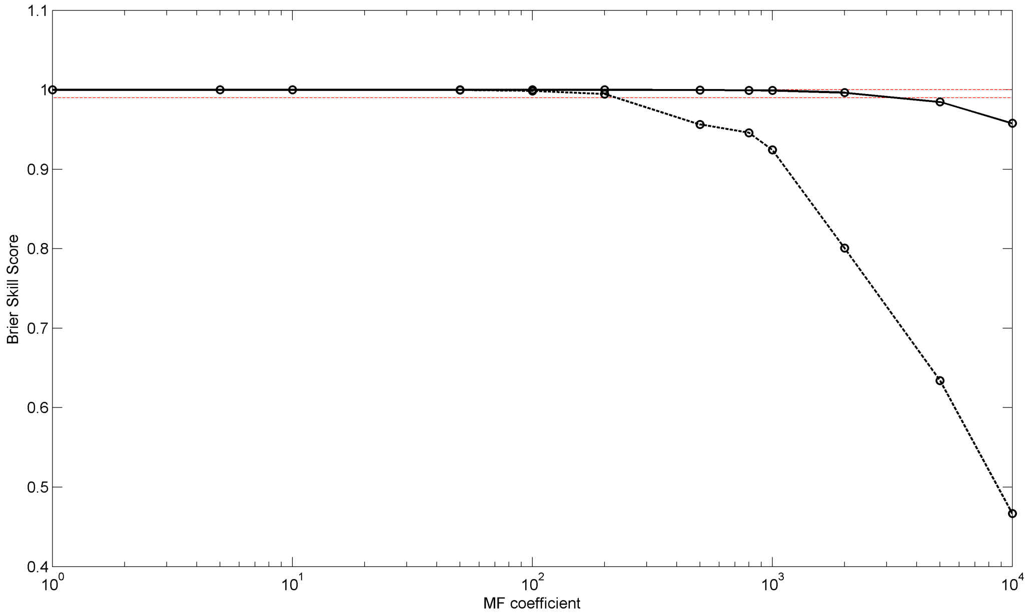

Figure 3.11 – Brier Skill Score (BSS) of morphology predicted using an increasing MF coefficient for the low- and high-flow cases (solid and dashed black lines respectively. The two red dotted lines represent a BSS of 1 (perfect agreement) and 0.99.

3.7 Stability of sediment advection-diffusion and the MF method in `SISYPHE`

When transporting sediment as suspended load, `SISYPHE` is able to use an Advection-Diffusion (A-D) scheme to model the transport of the depth-averaged suspended sediment concentration C (following an assumed Rouse profile) between grid nodes by advection (via sediment convection velocities) or direct diffusion between nodes via a sediment diffusivity ϵ_s, so that

$$\frac{\partial C}{\partial t} + \underbrace{U_{conv}\frac{\partial C}{\partial x} + V_{conv}\frac{\partial C}{\partial y}}_{Advection} = \underbrace{\frac{1}{h}\left[\frac{\partial}{\partial x}\left(h\epsilon_s\frac{\partial C}{\partial x}\right) + \frac{\partial}{\partial y}\left(h\epsilon_s\frac{\partial C}{\partial y}\right)\right]}_{Diffusion} + \frac{(E-D)_{z=z_{ref}}}{h} \tag{3.22}$$

where $(E-D)_{z=z_{ref}}$ is the net erosion minus deposition at the bed (specifically at the reference level z_{ref}), determined via an equilibrium concentration C_{eq}

$$(E-D)_{z=z_{ref}} = w_s\left(C_{eq} - C_{z_{ref}}\right) \tag{3.23}$$

where w_s is the sediment settling velocity. Although it may be favourable to adopt an A-D transport scheme for morphological modelling there are significant stability issues when used in conjunction with the morphological factor method. The problem arises in the form of Courant-Friedrichs-Lewy (CFL) numerical instabilities which invade the system and grow exponentially until the model crashes. In the case of `TELEMAC` such a crash is usually due to a bed evolution during a single time-step which is greater than the flow depth, most often resulting in a divide-by-zero in the hydrodynamic equations.

The instabilities arise from the combination of multiple morphological feedback loops. In an equilibrium bed update model there is a single feedback loop between bed evolution and the hydrodynamics: As the bed is eroded or deposited there is a change in flow depth that directly affects flow speed—and therefore sediment transport and subsequent bed evolution. In the case of the A-D scheme a change in the flow also affects the depth averaged concentration and therefore the suspended sediment transport rate (and subsequent evolution). However due to the advection term this affect on suspended sediment transport can be non-local. Although there is also a non-local feedback loop in the equilibrium bed model (through the advection of depth in the hydrodynamic equations) this is compounded by the second non-local feedback loop introduced by the sediment A-D scheme. The combination of the two is believed to cause the numerical instabilities found in this body of work.

To address the issue a stability criterion was developed based on the CFL number, defined by Courant et al. (1967) as

$$\mathrm{CFL} = c\frac{\delta t}{\delta x} \tag{3.24}$$

where c is an advection velocity, t is time and x is distance. In this way the CFL number is a percentage of a finite distance δx (e.g. a discreet grid cell) that will be travelled in a given time δt (in this case the model time-step). As a rule of thumb the stability threshold is usually set at 0.2, meaning that no more than 20% of a grid cell can be advected over (e.g. by a parcel of fluid, a wave, etc.) in any one time step. `SISYPHE` calculates a sedimentological CFL number based on sediment fluxes and depth gradients. The bed evolution equation for the AD scheme reads

$$(1-n)\frac{\partial z_b}{\partial t} + Div\left(\vec{Q_s}\right) + (E-D) = 0 \tag{3.25}$$

that can be re-written in terms of the sediment flux Q_s as

$$(1-n)\frac{\partial z_b}{\partial t} + \frac{\partial Q_s}{\partial h}\frac{\partial h}{\partial x} + \frac{\partial Q_s}{\partial h}\frac{\partial h}{\partial y} = 0 \tag{3.26}$$

`SISYPHE` calculates a sedimentological criterion CFL_s based on the sediment advection field $\vec{\mathrm{CONV}}_s$ where

$$\vec{\mathrm{CONV}}_s = \left(-\frac{Q_{s,x}}{Q_s}\frac{\partial Q_{s,x}}{\partial h}, -\frac{Q_{s,y}}{Q_s}\frac{\partial Q_{s,y}}{\partial h}\right) \tag{3.27}$$

so that

$$\mathrm{CFL}_s = \frac{\left\|\vec{\mathrm{CONV}}_s\right\|\delta t}{\delta x} \leq 0.2 \tag{3.28}$$

When using a MF number > 1 the morphological reference frame is elongated, i.e. the time-step is effectively increased. Therefore a first approximation for a morphological criterion CFL_m could be

$$\mathrm{CFL}_m = \mathrm{MF}\frac{\left\|\vec{\mathrm{CONV}}_s\right\| \delta t}{\delta x} \tag{3.29}$$

Therefore for a system that is approaching instability, and with a MF number of 100 in use, either the time-step would have to be 100 times longer or the grid spacing 100 times smaller, an adaptation to the model which is unacceptable. The problems of run-away numerical instabilities arise from an unsuitable time-step or mesh resolution for the magnitudes of transport involved, which are subsequently amplified by the MF number. However if stability is compromised in only a few discrete locations in the grid it may be possible to place an upper limit on bed evolution over a single time-step based on the above criterion.

With the simplifying assumption that suspended sediments advect at the same rate as the current, $\partial Q_s/\partial h$ from the A-D equation may be taken as equivalent to the advection velocity U_{adv}. Taking the original CFL threshold of 0.2 then for stability at a given MF number

$$\mathrm{MF}\frac{U_{adv}\delta t}{\delta x} = 0.2 \tag{3.30}$$

Therefore the maximum advection velocity $U_{adv,max}$ could be taken as

$$U_{adv,max} = \frac{0.2}{\mathrm{MF}}\frac{\delta x}{\delta t} \tag{3.31}$$

The bed evolution equation for a particular grid cell over a single time-step can be re-written, replacing Q_s in 3.25 so that

$$-\left(1-n\right)\frac{\delta z_b}{\delta t} + U_{adv}\frac{\delta h}{\delta x} = 0 \tag{3.32}$$

If free-surface slope across a grid cell is taken to be approximately equal to 0, the maximum possible depth change over a grid cell is simply the sediment angle of repose (above which sediment will avalanche down-slope) which for spherical grains is equal to a gradient of approximately 0.62 (Soulsby, 1997) so that

$$\left(\frac{\delta h}{\delta x}\right)_{max} = 0.62 \tag{3.33}$$

Combining equations 3.31,3.32 and 3.33, the maximum bed level change per grid cell per time step based on the CFL criterion and the MF number is approximately

$$\left(\frac{\delta z_b}{\delta t}\right)_{max} \approx 0.62\frac{U_{adv,max}}{(1-n)} \tag{3.34}$$

This may be expressed alternatively in terms of the change in bed level (the evolution) calculated by `SISYPHE` over a time step

$$|\delta z_b|_{max} \approx \frac{1}{8}\frac{\delta x}{\mathrm{MF}\,(1-n)} \tag{3.35}$$

which taking the bed porosity n to be equal to 0.4 (as for spherical grains) is approximately

$$|\delta z_b|_{max} \approx \frac{1}{5}\frac{\delta x}{\mathrm{MF}} \tag{3.36}$$

Therefore over the course of a time step bed-level change should not exceed a level determined by the grid node spacing and the MF number. For example if the grid node spacing is $50m$ and the MF number is set to 100 the maximum allowable evolution per time step is $10cm$.

3.7.1 MF-CFL criterion testing

Equation 3.36 was tested against a simple steady flow model case. The domain was rectangular, 200m long and 20m wide, with a constant grid resolution of 1m and constant depth of 5m below the mean free surface. Hydrodynamic forcing was provided by a fixed free surface gradient of 1×10^{-4} generated by fixed free surface elevations at the left and right (in-flow and out-flow) boundaries. Fluid flux was free across both liquid boundaries allowing the model to generate the appropriate flux for the given free surface slope. After initial instabilities had disappeared after a period of spin-up a constant depth averaged flow speed of $0.75ms^{-1}$ was observed.

For the sediment transport module the AD equations were activated, using Zyserman & Fredsøe's (1994) definition of C_{eq} and the bed-load transport formula of Van Rijn (1984a). Both grain size and the MF number were varied between runs—the grain size being varied as it has a direct effect on the total sediment flux (and therefore maximum evolution per time step). Grain size was varied between $100\mu m$ and $500\mu m$. Simulations were run for $50,000$ iterations or until the model became unstable, identified by the emergence of very large bed evolutions of the order of $1m/\delta t$. The maximum bed evolution (combined effect of bed load and suspended load transports) per time-step was recorded for each case and compared with equation 3.36 (figure 3.12) For this simplified scenario it was found that the derived stability criterion

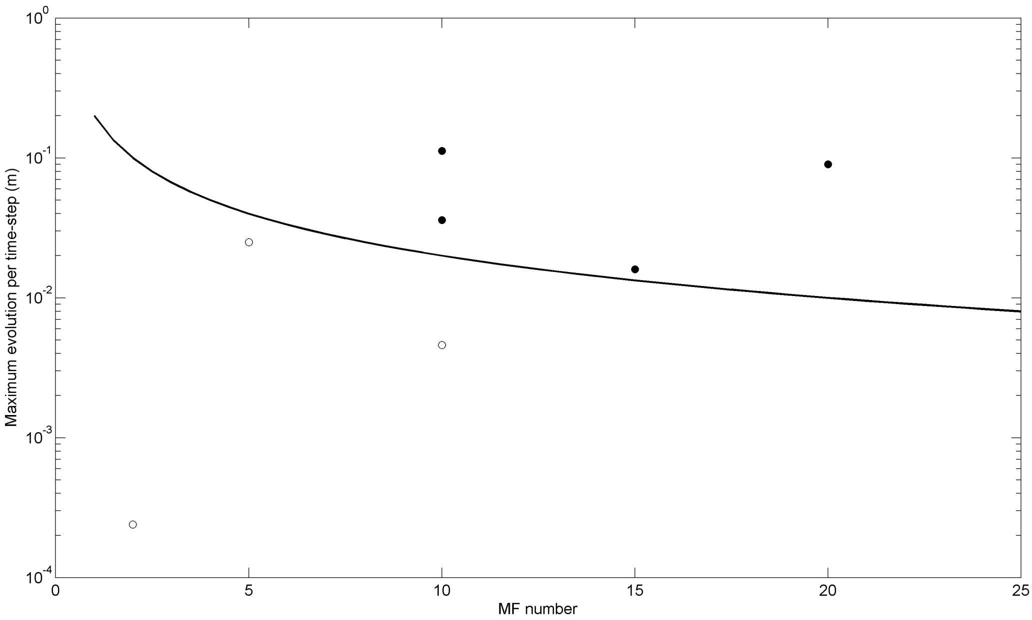

Figure 3.12 – The maximum evolution per time step vs. MF coefficient for seven test cases. Un-filled circles represent model runs which remained stable indefinitely while filled circled represent models which eventually became unstable. The line corresponds to equation 3.36

correctly identified unstable model runs based on the accelerated rate of bed evolution from the MF method. During testing it was noted that MF coefficients greater than 10 would only allow stable runs with relatively large grain sizes ($500\mu m$)—grain sizes which would not normally be transported by suspended load in the natural environment. Unfortunately, fine grain fractions which are most suitable for suspended transport also are transported en-masse via bed-load and contribute to large bed evolutions which eventually cause instabilities in the model through their interaction with the AD equations.

It is therefore concluded that for applications where suspended sediment transport by advection-diffusion schemes is required in `SISYPHE`, the MF method is incompatible in the present form of internal morphological coupling. Further investigation is required (including a full analytical study) of the relationship and interaction between the AD equations and MF method enhanced morphological modelling in `TELEMAC 2D` + `SISYPHE` to asses whether this incompatibility can be overcome with enhancements to the program code.

Chapter 4

The morphological evolution of a sandy, tidal basin

4.1 Introduction

At the time the work described below was conducted the current version of `TELEMAC 2D` (`5.9`) contained no in-built provision for the widely-adopted Morphological Factor approach to bed level update when internally coupled with `SISYPHE`. To test the suitability of the `TELEMAC` modelling system for use with the MF method extensive trials were conducted to asses the presence and cause of instabilities (if any), as well as investigate the limitations of the MF method when applied in conjunction with certain subroutines (much of which was discussed in section 3.6.3).

In this chapter a simple, long-term morphological model trial is introduced and the results of 100 years of morphological evolution discussed. The model is of a long, narrow and deep schematised tidal basin similar to that of Hibma et al. (2003) which was used as a proof-of-concept model to attempt to reproduce results obtained in a similar setting but with a finite-difference type model (namely Delft 3D).

4.2 Mesh generation, boundary conditions and model set up

The schematised tidal basin was designed to emulate the model domains of Hibma et al. (2003; 2004a), Van der Wegen & Roelvink (2008) and the long, narrow and deep tidal embayments in the Netherlands which were described by Van Veen et al. (2005). Using the mesh generation and pre-processor package BlueKenue, a rectangular basin 50km long and 2km wide was constructed, with a constant mesh resolution of 50m (figure 4.1), a linearly sloping bed, shoaling from -15m at the open liquid boundary to +6m at the head (relative to mean sea level, figure 4.2) and a constant cross-sectional profile in the y-direction. Although the model boundary is perfectly rectangular the mesh does not comprise regular triangles. It would be possible to create a regularly-spaced triangular grid comprising right-angled triangular elements, however the process of 'mesh smoothing' (the adjustment of node position to create a mesh of more uniform, equilateral triangular elements) produces a non-uniform node position. This is important for the introduction of numerical non-uniformities in cross-basin bathymetry which is essential for morphological evolution from a flat bed (this is discussed later). The model consisted of a liquid boundary across the mouth (x=0km, y=0–2km) with a boundary condition of a fixed free surface elevation (imposed by the tidal elevation calculated by `BORD`) and free velocity components. The remainder of the model boundary was set to a closed condition, with a no-slip and no-flux condition throughout. Boundary conditions were set using the BOYCOTT routine described in Appendix II. The liquid boundary free surface elevation was provided by the subroutine `BORD` for a single tidal constituent (M_2) with a period of 44710 seconds and an amplitude of 3m, imposed at every point along the liquid boundary (i.e. no spatial variation in amplitude or phase). This provided a tidal range at the liquid boundary of 6m which, with the along-basin bed-slope, created an initial inter-tidal area 22km long. Model spin-up was conducted for one tidal period with a time step of 10s starting at high-slack water. To achieve this the free-surface level of the entire basin was set to a constant +3m. The tidal elevation at the mouth then began to drop

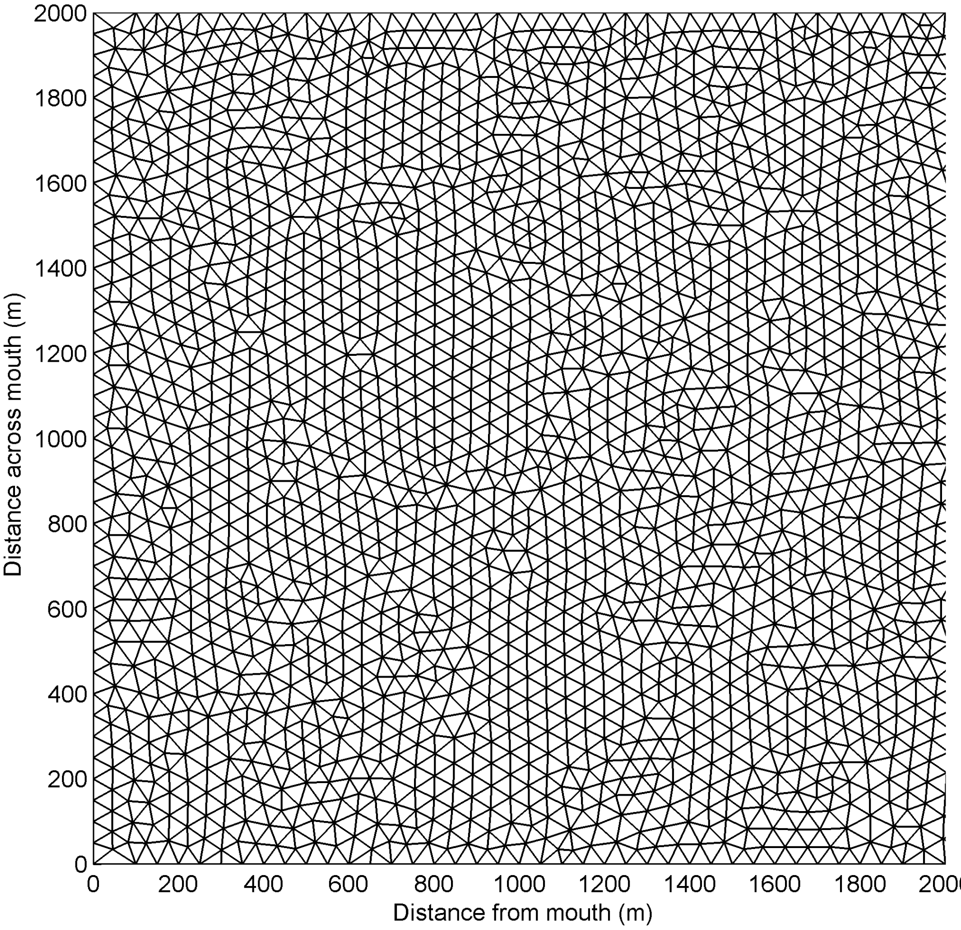

Figure 4.1 – Example area of the schematised tidal basin mesh. Note that although the mesh resolution is a constant 50m there are variations in the node positions due to mesh smoothing.

with the tide, slowly emptying the basin of water. In this way the initial conditions partially represent the hydrodynamic conditions at high-slack water (tidal elevation at its maximum and zero current velocities). This negates the need for long spin-up times as the model is not 'shocked' by hydrodynamic conditions which are vastly different from those being imposed at the tidal boundary. The spin-up results file was checked for instabilities (in both free surface and velocity) before proceeding.

The `SISYPHE` steering file was set up for a uniform sediment grain size of $200\mu m$ and the use of the bed load transport equation of Van Rijn. This was

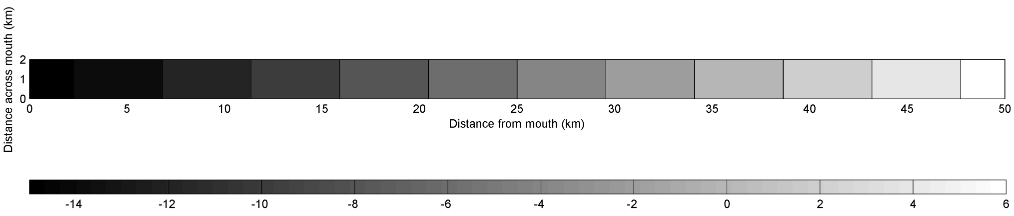

Figure 4.2 – Bathymetry (contours in m relative to mean sea level) of the schematised tidal basin model.

chosen over a total-load equation for simplicity and to emulate the result of previous investigations found in the literature. Bed slope and sediment slide effects were activated and a uniform bed roughness of 0.05m was applied to the entire basin. A morphological factor of 705.3456 was applied to bed evolutions per time step. This was chosen so as to maximise run speed-up while minimising impact on the result (see section 3.6.3). This particular choice of MF coefficient produces a year of morphological time for every tidal period (44710s) of hydrodynamic time. With a result file print-out period of 263 time steps this gives exactly 17 result entries per morphological year (or tidal period). This is important as it allows precise averaging over tidal periods thus providing accurate residual results. After spin-up, the model was run for 100 morphological years (100 tidal cycles or approximately 50 days hydrodynamic time) in coupled mode. This was to provide the basin enough time to develop an extensive tidal channel network.

4.2.1 Limitations

It is important to note that the presented model has a number of limitations and shortcomings that affect its ability to simulate certain aspects of tidal basin morphology. Firstly, the choice of grid resolution (50m) places a lower limit on the spatial scale of morphological structures that can be simulated. Combined with the 2DH implementation of hydrodynamic processes (depth-averaging) this prevents the simulation of bed form dynamics (e.g. dunes) that have an impact not only on local morphological development but have a cumulative effect over the long-term (e.g. through bed form migration). The choice of sediment transport formula (bed load only) and single grain size also limit the simulation to large-scale, average processes that may not be totally indicative of a natural system (e.g. an estuary).

The MF method essentially elongates the reference frame of morphological evolution relative to the hydrodynamics. Depending on the simulation time-step the choice of MF coefficient will have a direct effect on the ability of the model to simulate certain morphological events. A large MF coefficient (for example the choice of coefficient in the present model) will prevent the simulation of sort-term changes. In the present case, a single tide of hydrodynamic time corresponds to a year of morphological time. Therefore only large-scale, long-term (i.e. tidal) changes are represented.

However it must be noted that the MF method does not rule out short-term, small-scale processes alone. The choice of time-step, grid resolution and treatment of the hydrodynamics (and sediment transport) have a much larger effect on the simulation outcome. As such, the following simulation results should be viewed as the general, large-scale behaviour of a long tidal basin.

4.3 Results

4.3.1 Initial hydrodynamics and sediment transport

The tidal wave is distorted as it propagates up the basin due to energy losses through bed friction resulting in both a delay in phase and a slight increase in maximum high water relative to minimum low water (tidal range). Figure 4.3 shows the tidal range along the length of the basin over the first simulated tidal cycle. Tidal asymmetry is seen to increase the tidal range to a maximum (6.71m) at approximately mid-way up-basin. The range can then be seen to decrease linearly to zero, marking the initial extent of tidal influence (42.25km from the mouth).

The effects of tidal asymmetry are evident in a time-series of hydrodynamic variables (figure 4.4). At a point 38km up-estuary (blue lines, figure 4.4) the bed remains dry for much of the tidal cycle, with tidal inundation only occurring for short periods. This results in an elongation of the duration of the ebb tide relative to the flood. Combined with the reduction in water depth towards low slack water this produces high velocities and shear stresses for longer periods during the ebb tide further up-estuary. As ebb velocities and the resulting sediment transport are directed out of the basin this results in a general *ebb-dominance* of fluid flux and sediment transport within the basin. Towards the limit of tidal influence (blue lines in figure 4.4) the hydrodynamic conditions are dominated by the shallow flow depth and the distance over which the tidal wave has had to travel. Here the tide takes on the form of a tidal pulse characterised by a short, strong flood and a long, weak ebb. As the transport of sediment is non-linearly related to U (both through the quadratic nature of the bed shear stress and the non-linearity of the bed load transport equation) and only occurs if the threshold of motion has been overcome ($\theta' > \theta_{cr}$), this pulsing flood tidal current produces a flood dominant transport of sediment towards the head of the basin. However it is evident that the sediment transport rate towards the centre and mouth of the basin (red and black lines respectively, figure 4.4) is both high in magnitude and long in duration which suggests ebb dominance towards the mouth. There is therefore a point along-basin where the bed load sediment transport switches from ebb to flood dominance, with some areas predominantly importing sediment while others are predominantly exporting. This can be seen in a plot of the tidal residual transport rates over the first tidal cycle (Figure 4.5). As the morphology has not yet begun to develop over the first tidal cycle (the first morphological year) the residual

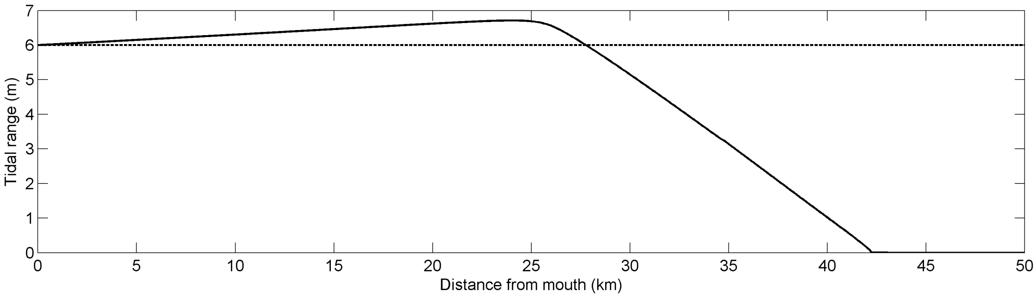

Figure 4.3 – Tidal range (difference between maximum high water and minimum low water) along the length of the basin over the first simulated tidal cycle. The dashed line at 6m denotes the tidal range at the liquid boundary.

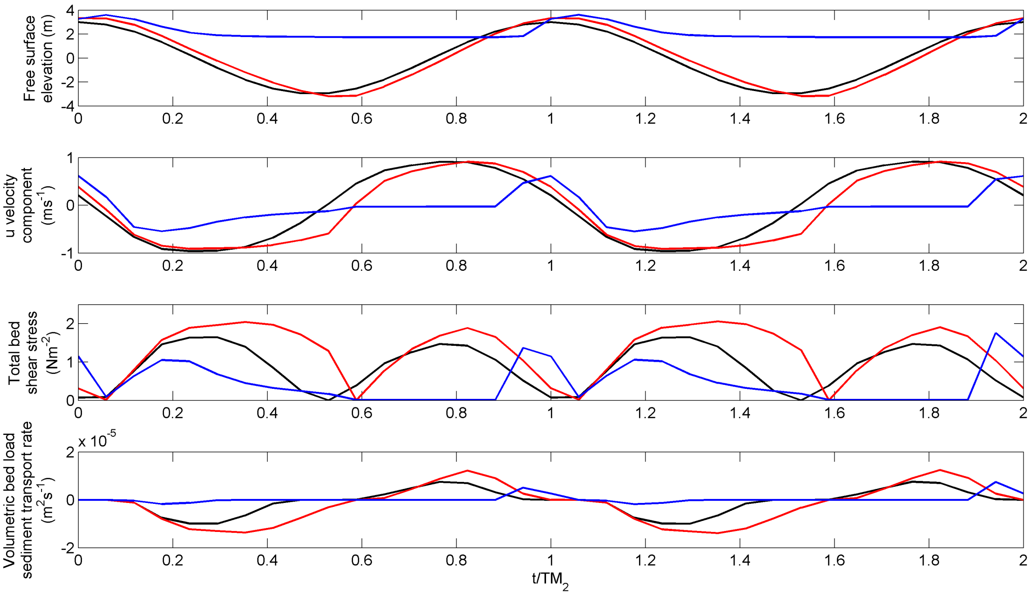

Figure 4.4 – Time series over two tidal cycles (of period TM_2) of hydrodynamic time from points in the centre of the model domain (y=1km) at the mouth (x=0km, black lines), mid-way up the basin (x=25km, red lines) and towards the limit of tidal influence (x=38km, blue lines). From top to bottom: Free surface elevation (relative to mean sea level), U component of velocity, magnitude of the total bed shear stress and in the bottom panel the x component of the volumetric bed load sediment transport rate. Positive values are in the direction of the flood tide, negative values are in the ebb direction.

components are uniform across-basin. Therefore the residuals in figure 4.5 have been averaged across-basin. The tidal residual along-basin velocity indicates the flood or ebb dominance of fluid flow. Here the basin can be seen to be ebb-dominant throughout the extent of tidal influence, with significant ebb-residual velocities of over $0.1ms^{-1}$ towards the centre of the basin. The peak in residual bed shear stress, however, is found further up-basin. This is due to the dependence of bed shear stress on flow depth which becomes increasingly shallow towards the head. Although the residual shear stress is entirely ebb-dominant the magnitude of the residual is very small as only stresses that are above the those required for the threshold of motion will transport sediment. This is evident in the available transport stress, characterised by the available Shields parameter above threshold $\theta' - \theta_{cr}$. Here the effect of the pulsing flood tide at the reaches of tidal influence is evident in

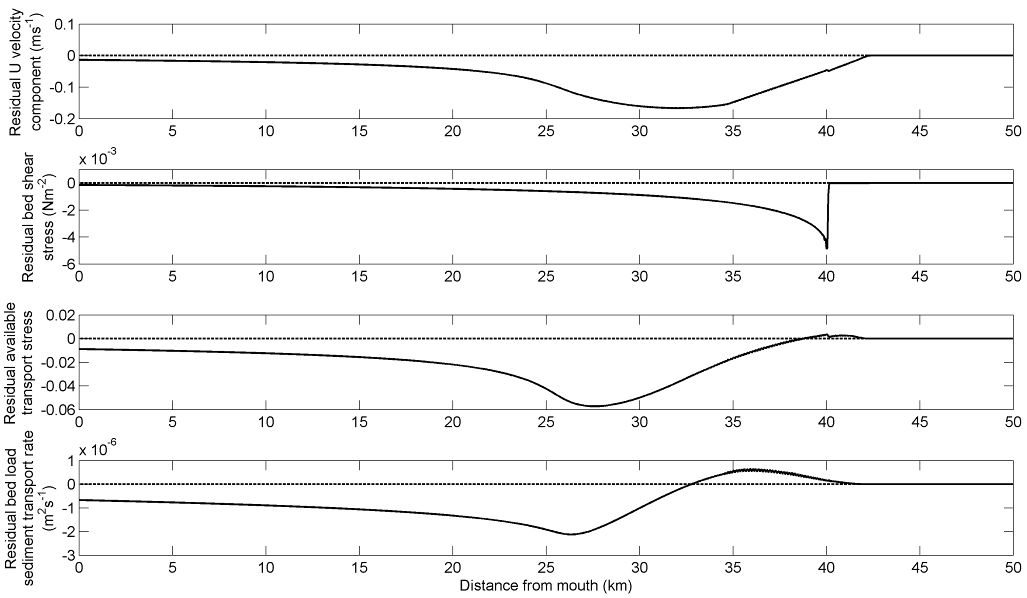

Figure 4.5 – Profiles of the across-basin averaged tidal residual components of (from top to bottom) the along-basin (U) velocity component, bed shear stress, available transport stress $\theta' - \theta_{cr}$ and along-basin component of the bed load sediment transport rate. Positive values are in the direction of the flood tide, negative values are in the ebb direction.

the positive shift in $\theta' - \theta_{cr}$. This is due to the fact that the residual velocity and stress does not take into account the threshold of motion—once it is taken into consideration the flow becomes too weak to transport sediment for much of the tidal cycle, showing the flood tidal pulse to become increasingly significant. The final result is the residual, along-basin bed load sediment transport rate. As this is affected by both the threshold of motion and a non-linear dependence on U and h the transport flux is seen to change from ebb to flood dominance at around 32.5km from the basin mouth. It must be noted that this is the bed-load transport of sediment—suspended sediments are more greatly affected by tidal currents and so may behave differently in respect of flood or ebb dominance.

The residual transport of sediment, although small, is significant for morphological development. The nature of the tidal environment is to transport great quantities of sediment in both in- and out-of-basin directions. The relationship between different hydrodynamic variables and basin geometry, however, creates a residual change. The phrase '*two steps forward, one step back*' is a good analogy—sediment is moved finite distances in a morphological model and the residual movement results in a change in bed morphology. Morphology is a direct consequence of the pattern of residual sediment transport, however it is also true that the residual sediment transport pattern is a consequence of the underlying morphology (Dronkers 1986, Prandle, 2006).

4.3.2 First stage of morphological evolution

Figure 4.6 shows the morphological evolution from a flat bed to 20 years of morphological time. From the initially flat bed a 'hatched' pattern begins to form on the bed which between 15 and 20 years of morphological time grows to a very regular, quasi-sinusoidal bed perturbation with alternate humps and depressions orientated to appear so as to resemble a chess board or 'brick pattern'. This pattern is significant as it arose in every morphological simulation initialised with a flat bed. This morphological pattern is an example of self-organisation, where a system spontaneously takes on a more complicated form *without the influence of external organisational forces.* This is important as the imposition of an external forcing event onto the simulation (e.g. a wave/storm event, river flood etc.) could have been the cause of the pattern formation. However in this case the only input of energy into the model is from the M_2 tidal wave which has a constant amplitude and period (and therefore input of energy) throughout the entire simulation.

It was stated by Hibma et al. (2003) that in order for a morphological model (in that case the 2DH implementation of `DELFT 3D`) to display the processes of morphological self-organisation the initially flat bed must be 'roughened' with some form of infinitesimal perturbation. With the present schematised tidal channel as an example, this is due to the fact that without even an infinitesimal change in across-basin initial morphology there can be no lateral changes in the flow (created from flow veering around changes in depth). These lateral differences in velocity then lead to non-uniform, cross-channel sediment transport rates and subsequent bed level change. `DELFT 3D` is a finite difference model and therefore has a rectangular placement of grid nodes. In the current context of a rectangular model domain with a flat (or along-channel sloping) bed this has the effect of producing a numerically flat across-channel bed. However in the `TELEMAC 2D` finite element environment the placement of nodes is non-uniform. It was found in initial tests that this unstructured placement of grid nodes, combined with the interpolation procedure used in the process of bathymetry mapping and rounding errors of floating point numbers (a consequence of numerical computing) creates infinitesimal, numerical differences in across-channel initial morphology. There is therefore no need to artificially 'roughen' the bed in order to instigate a self-organising morphological evolution.

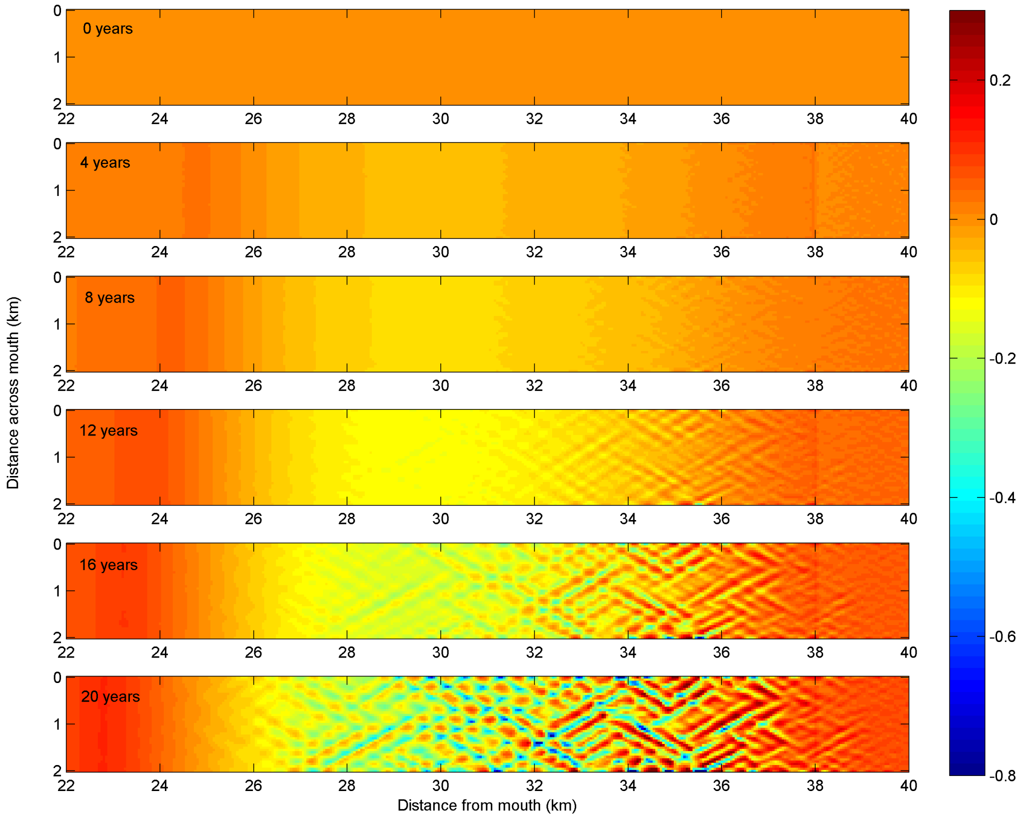

Figure 4.6 – Bed evolution in meters (with the initial bathymetric slope removed) from 0 to 20 years morphological time. The 'brick pattern' is seen to evolve from 12 to 20 years.

Figure 4.7 shows profiles of bed evolution at 4 year intervals over 20 years of morphological time across a centre-line through the model domain (y=1km). The first 12 years (dotted lines) show no formation of bed instabilities but a gradual propagation of a sedimentary 'bed wave', anchored at the head of the basin. This is the evolution of the convex-downward, longitudinal bed profile which is prevalent in tidally-dominated estuaries (Friedrichs & Aubrey, 1996)—a consequence of the residual along-basin sediment transport field which is seen in figure 4.5. There is also a concave-upward evolution in the longitudinal bed profile consistent with the point of change between ebb- and flood-dominated sediment transport (bottom panel in Figure 4.5) that characterises the head of the so-called sedimentary bed wave. Between 16 and 20 years of morphological time large and regular bed forms begin to evolve rapidly—the spontaneous self-organisation of the so called brick pattern. Once complicated plan-form channel-bank patterns emerge the residual transport of sediment becomes more complex. As the tide is constrained in the channels during the ebb tide, local velocities are increased at the same time as an increase in ebb duration caused by tidal asymmetry. This has the effect of creating a plan-form pattern of residual sediment transport, with ebb-dominance in the main tidal channels and flood-dominance over the tidal flats. Figure 4.8 shows an example of this complicated residual sediment transport field, calculated over the 20th tidal cycle (i.e. the 20th morphological year). The vectors in Figure 4.8 display this pattern of flood- and ebb-dominance, especially towards the head of the basin (around 33km from the mouth) where there is a marked difference in residual vector direction between the channels (blue areas) and shoals (red areas). At this

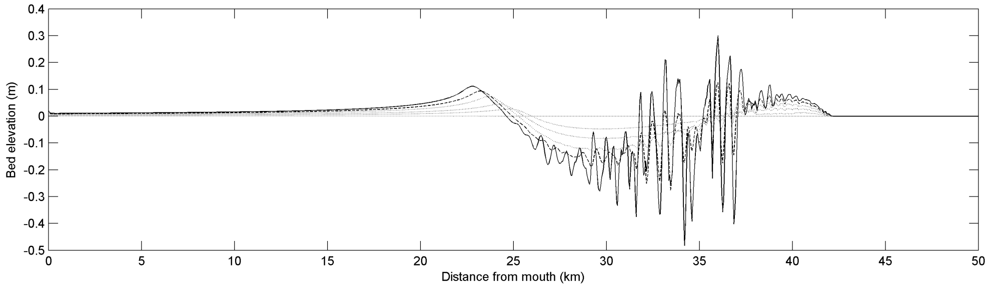

Figure 4.7 – Profiles of bed elevation across the centre-line of the domain (y=1km) at intervals of 0, 4, 8, 12, (dotted lines) 16 (dashed line) and 20 years (solid line) morphological time.

point in the model's morphological evolution the initial, highly regular and ordered self-organised brick pattern has begun to be modified by the tidal currents. The erosional pits are orientated in such a way as to channel water on the ebb tide along diagonal routes. As the depositional humps become 'dry' towards low water, the escaping ebb tide is constrained to flow from pit to pit. This constraint of the tidal flow not only increases the local flow speed but also creates a path which will be subsequently repeated on the following tide. This is critical, as it is this repeated ebb-dominated, constrained tidal flow that begins to 'carve out' the tidal channel network from the connected pits of the initial brick pattern. This is evident in figure 4.8 towards the head of the basin (right of the figure) where the residual bed load sediment transport rate vectors are beginning to follow channel-like paths between the brick pattern pits and humps.

However the bed is not only modified by erosion; depositional processes are also evident in figure 4.8. It follows from the sediment continuity equation (equation 3.5) that divergences in the sediment transport field are responsible for erosion, whereas convergence creates deposition. Both divergence and convergence can be seen in the residual transport field, with convergence occurring above the brick pattern humps and divergence over the pits, with small circulatory patterns occurring in between. This shows that the morphological pattern, although being modified into a channel system by the constrained ebb flow, is also producing a positive feedback in the flow field which is resulting in a sediment transport pattern that serves to cause the pattern to grow. This self-amplification is indicative of self-organisation—if the morphological pattern is to spontaneously grow from a flat bed it must cause a positive feedback in the hydrodynamics or it could not exist without external forcing.

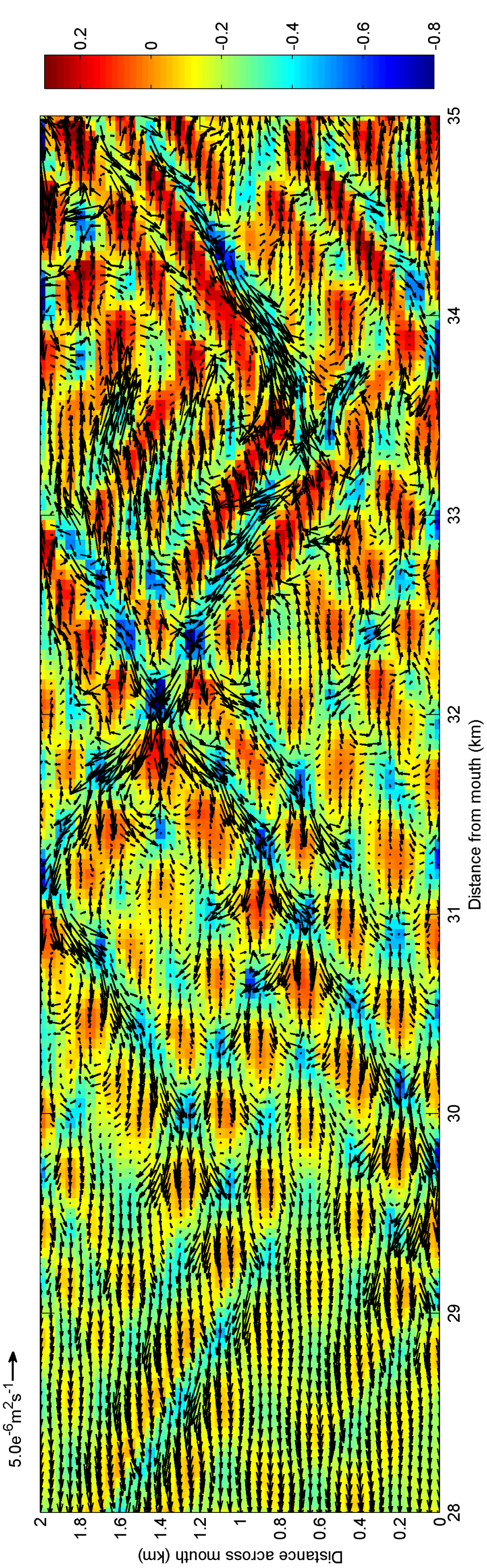

Figure 4.8 – A section of the model bathymetry (in meters with the initial bathymetric slope removed) at 20 years of morphological time overlain with vectors of the tidal residual bed load sediment transport rate.

4.3.3 Second stage of morphological evolution

As soon as the tidal flow becomes consistently constricted within channels during each subsequent tide the second stage of morphological development begins. Here the conditions required to create the initial, self-organised morphology are overcome by the much larger velocities and sediment transport rates that are created by flow within the evolving tidal channels. The channels are now the dominant morphological element in the system and all subsequent morphological structures evolve from their present form. Figures 4.9–4.12 show the evolution of the channel-bank system at 4 year intervals over the remaining 80 year period. In figure 4.9 the first stages of this process are evident. As the pits of the initial morphological pattern are connected and formed into channels, multiple meandering tidal channels begin to form in the bed. These channels then begin to compete with each other for space as they grow laterally. There is a limited amount of lateral space (only

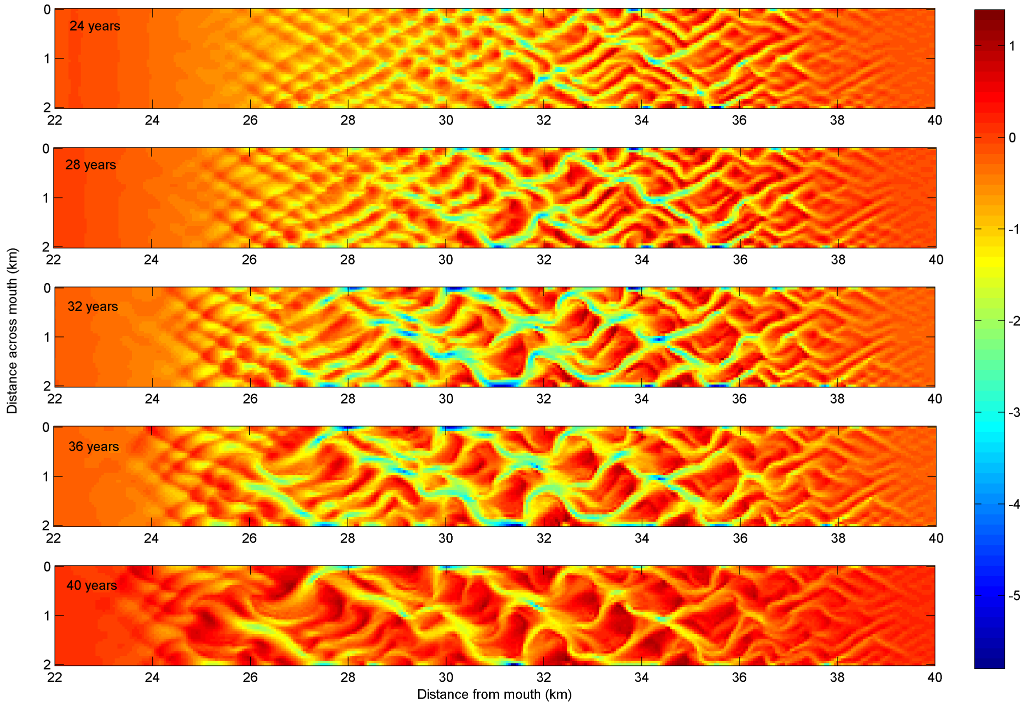

Figure 4.9 – Bed elevations in meters (with the initial bathymetric slope removed) from 20 to 40 years of morphological time.

2km) in this particular basin and the channel bends begin to interact with the domain boundary, which has a boundary condition of zero flux and no slip. This may be likened to an infinitely tall and deep wall that absorbs all energy incident onto it. This has the effect of anchoring the channel bend apexes onto the domain boundary—as the meander has no room to evolve into laterally and the boundary condition prevents flux through it the bend apex forms a deep pit (blue areas at the edges of the domain in figures 4.9–4.12). These pits then become self-sustaining, being seen to remain in similar positions (i.e. not migrating) throughout the 100 year simulation. The channel-shoal network continually grows longitudinally towards the mouth of the basin, reaching approximately 15km from the mouth at 100 years morphological time—approximately 10km from the extent of the initial brick pattern. There is a much slower spread of the network towards the head of the basin, but this is due to the very low velocities and flow depths in this region of the model as it marks the limit of tidal influence.

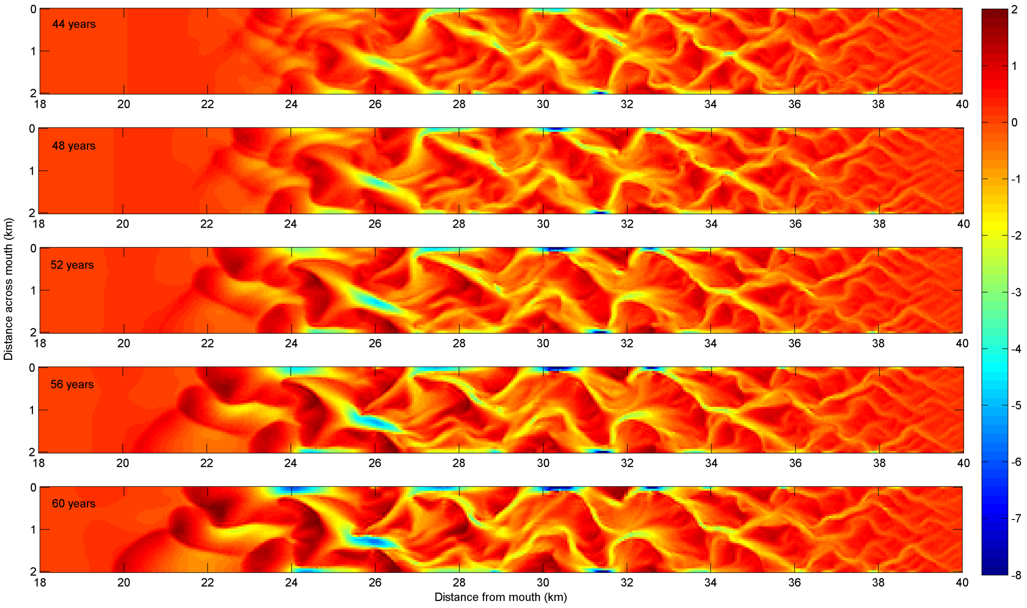

Figure 4.10 – Bed elevations in m relative to mean sea level with the initial bathymetric slope removed from 40 to 60 years morphological time.

There are large differences in maximum flow velocity magnitude across the basin over the first morphological year and the 100th (figure 4.13), both

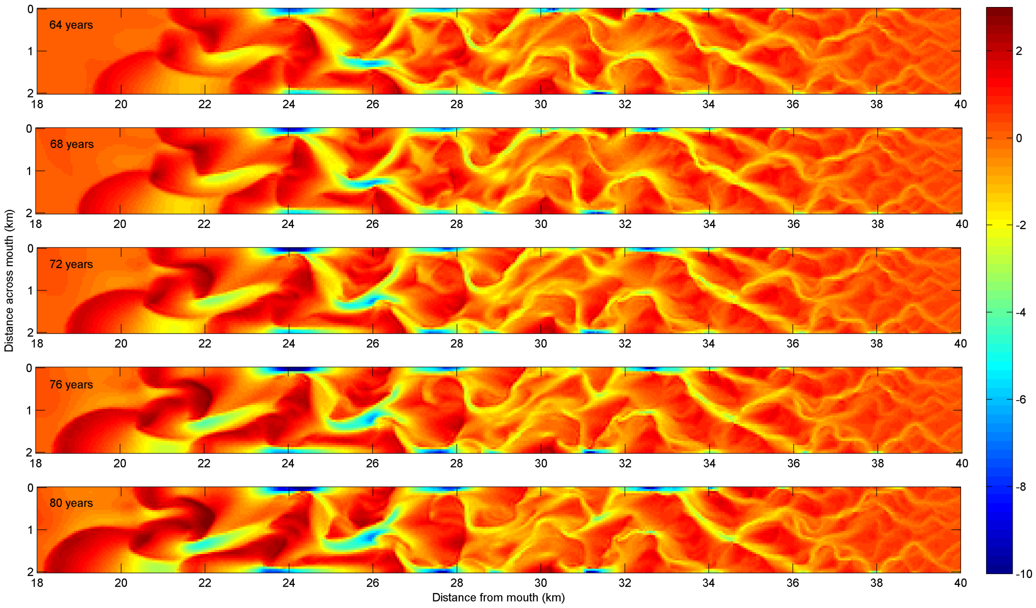

Figure 4.11 – Bed elevations in meters (with the initial bathymetric slope removed) from 60 to 80 years of morphological time.

in the value of maximum velocity and its distribution due to the difference in bathymetry. The maximum magnitude of tidal velocity increased from $0.96ms^{-1}$ in year 1 to $1.78ms^{-1}$ in year 100. The high flow velocities at 100 years are constrained mostly to the deep pits which come into contact with the model boundary. These increased velocities are also balanced, in part, by reduced flow speeds on the banks between the main tidal channels where flow depth is shallower and where tidal inundation is for shorter periods than within the channels. The erosion of the tidal channel network allows the tidal range to increase locally as the tidal wave is able to penetrate further up-estuary (figure 4.14). Although the general trend of tidal amplification and the subsequent reduction in tidal range with shoaling depth remains similar at the end of the simulation as it was at the start, the maximum across-basin tidal range is higher further up-estuary in the tidal channel network due to the deeper channels which allow the tide to penetrate further up-basin.

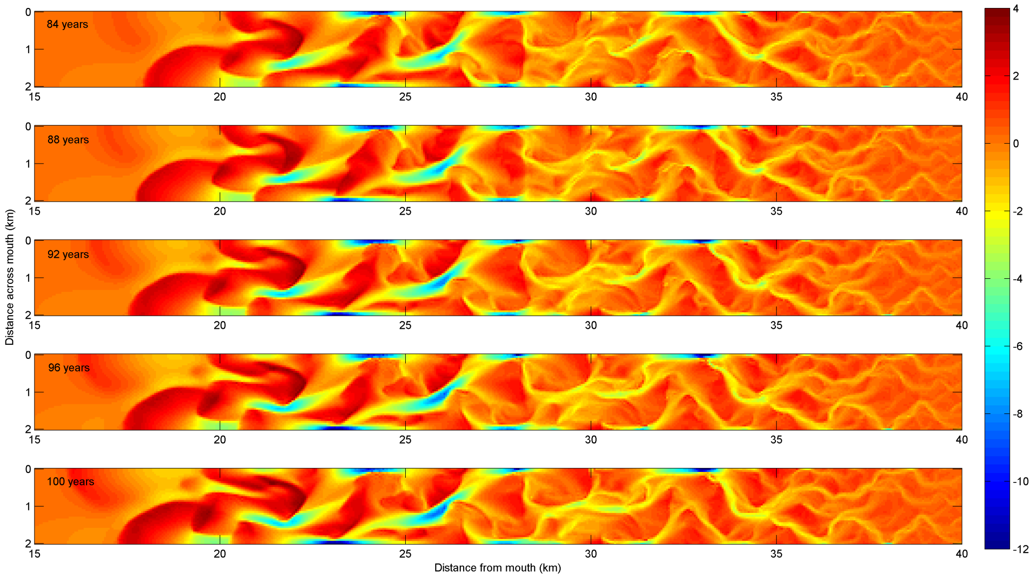

Figure 4.12 – Bed elevations in meters (with the initial bathymetric slope removed) from 80 to 100 years of morphological time.

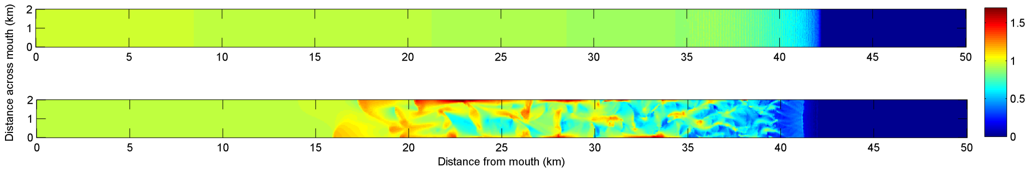

Figure 4.13 – Maximum velocity over the 1st and 100th morphological years (top and bottom panels respectively) in ms^{-1}.

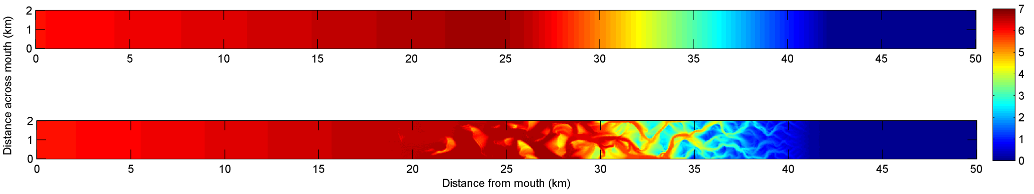

Figure 4.14 – Tidal range over the 1st and 100th morphological years (top and bottom panels respectively) in m.

4.4 Summary

This is the first time that a coupled morphological simulation between `TELEMAC 2D` and `SISYPHE` has been undertaken using the morphological factor approach to bed level updating. This has not been due to a lack of suitability of the `TELEMAC 2D` model package, but rather a predominant use of other 2DH model systems (especially the 2DH implementation of `DELFT 3D`) in the field of morphodynamic research. It is concluded that `TELEMAC 2D` and `SISYPHE` are suitable for the use of the morphological factor method but some thought must be lent to an appropriate choice of MF coefficient.

It is interesting that a heavily simplified model in a rectangular, schematised basin geometry can produce a complicated tidal channel-bank network without any associated external forcing. Although previous studies have explored the evolution of such morphology from a flat bed in detail there has been little attention given to the initial years of morphological evolution. The initial pattern is not channel-like in nature but a regular, quasi-sinusoidal pattern of humps and pits which spontaneously evolves from a flat bed. Such self-organisation of morphology has been investigated in the past, but this has always concentrated on the self organisation of the channel network as a whole. In the model simulation presented here it appears that the initial pattern which is ultimately responsible for the entire tidal channel network is produced by a different process. The brick pattern is significant as it leads to more complicated morphological development, yet it is subtle in scale and form which suggests it may be explained by an analytical solution. Whether it is a true physical phenomenon or a product of the model environment (the use of a finite element grid, for example) should be a subject for future investigation.

The model presented here was a simplified, schematic case of a tidal sandy basin. It has been shown that suspended sediment transport using an advection-diffusion scheme is not compatible with the MF method, but a total-load sand transport formula (some of which are already programmed into `SISYPHE`) could provide some insight into the effect of the contribution of the suspended load on the rate of development of the tidal channel network. It can be assumed that the use of a total load sand transport formula will increase the rate of sediment transport (and therefore morphological evolution)—possibly to the point where a reduction in the choice of MF coefficient is necessary to preserve stability.

The effect of waves using the `TOMAWAC` wave module has not been assessed in this study as it is believed that without full internal coupling with `TELEMAC 2D` and `SISYPHE` the module is not compatible with the MF method due to the current need to interrupt the tidal cycle to simulate the wave field. The effect of waves will be important in models of natural, 'real-world' tidal basins, so this is an important issue which needs to be addressed in the future.

The simulation was ended at 100 morphological years, however it is clear from figures 4.9–4.12 that the tidal channel network is propagating towards the basin mouth. At the current rate of propagation (approximately 10km in 100 years) it is estimated that the network will fill the entire area of the domain influenced by the tide in 250–300 morphological years. The rate of propagation may slow in deeper water towards the mouth however, as the bed shear stress is generally lower which will slow the rate of sediment transport and therefore the rate of morphological evolution.

A change in MF coefficient is expected to directly affect the rate of morphological evolution with respect to the hydrodynamic time-scale. In section 3.6.3 a model was presented where very high MF coefficients (up to 10,000) resulted in a relative slowing of morphological evolution. Such a large MF coefficient is not recommended for most simulations, and as moderate coefficients did not have a significant affect on bed evolution it is not expected that a change in the MF number will produce a significantly different morphological pattern.

The tidal channel network present in the simulation results is a product of a simplified implementation of both the hydrodynamics and sedimentological processes. Although the form of the network appears realistic, the behaviour of the system lacks certain features that are present in nature. The 2DH implementation of the hydrodynamics ignores three-dimensional circulation that is important for the formation of river meanders where helical flows cause erosion at the outer boundary of the meander and deposition at the apex. It is believed that a full 3D implementation of the hydrodynamics would therefore provide a more complete description of the physical processes important for meander development.

Another important consideration is the role of river flows in channel-bank networks in real-world tidal basins. Estuaries, by their very definition, are the connection between rivers and the coast and as such river flows play an important role in estuarine morphodynamics. After periods of heavy rainfall in the river's catchment area a flood occurs, manifest by an increased river flow rate and enhanced import of terrestrially-derived sediments. During flood events major morphological changes can occur, especially in the main tidal channel. Avulsion events—the abandonment of one section of channel for another by the flow—are common during river floods, significantly altering the large-scale morphology of the estuary in a relatively short period of time. However in the presented model only tidal flow is simulated with a single harmonic constituent as the MF method is not deemed suitable for events modelling.

Chapter 5

Modelling bed roughness feedback in `TELEMAC 2D`

5.1 Introduction

Beds of non-cohesive sediment, such as in many coastal environments, are rarely ever flat. Bed forms—ripples and dunes—are generated by an interaction between the free surface flow and the erodible bed. The frictional force generated between the flow and the bed is heavily affected by the presence and form of these sedimentary structures. Form drag, the pattern of pressure around the bed form due to flow separation over the crest, generates a frictional force which is often the dominant resistive force between bed and flow in coastal tidal environments (Soulsby, 1997).

Bed roughness enters the flow computation as the roughness length z_0 of the logarithmic velocity profile. As such an increase in the hydraulic roughness of the bed results in a decrease in the depth-averaged flow velocity $\bar{U}$. However, roughness also has a direct impact on the bed shear stress τ_0, both through the drag coefficient C_D and its previous effect on $\bar{U}$ which is subsequently amplified as $\tau_0 = 1/2\rho C_D \bar{U}^2$.

The effect of ripple roughness on sediment transport has been widely reported. However the roughness due to dunes—which often make up much of the bed in deeper channels of sandy estuaries—on sediment transport rates in coupled morphological models is poorly understood.

Currently under development is an adaptation to `TELEMAC 2D` and `SISYPHE` which allows bed roughness calculated in `SISYPHE` to be fed back into `TELEMAC 2D` to affect the following flow computation. At the time of writing the current release of `TELEMAC 2D (v6.0)` does not contain this feature as a standard, built-in option.

In most part the lack of research on the influence of dunes on coupled morphological models is due to a lack of field evidence which requires a greater spatial range (due to the size of dunes) than that for ripples. A recent field campaign in the Dyfi estuary, however, provided an extensive, fine-scale map of the seabed using swathe sonar. In this chapter a coupled morphological model of the Dyfi is presented which contains a mechanism to feed back bed roughness to `TELEMAC 2D`. The model is run to simulate a period of 21 days in July 2007 which coincided with the swathe sonar bathymetric survey with the attempt to reproduce the bed roughness derived from these measurements. The simulation hydrodynamics are validated by data from three tide gauges obtained during the same field campaign. The effect of coupling roughness between `TELEMAC 2D` and `SISYPHE` on the subsequent sediment transport rate for a simplified tidal case in the Dyfi is also explored.

5.2 Predicting roughness due to bed forms

To simulate a time-dependent bed roughness the predictive formulae of Van Rijn (2007) were used, coded into the `RIDE` subroutine of `SISYPHE`. Here the roughness length is predicted for ripples ($k_{s,r}$), megaripples ($k_{s,m}$) and dunes ($k_{s,d}$) separately and then combined to form a total bed roughness k_s. The formulae are dependent on the mobility parameter ψ where

$$\psi = \frac{\bar{U}}{gsD_{50}} \tag{5.1}$$

and a granular coefficient f_s to reduce k_s at large grain sizes, where $f_s = 0.25\left(D_{gravel}/D_{50}\right)^{1.5}$ for $D_{50} > 0.25D_{gravel}$ and $f_s = 1$ for $D_{50} \leq 0.25D_{gravel}$ (where $D_{gravel} = 2mm$). The contribution of each bed form type to the total roughness is based on their height, and as such, the predictive formulae represent curves of bed roughness with respect to ψ, representing the formation and destruction of bed form height with increasing bed stress.

Ripples

The bed roughness length due to ripples $k_{s,r}$ is assumed to be roughly equal to the ripple height η (Van Rijn & Havinga 1995). Ripples are assumed to be fully formed in the low-flow regime ($\psi \leq 50$) and 'washed-out' (their crests rounded-off and thus steepness reduced) in the high-flow regime ($\psi > 250$) with the only contribution to k_s coming from moving grains in the sheet flow layer. In the transitional regime ($50 < \psi \leq 250$) a linear decay curve is assumed so that

$$\begin{aligned} k_{s,r} &= 150 f_s D_{50} & \psi \leq 50 \\ k_{s,r} &= (182.5 - 0.652\psi)\, f_s D_{50} & 50 < \psi \leq 250 \\ k_{s,r} &= 20 f_s D_{50} & \psi > 250 \\ k_{s,r} &= 20 D_{silt} & D_{50} < D_{silt} \end{aligned} \tag{5.2}$$

The conditions in equation 5.2 can be combined into a continuous curve which is the form used in `RIDE` so that

$$k_{s,r} = f_s D_{50} \left\{85 - 65 \tanh\left[0.015\,(\psi - 150)\right]\right\} \tag{5.3}$$

The corresponding curve from equation 5.3 can be seen as the solid black line in figure 5.1.

Megaripples

Megaripples are distinct from ripples in that they are related to the flow depth h, with a bed roughness length equal to approximately 0.5η (Van Rijn, 1993). However the contribution of megaripples (and later dunes) to the bed roughness $k_{s,m}$ is not calculated based on bed form dimensions but estimated directly from empirical experiments. $k_{s,m}$ is assumed to be related to ψ and h so that

$$\begin{array}{ll} k_{s,m} = 0.0002 f_s \psi h & \psi \leq 50 \\ k_{s,m} = (0.011 - 0.00002\psi_s h & 50 < \psi \leq 550 \\ k_{s,m} = 0.02 & \psi > 550 \text{ and } D_{50} \geq 1.5 D_{sand} \end{array} \qquad (5.4)$$

The conditions in equation 5.4 can be combined into a continuous curve which is the form used in `RIDE` so that

$$k_{s,m} = 0.00002 f_s h \left[1 - \exp\left(-0.05\psi\right)\right] \left(550 - \psi\right) \qquad (5.5)$$

The corresponding curve from equation 5.5 can be seen as the dashed black line in figure 5.1.

Dunes

Dunes can provide the greatest contribution to the total hydraulic roughness of the bed. With dimensions that are strongly linked to the flow depth, dunes have a significant influence on flow speeds.

$$\begin{array}{ll} k_{s,d} = 0.0004 f_s \psi h & \psi \leq 100 \\ k_{s,d} = \left(0.048 - 0.00008\psi\right) f_s h & 100 < \psi \leq 600 \\ k_{s,d} = 0 & \psi > 600 \end{array} \qquad (5.6)$$

The conditions in equation 5.6 can be combined into a continuous curve which is the form used in `RIDE` so that

$$k_{s,d} = 0.00008 f_s h \left[1 - \exp\left(-0.02\psi\right)\right] \left(600 - \psi\right) \qquad (5.7)$$

The corresponding curve from equation 5.7 can be seen as the dotted black line in figure 5.1.

Total bed roughness

The depth-averaged flow, as calculated by `TELEMAC 2D`, ‘feels’ the total hydraulic roughness of the bed—that is to say the combination of all roughness elements. Following Van Rijn's method the total bed roughness k_s is a quadratic summation of the three bed roughness elements so that

$$k_s = \sqrt{{k_{s,r}}^2 + {k_{s,m}}^2 + {k_{s,d}}^2} \tag{5.8}$$

As such, the presence and size of dune roughness will dominate k_s, providing a much greater contribution. This is physically sound, as the form drag, flow separation and associated turbulence of dunes will provide a greater frictional force to the total flow than those produced by ripples and megaripples.

`TELEMAC 2D` uses the total bed roughness k_s to calculate flow velocities (through the drag coefficient C_D). Although megaripples and dunes will have some effect on sediment transport there is, at the time of writing, no parameterisation in `SISYPHE` to include their roughness contributions (through k_s) in the calculation of sediment transport rates. Depending on the form of sediment transport formula chosen, `SISYPHE` either requires only the granular roughness, small scale ripple roughness (form drag on ripples) or a combination of both. In the model presented in this Chapter the chosen sediment transport formula is that of Bijker (1968), which uses the small scale ripple roughness $k_{s,r}$.

The above procedure is programmed into the `SISYPHE` subroutine `RIDE` where the value of k_s and $k_{s,r}$ at every node are stored to an external file. Before the calculation procedure there is a check on θ' and no roughness element is updated in the external file unless $\theta' \geq \theta_{cr}$. The external file is then used by `TELEMAC 2D` in the next computation time step through the subroutine `CHESTR` which sets k_s at every node to the value in the file. Only the $k_{s,r}$ ripple component is used by SISYPHE for sediment transport computation (figure 5.2).

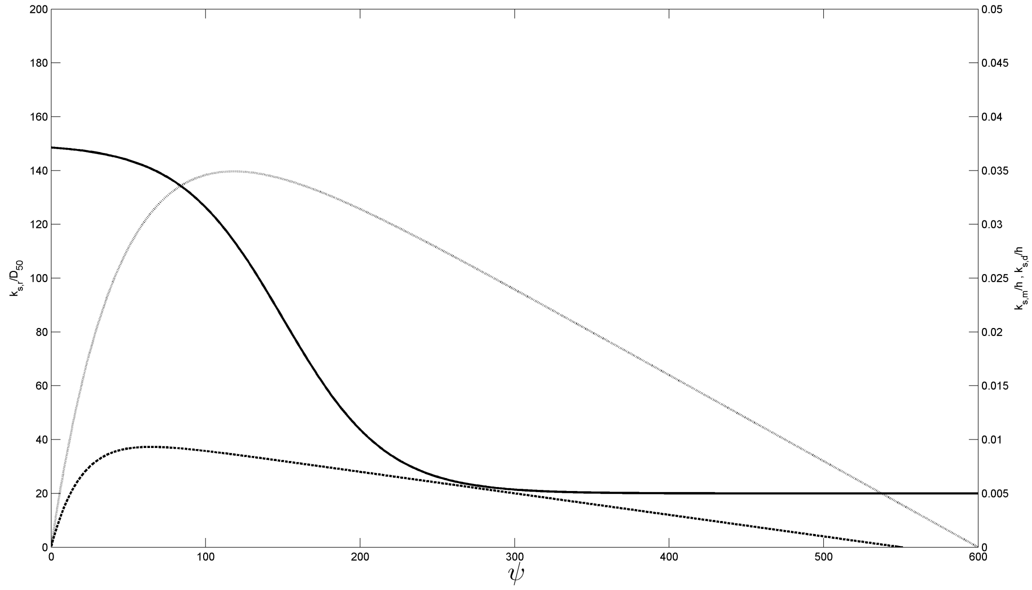

Figure 5.1 – The variation of $k_{s,r}/D_{50}$ (solid line, left axis), $k_{s,m}/h$ (dashed line, right axis) and $k_{s,d}/h$ (dotted line, right axis) with the mobility parameter ψ from equations 5.3,5.5 and 5.7 respectively, as coded into `SISYPHE`. The total bed roughness k_s is a quadratic summation of all three curves.

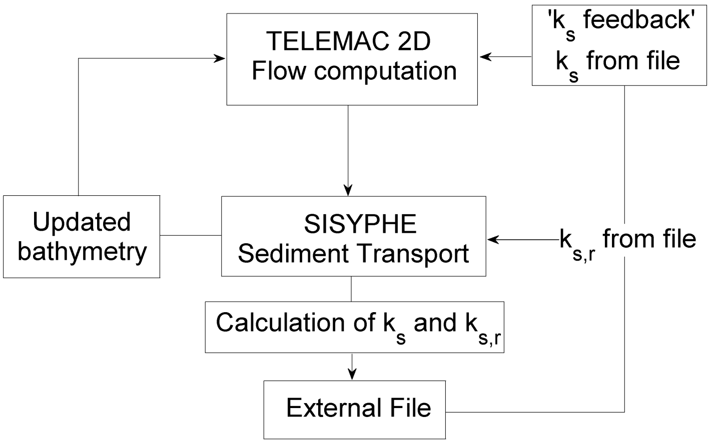

Figure 5.2 – Schematic representation of the k_s feedback procedure in `TELEMAC 2D` and SISYPHE.

5.3 Extracting bed-form dimensions from side-scan sonar data

A swathe sonar bathymetric survey of the Dyfi Estuary was undertaken in July 2007 as part of a field monitoring program funded by the Centre for

Catchment to Coast Research (CCCR). The instrument (on loan from R. Bates at the University of St. Andrews) was a SEA Ltd 'SWATHplus-H' system with 468kHz transducers pole mounted over the side of a light vessel. Bed elevations were calculated from the depth beneath the instrument and the elevation of the vessel on the free surface using a Leica 1200 RTKGPS and tidal data from two gauges to make corrections. The raw data were processed by R. Bates to 1m resolution in the horizontal and 10cm in the vertical, producing a map of bed elevations (figure 5.3) which could be used to extract the dimensions of dune-like bed forms with wavelengths of the order of tens of meters. Due to the need for a minimum depth of water for the side scan instrument to operate correctly, measurements were taken at high-water and could only be taken a short distance up the main tidal channel. Extensive measurements were taken around the scour pit and estuary mouth however, where relatively deep water made wide-area bed scans possible (figure 5.4).

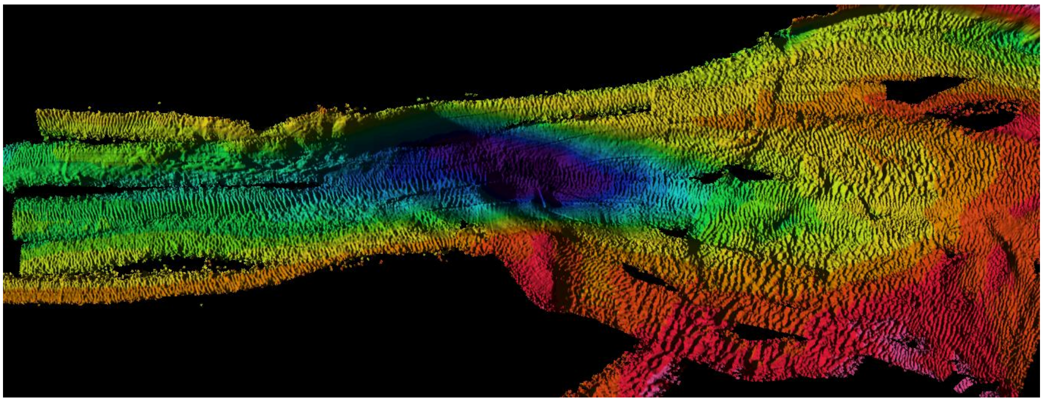

Figure 5.3 – Image of the Dyfi seabed from Side Scan Sonar, highlighting the 'texture' of the bed with artificial lighting which shows the extensive presence of large bed forms.

5.3.1 Turning points algorithm

To extract individual bed forms from the sonar data set 103 profiles were taken (an example of which can be seen in figure 5.5), each selected to lie as close as possible to perpendicular across bed form crests. Profiles were also chosen to only intersect areas containing bed forms (much of the channel

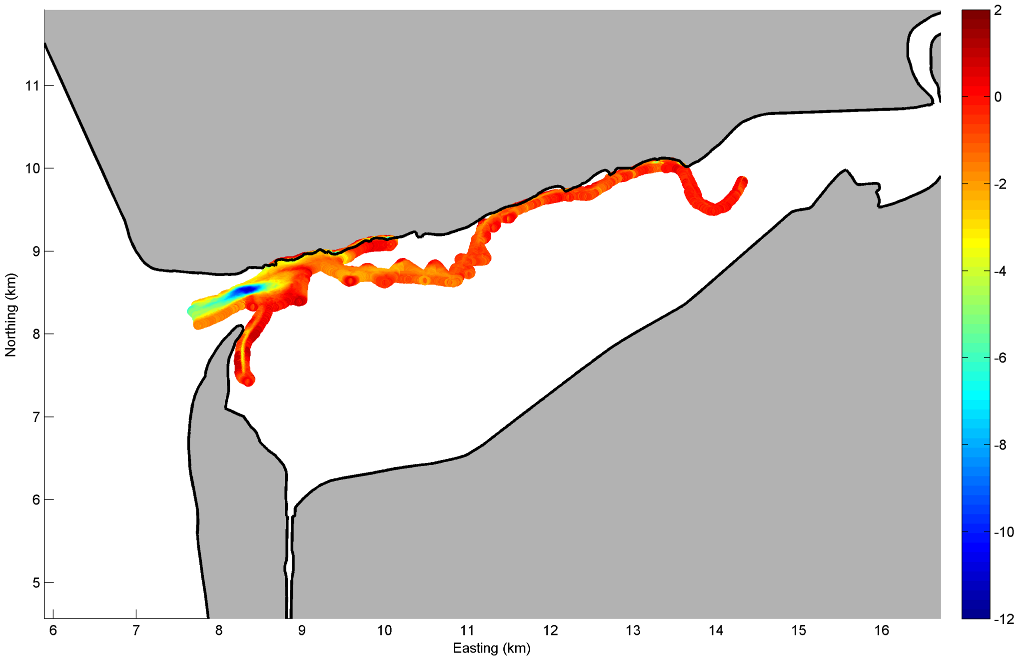

Figure 5.4 – Extent of the Swathe sonar bathymetric survey data relative to the Dyfi model grid boundary. Sonar derived bed elevations in m below ODN.

section of the sonar data were devoid of bed forms). As such the profiles varied considerably in length, from a single bed form to hundreds of meters. The profiles were then run through a turning points algorithm to identify the coordinates of bed form crests and troughs. Working along the profile $(Z(i=1), Z(i=2), \cdots, Z(n))$ the forward and backward bed gradients ($\overset{\rightarrow}{\Delta}Z$ and $\overset{\leftarrow}{\Delta}Z$) were calculated as

$$\overset{\rightarrow}{\Delta}Z= \frac{Z(i+1)-Z(i)}{x(i+1)-x(i)} \quad \overset{\leftarrow}{\Delta}Z= \frac{Z(i-1)-Z(i)}{x(i-1)-x(i)} \tag{5.9}$$

so that comparison of the two gradients would yield whether the algorithm had reached a crest or trough in the profile. Crests correspond to the situation $\overset{\rightarrow}{\Delta}Z< 0$ and $\overset{\leftarrow}{\Delta}Z> 0$ while troughs correspond to $\overset{\rightarrow}{\Delta}Z> 0$ and $\overset{\leftarrow}{\Delta}Z< 0$ (figure 5.6)

To calculate the bed form length λ and height η, individual bed forms were identified as two troughs with an intermediate crest. With the assumption that the bed forms were long-crested and two-dimensional in plan form, λ can

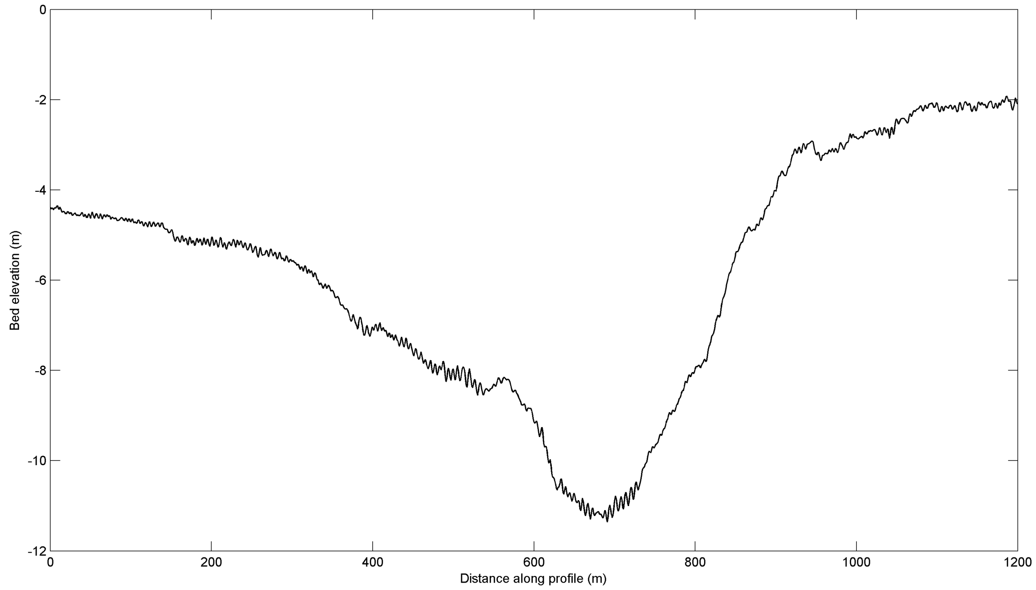

Figure 5.5 – Example of a bed elevation profile extracted from the sonar data. The profiles are chosen to lie perpendicular to bed form crests—this particular profile runs through the scour pit (left of profile corresponds to the estuary mouth).

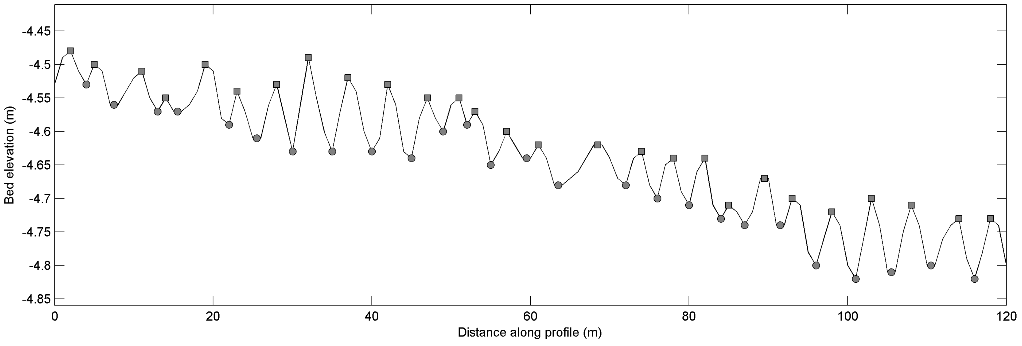

Figure 5.6 – Example section of the profile in figure 5.5 after application of the turning points algorithm to locate the position of bed form crests (squares) and troughs (circles).

be defined as the distance between two successive trough points. However many of the bed forms were found to lie on a mean bed slope and so the true on-ground distance between two trough points would be greater than the distance between their respective x coordinates. Bed form length was therefore taken in all cases as the length of line connecting both trough points in x, z space (figure 5.7). The bed form height η was similarly taken from a line perpendicular to that between two troughs and intersecting the intermediate crest point.

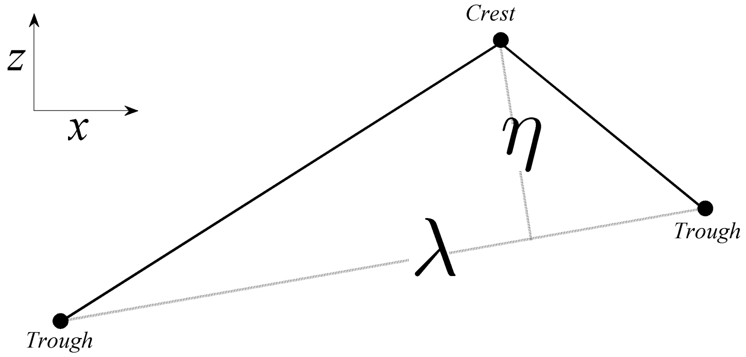

Figure 5.7 – Representation of a bed form on a sloping bed. Bed form length λ is taken from a line drawn between successive troughs and the height η taken as the length of a line perpendicular to this and crossing through the intermediate crest.

Each measurement of length and height was co-located with the 'real-world' x, y coordinate of the corresponding bed form crest, calculated by interpolating from the x, y coordinates of the end-points of each profile. 2730 individual bed forms were measured, covering much of the area around the scour pit as well as an up-stream portion of the main ebb channel (figure 5.8).

5.4 Dyfi model set-up

Using the Dyfi model grid outlined in Chapter 3, a validation case was set up to simulate the tidal conditions for the period 9th–20th July, 2007, to co-incide with the period covered by the swathe sonar survey.

Tidal boundary condition

For the off-shore liquid open boundary a tidally varying free surface elevation was assigned using eight tidal constituents (M2,S2,M4,K1,K2,O1,Q1 and P1),

Figure 5.8 – Locations of measured bed forms extracted from the side scan sonar data set in the Dyfi. Dark grey areas represent the coverage of bed form measurements.

provided by the POLCOMS Irish Sea tidal model (courtesy of S.Neil, University of Bangor). The amplitudes and phases of the eight constituents were linearly interpolated onto the 27 offshore boundary points (Figures 5.9 and 5.10) and programmed into the subroutine `BORD` to calculate the free surface elevation at each offshore boundary node at each time step. Nodal tuning coefficients were applied to the amplitude and phase of each constituent to adjust the predicted tide to the correct start date. This is important as the tidal envelope not only changes significantly during the spring-neap cycle but longer-term changes in the envelope occur due to the addition of further tidal harmonics. The start date was chosen to be 24 hours before the beginning of the period covered by the data.

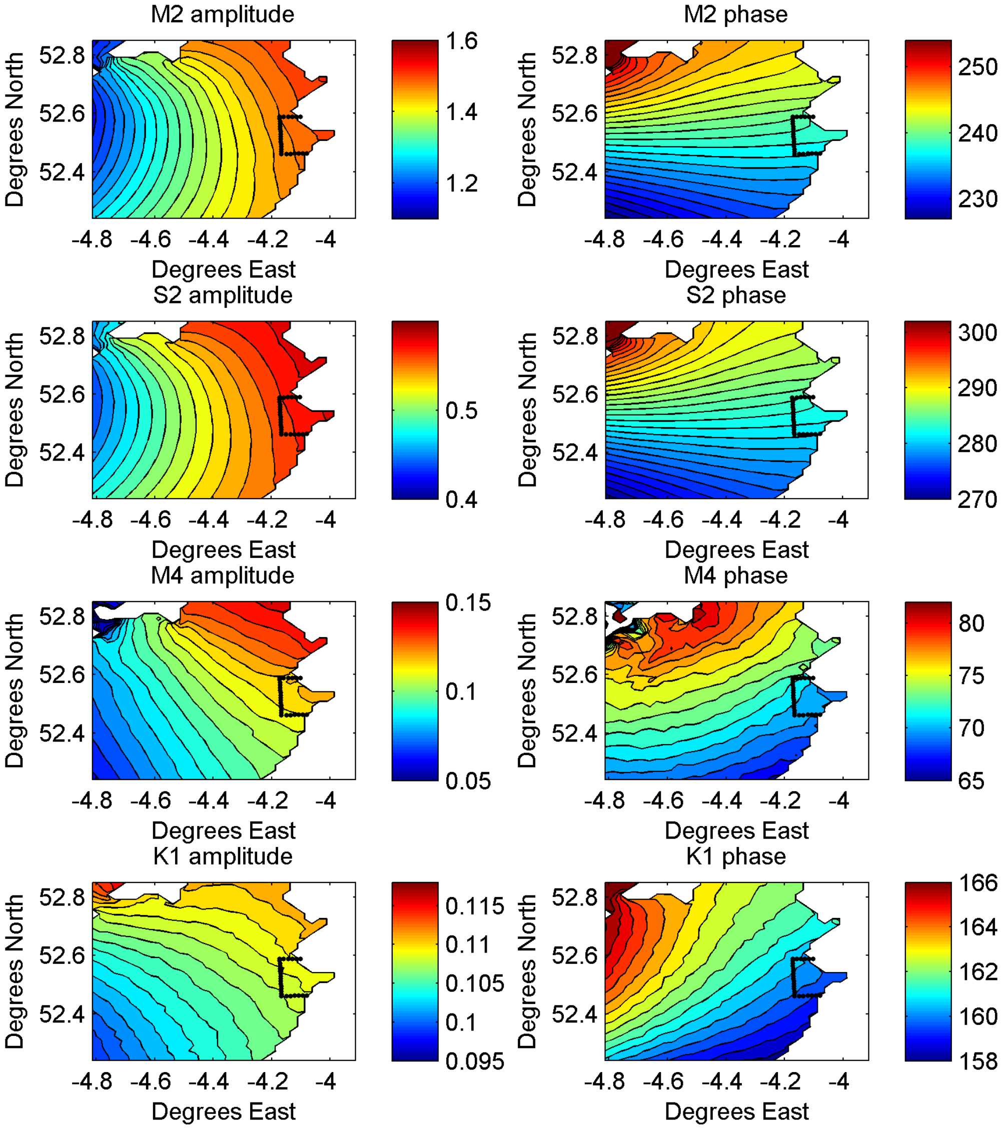

Figure 5.9 – Tidal constituents used to force the liquid boundary taken from POLCOMS (courtesy of NOC, Liverpool). Panels on the left show amplitude (m) and panels on the right the phase (degrees). The black symbols represent the liquid outer boundary of the model onto which each constituent amplitude and phase were interpolated.

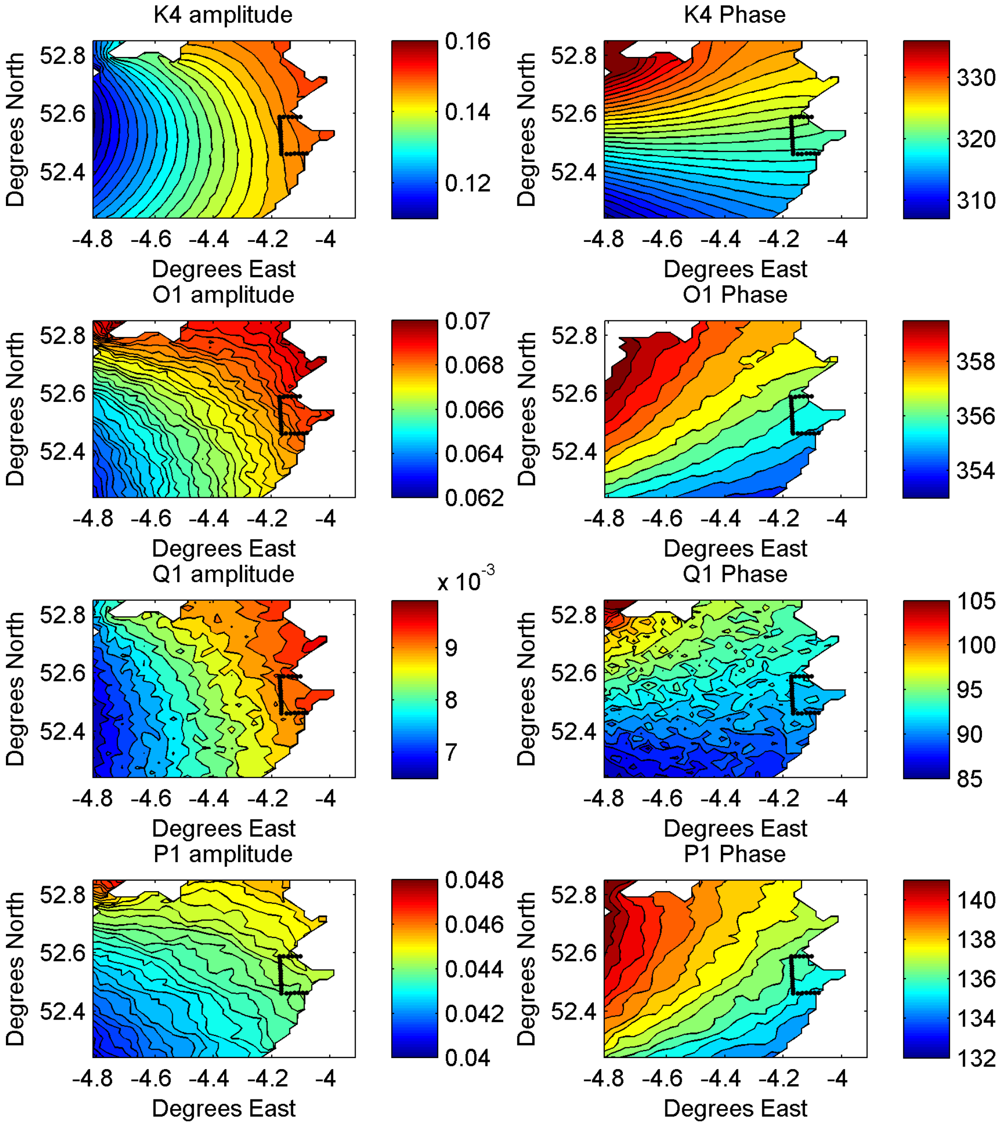

Figure 5.10 – Tidal constituents used to force the liquid boundary taken from POLCOMS (Courtesy of NOC, Liverpool). Panels on the left show amplitude (m) and panels on the right the phase (degrees). The black symbols represent the liquid outer boundary of the model onto which each constituent amplitude and phase were interpolated.

River boundary condition

The Dyfi Estuary has two main river inputs—the Dyfi and the Leri. Both rivers are relatively small in comparison to many UK rivers with yearly average flow rates of approximately $20m^3s^{-1}$ and $1.5m^3s^{-1}$ respectively. At the time the present work was undertaken there was an incompatibility between the liquid boundary assignment code `BORD` and the use of an external, formatted liquid boundary conditions file—essentially a table containing the simulation time, flow rates and/or free surface elevation through which `TELEMAC 2D` interpolates. As the formatted boundary conditions file is the method used for inputing a time-varying flow rate through a number of boundary nodes (i.e. river inputs) and the extensive use of `BORD` for the input of the tidal boundary condition it was decided to use the yearly average river input from the Dyfi and Leri.

5.5 Results

5.5.1 Tidal elevations

Free surface elevations from the three tide gauges in the Dyfi were compared to the corresponding free surface elevations from the simulation (figure 5.11). It can be seen that although both models achieve a relatively good fit with observed tidal elevations (especially at the Aberdyfi gauge site) the degree of asymmetry in the observed tide is not fully reproduced. The models both reproduce a low-water phase which is earlier than the observed tide, while high-water is generally well represented.

There are, however, significant differences between the model and observation period that contribute to the differences between the simulation and observation data seen in figure 5.11. Firstly, the omission of a more accurate, time-dependent Dyfi river boundary condition lead to differences in the free surface elevations, particularly at low water and further up-estuary. The differences in tidal phase between the simulation and observations is most probably due to the difference in bathymetry as the LIDAR survey was conducted in 2004 while the simulation period is in 2007. This most likely is manifest as a difference in the position of the main tidal channel (known to migrate dynamically) that will result in a change in the speed of tidal propagation within the estuary. Improvements to the validation could therefore be made by introducing the river flood and, if possible, by sourcing more recent bathymetric data.

Although there are differences (some significant) between the simulated and observed free surface the model does reproduce the general tidal envelope well. It can therefore be expected that the general magnitude of tidal currents in the observation period are reproduced with sufficient accuracy to make further comparisons with the model data—specifically between the bed forms measured during the Sonar survey and the modelled k_s.

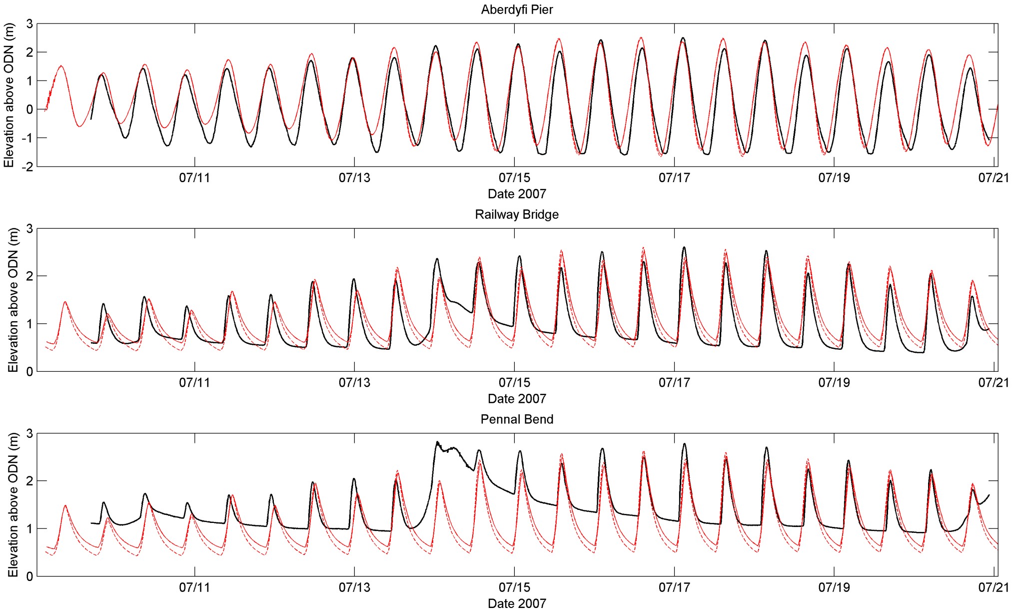

Figure 5.11 – Free surface elevations from tide gauge data (black lines) and simulated tidal elevations with and without k_s feedback implemented (solid and dashed red lines respectively) for three sites in the Dyfi. The increase in the mean free surface level evident in the 'Railway bridge' and 'Pennal bend' tide gauge data sets beginning on the 14th of the month is most likely due to a river flood event which occurred at that time.

5.5.2 Bed form dimensions from sonar survey

Over 130 profiles of 2730 individual bed forms were extracted by the turning points algorithm. Bed forms varied in wavelength λ between 2–30m (2m being the minimum possible wavelength at twice the spatial resolution of the data) with an average of 6.22m and standard deviation of 2.45m and between 0.01–1m in height η with an average of 0.19m and standard deviation of 0.13m (figure 5.13). Bed form steepness η/λ ranged between 1/10 and 1/100 (figure 5.12), indicating that these indeed are shallow, dune-like bed forms (Van Rijn, 1984b).

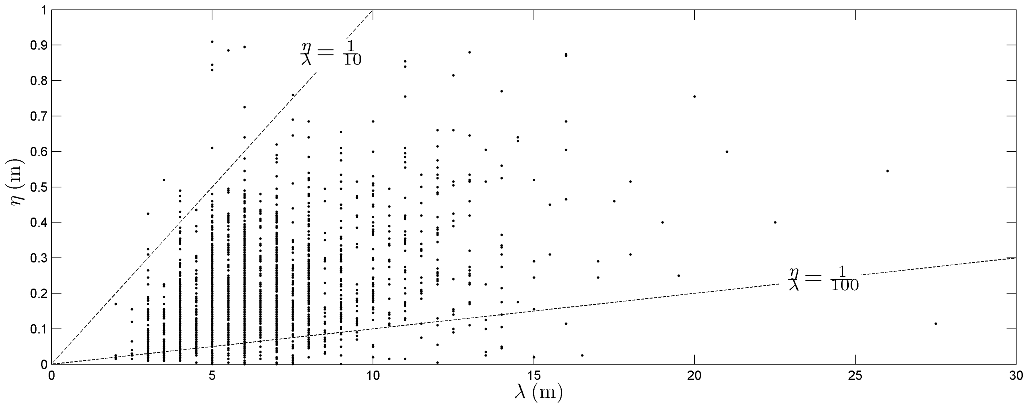

Figure 5.12 – Measured wavelengths λ and heights η of bed forms from the sonar data. The two dotted lines represent bed form steepnesses η/λ of 1/10 and 1/100, between which the majority of the data points lie.

5.5.3 Total bed roughness prediction from `TELEMAC 2D`

The k_s feedback method calculates a new value of k_s (For `TELEMAC 2D`) and $k_{s,r}$ (for `SISYPHE`) at every time-step and at every node that satisfies the condition $\theta' \geq \theta_{cr}$. This equilibrium approach produces a dynamic roughness environment that responds to changes in tidal currents and flow depths, with ripples and dunes evolving and devolving with the local state of ψ. Figure 5.14 shows a time-series of model output parameters over the simulation period from a point located at the centre of the scour-pit. Here depth and flow velocities are relatively high, producing the greatest roughness in the model

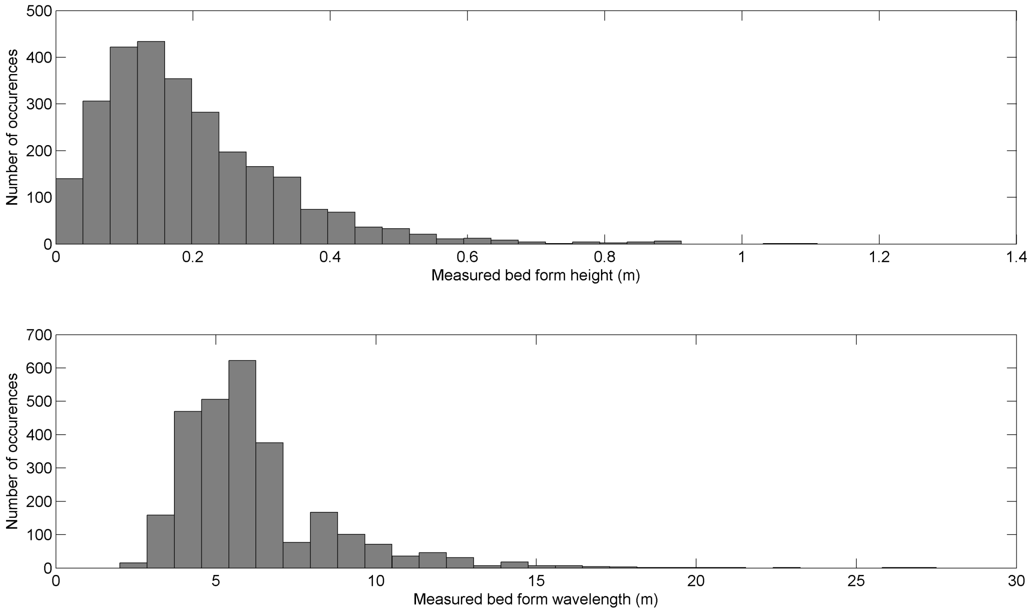

Figure 5.13 – Histograms of the heights (top panel) and wavelengths (bottom panel) of all measured bed forms from the Sonar survey

domain. The calculated values of k_s and $k_{s,r}$ can be seen to fluctuate with the tidal signal, producing two distinctive patterns. Recalling figure 5.1, dune and megaripple roughness increase from zero to a maximum for moderate flows whereas ripple roughness is greatest for weak flows and decreases as flow strength increases. In the model data, this produces two tidally oscillating signals which appear 180° out of phase with each other. This is most noticeable in an expanded view, centered around the peak spring tide (figure 5.15).

In the current implementation of Van Rijn's method the bed roughness is calculated and applied at every time step where $\theta' > \theta_{cr}$. Although this is a suitable procedure (as under the threshold of motion no ripple or dune formation should occur) it is technically incorrect to assume the bed roughness (and therefore bed forms) should be able to evolve at the same rate as changing hydrodynamic conditions. The current model assumes bed forms are in equilibrium with local hydrodynamic conditions which has the effect of allowing bed forms to essentially grow and decay at unnaturally high rates. The time required for ripples to reach equilibrium dimensions is a function of flow strength and can be of the order of hours to hundreds of hours (Baas, 1994; 1999). Tidal currents are constantly varying however, so it may be possible that bed forms are unable to reach equilibrium conditions within a given tidal period. Bed forms must also adapt from a previous form to a new one consistent with new flow conditions—i.e. the history of bed form geometry is important. In this way, bed forms in a tidal environment are continually attempting to 'catch up' with changing hydrodynamic conditions. This history effect is an important omission from the present feedback method and one upon which future work should be concentrated (discussed later).

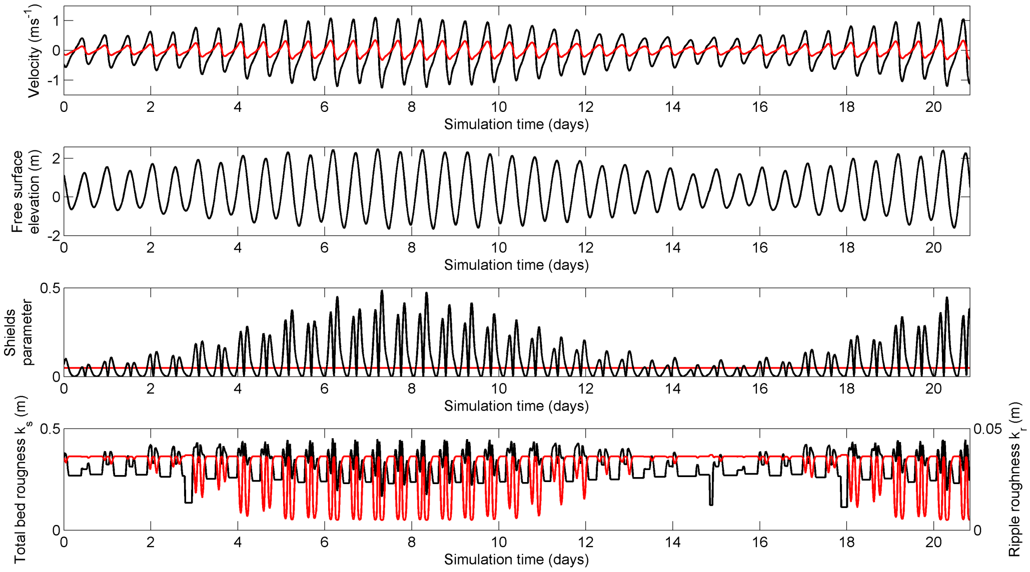

Figure 5.14 – Time series of model parameters from a point located in the scour-pit over the full simulation period of 21 days. From top to bottom: Depth-averaged u (black) and v (red) velocity components, free surface elevation around mean sea level, skin friction Shields parameter θ' (black) and critical Shields parameter θ_{cr} (red) and at the bottom the total bed roughness k_s (black line) on the left axis and the ripple roughness $k_{s,r}$ (red line) on the right axis.

The predicted roughness evolves in time with changing hydrodynamic conditions and therefore not only varies in time (with the tide) but also spatially as a function of depth. Figures 5.16 and 5.17 show maps of the average and maximum values of k_s over the simulation period. The largest k_s values are predicted around the mouth of the estuary, consistent with the large tidal

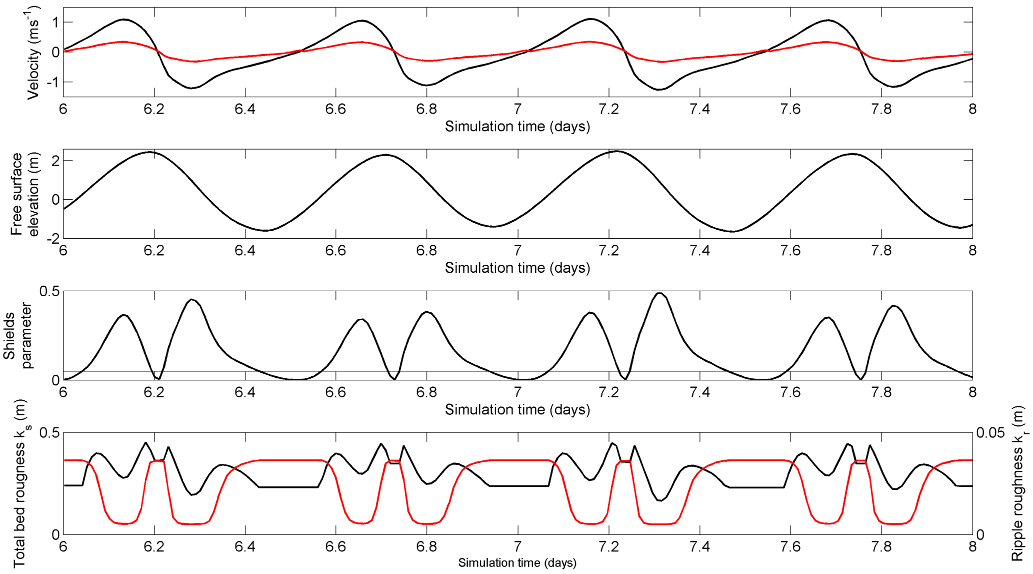

Figure 5.15 – Time series of model parameters from a point located in the scour-pit over peak spring tidal conditions. From top to bottom: Depth-averaged u (black) and v (red) velocity components, free surface elevation around mean sea level, skin friction Shields parameter θ' (black) and critical Shields parameter θ_{cr} (red) and at the bottom the total bed roughness k_s (black line) on the left axis and the ripple roughness $k_{s,r}$ (red line) on the right axis.

velocities funneled through the constriction created by the spit and convergence over the scour pit. k_s values upwards of 0.2–0.4m are predicted around the estuary mouth, with a maximum k_s of 0.05–0.15m in the estuary interior. This is consistent with the general decrease in tidal velocities as the estuary becomes more shallow upstream. Depths and velocities are greatest in the estuary interior within the main channel which is where the highest local roughness lengths are predicted. The average roughness is approximately 50% that of the peak at the estuary mouth, highlighting the significant tidal variation. However in the estuary interior the average predicted k_s is approximately 65% of the maximum, indicating a lower degree of variation.

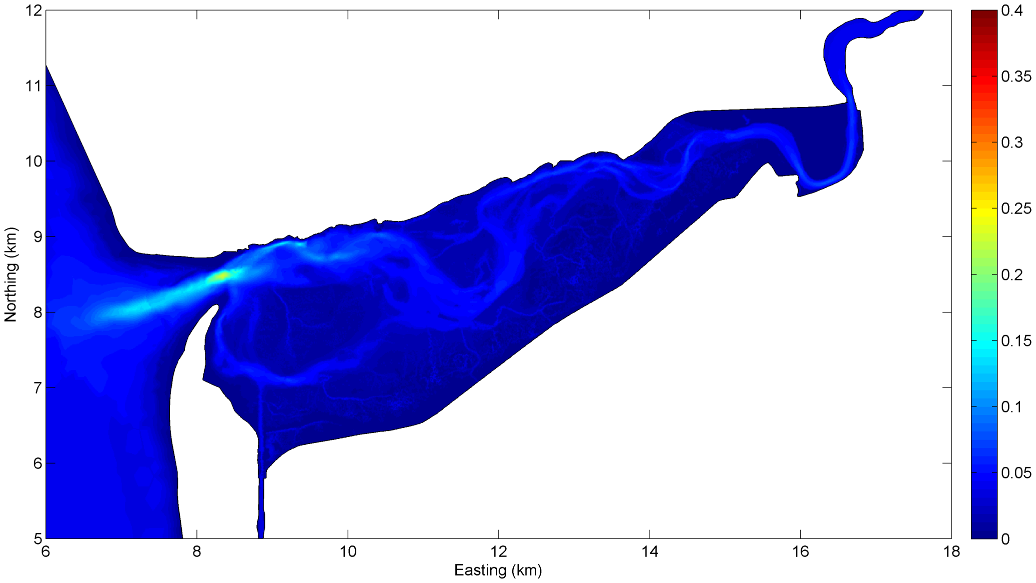

Figure 5.16 – Map of average modelled values of k_s (m) from `TELEMAC 2D` in the Dyfi over the simulation period. The largest roughness lengths can be found in the area around the scour pit where velocities are generally greatest.

5.5.4 Comparison of calculated k_s with Sonar data

To compare the calculated values of k_s from `TELEMAC 2D` and `SISYPHE` with bed form dimensions extracted from the sonar data they first must be put into equivalent forms. Due to the quadratic summation present in equation 5.8 the total bed roughness is dominated by the contributions of dunes and megaripples. As $k_{s,m}$ and $k_{s,d}$ are roughly equivalent to 0.5η (Van Rijn, 1993) bed roughness magnitudes have been increased by a factor of two (to equal $2k_s$) to directly compare with bed form heights measured from the sonar data. Two profiles (A–B and C–D) were chosen to compare the two data sets—one across the major axis of the scour pit and one further into the estuary interior with lengths of 2km and 950m respectively (figure 5.18). Figures 5.19 and 5.20 show the observed bed form height (black lines) and calculated k_s (red and blue lines) scaled by a factor of two for comparison. Attention is first drawn to the difference in bathymetry (lower panels) between the model and observations. This is due to the difference in time between the two bathymet-

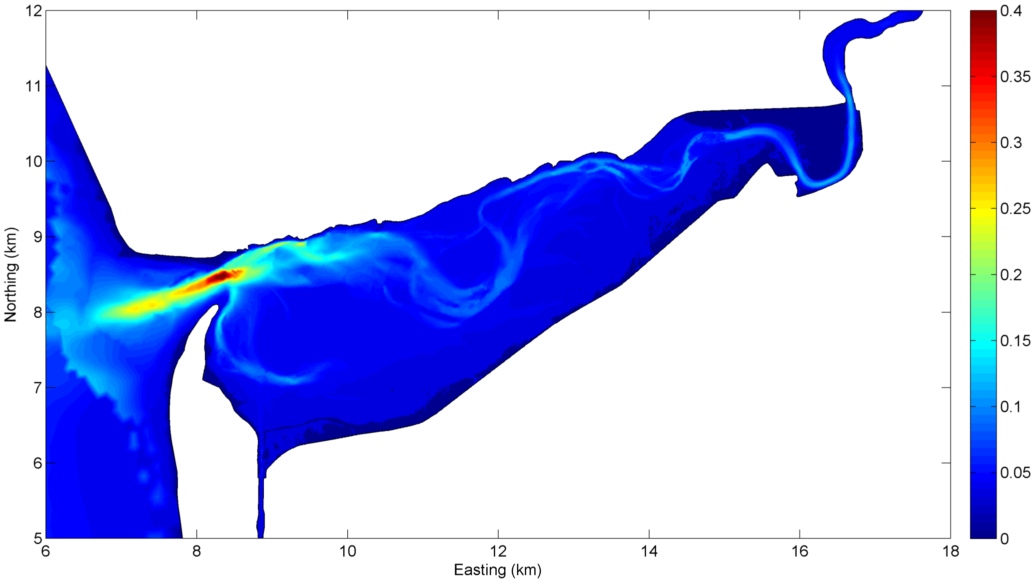

Figure 5.17 – Map of maximum modelled values of k_s (m) from `TELEMAC 2D` in the Dyfi over the simulation period. In general the maximum roughness is twice the average.

ric surveys—the model bathymetry is based on the 2004 lidar survey whereas the sonar survey was conducted in 2007. The average absolute difference between the two bathymetric profiles was 0.78m, with a maximum of 2.98m and a standard deviation of 0.57m. As depth-averaged flow speed, bed shear stress and ultimately the formulation for k_s are dependent on depth, this difference in bathymetry (which is significant in some areas) should be taken into consideration when comparing model results and observations. A second consideration is the numerous simplifying assumptions that were made (uniform D_{50}, absence of waves, steady river input) may have contributed to different near-bed environments in the model and in the field at the time the data were collected.

In the upper panels in figures 5.19 and 5.20 the three separate simulation curves represent the average $2k_s$ (solid blue line, averaged over the simulation period), maximum $2k_s$ (solid red line, maximum over the simulation period) and the maximum $2k_s$ over the neap tide (dashed red line, taken as the maximum between days 14 and 16—see figure 5.14). Both maximum $2k_s$ profiles show values that are larger on average than the observations, being

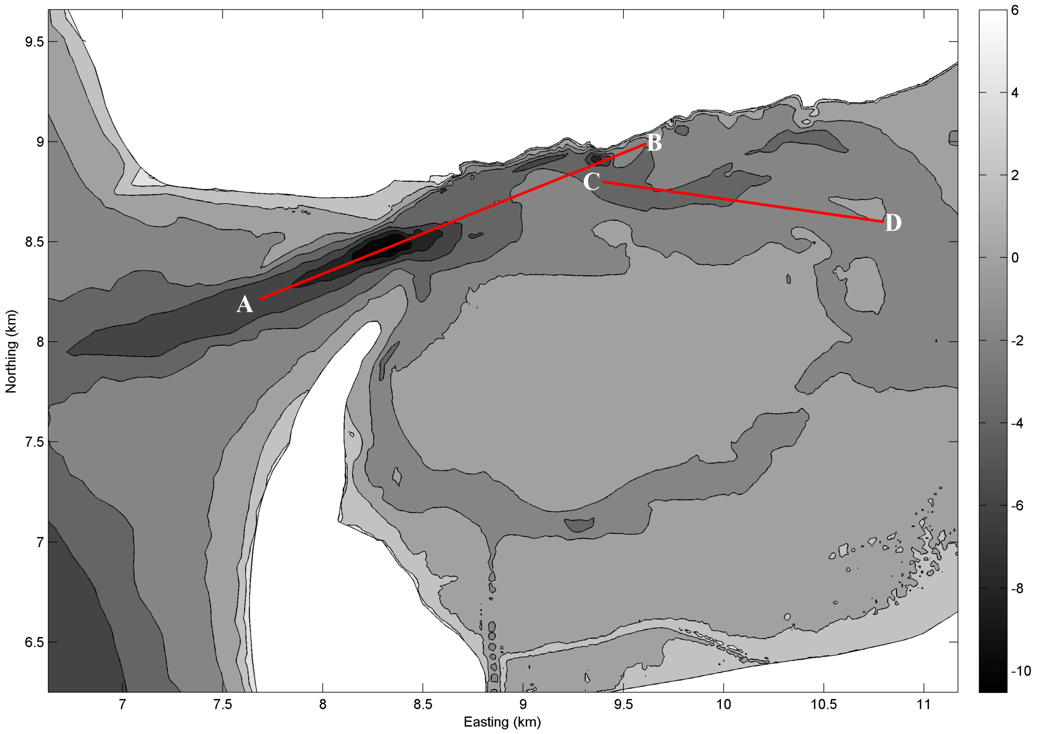

Figure 5.18 – Location of profiles to compare model and measured roughness and bed form height. The profiles A–B and C–D were chosen to extend through as much of the sonar data as possible while minimising interpolation. Bathymetry contours are in meters around mean sea level.

approximately twice that of observations towards the mouth (profile A–B, figure 5.19) with the difference decreasing towards the interior of the estuary. The difference in spring and neap tide maximums in k_s (red lines) is variable across both profiles, with the difference increasing in shallower water across profile A–B. This is most likely due to the presence of the main tidal channel that both profiles intersect (see figure 5.18). The main channel is inundated with water over both spring and neap tides and due to its role as the main escape for the ebbing tide constrains the flow and attains relatively similar maximum velocities (especially closer to the mouth) on both springs and neaps, therefore attaining relatively similar maximum simulated values of k_s due to its dependence on the flow speed in equations 5.2–5.7.

The maximum calculated bed roughness corresponds to the largest (highest) bed forms predicted to occur over the observation period. Although the dimensions of bed forms will adapt towards equilibrium with a given flow condition, the oscillating nature of tidal flow and the long development time required for bed forms to reach equilibrium dimensions means that the maximum k_s may never have in reality been reached. This is evident in figures 5.19 and 5.20 where in both cases the observed bed form height is significantly smaller than the scaled bed roughness.

The average k_s once scaled by a factor of two, shows significantly better agreement with the observed bed form heights. Averaged to 15m grid resolution to coincide with the model (solid black lines) the sub-grid scale bed form height shows promising similarities to the average $2k_s$ curves in both profiles. Profile A–B (figure 5.19) intersects the major axis of the elliptical scour pit at the mouth of the Dyfi. This permanent and stable feature is also the deepest point in the estuary at over 12m below MSL. The model predicts the largest roughness in this area due to the large depth and constriction of both ebb and flow tidal flows that lead to large currents (and therefore mobility parameter ψ). However the observed bed forms in the scour pit were relatively small in the deepest section and few in number. Whether this is representative of bed conditions other than at the time of measurement is not known, although it is speculated that due to the regularity of conditions suitable for large dunes to develop the bed may be rougher in this area at other times of the year. Moving along profile A–B, towards the estuary interior, the model and measurements agree favourably with a general decrease in bed form dimensions between 800m and 1400m along the profile. Here the measured bed form height lies approximately between the maximum and average calculated $2k_s$. There is an increase in both modelled and measured bed roughness at 1800m along the profile that co-incides with the intersection of profile A–B with a bend of the main tidal channel. The model reproduces this relatively well, with the measured bed form height lying approximately between the maximum and average calculated $2k_s$. Profile C–D (figure 5.20) shows similar agreement between calculated and observed bed form heights, with much of the measured heights lying on or around the average $2k_s$ curve.

The differences between model results and observations could be down to a number of reasons. Firstly it is assumed that Van Rijn's k_s method is able to accurately capture the average total bed roughness within a grid cell, however it is stated to only be able to capture the general behavior of the total roughness and reproduce roughness to within the correct order of magnitude. One source of error is the inclusion of only a single, uniform grain diameter in the model. Grain size in the Dyfi is known to be, on average, approximately $200\mu m$ but ranges from $700\mu m$ (coarse sand) at the mouth of the estuary to $64\mu m$ (very fine sand) at the banks of the southern salt marshes (Dollman, 2008). The coarser sands towards the mouth are the most interesting, however, as this is where some of the largest differences between model and measurements were found. Grain size has a strong effect on bed form dimensions, especially dunes (Van Rijn, 2007) and comes into the k_s formulation in the form of ψ.

Secondly, the linear dependence of $k_{s,m}$ and $k_{s,d}$ on h (Equations 5.5 and 5.7) means that the differences in bathymetry between the model and observation period will be manifest in a change in the calculated total bed roughness. A more accurate bathymetric data set can therefore be expected to improve the prediction of k_s. As mentioned previously however, a more accurate bathymetric data set should also improve the modelled hydrodynamic data which will have an additional affect on k_s through the mobility parameter ψ (is also linearly proportional to U).

5.5.5 Impact of k_s feedback on sediment transport

As seen previously, the introduction of hydraulic roughness feedback to `TELEMAC 2D` has a marked effect on calculated depth-averaged flow speeds and even the speed of the propagating tidal wave in a shallow estuary such as the Dyfi. The inclusion of ripple roughness into the calculation of sediment transport has been well studied, and the effect of bed roughness on flow computation has also been extensively reported. However the effect of the feedback of time-varying dune roughness between sediment and flow modules has not had significant attention. The impact of this feedback interaction on sediment transport may not be as simple as to slow depth-averaged currents, as bed friction also enters the bed shear stress equation in the form of the

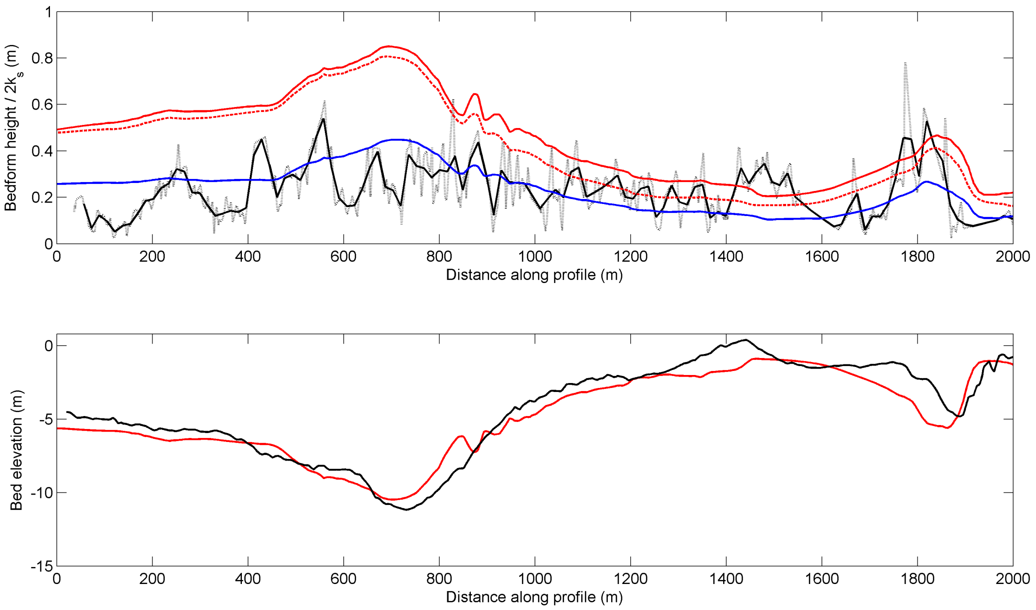

Figure 5.19 – Top panel: Profile A–B of bed form heights η from sonar data (black lines, solid corresponds to data averaged to 15m model grid resolution, dotted line is raw data) and calculated k_s, scaled for comparison. Coloured lines correspond to $2k_s$ for the simulation average (solid blue), spring tide maximum (solid red) and neap tide maximum (dashed red). Bottom panel: Corresponding bed elevations across the profile from the sonar data (red line, 2007) and model (black line, 2004).

drag coefficient C_D and also the sediment transport formulation in the form of the ripple roughness $k_{s,r}$. Importantly however, there is a complex relationship between the current speed and flow depth and the two components of roughness—k_s and $k_{s,r}$, the total and the ripple component, that are used by `TELEMAC 2D` and `SISYPHE` respectively. It is therefore important to understand the impact of not only roughness itself on sediment transport but the *feedback* of roughness in a morphological system.

To test the impact of roughness feedback on sediment transport the Dyfi validation model was simplified to run with a single tidal constituent, with a period M_2 of 12.42 hours and an amplitude of 1.5m. The model was spun-up for one tidal period with a time-step of 5s to remove any start-up instabilities. The model was then run for two tidal cycles in coupled mode with k_s feedback activated and for comparison the same period in coupled mode but with the

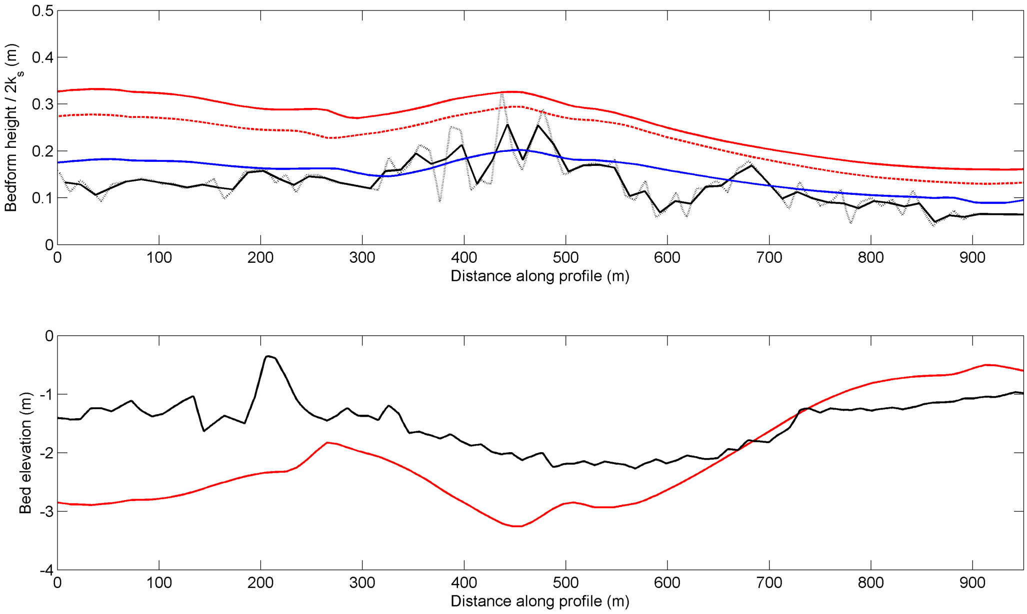

Figure 5.20 – Top panel: Profile C–D of bed form heights η from sonar data (black lines, solid corresponds to data averaged to 15m model grid resolution, dotted line is raw data) and calculated k_s, scaled for comparison. Coloured lines correspond to $2k_s$ for the simulation average (solid blue), spring tide maximum (solid red) and neap tide maximum (dashed red). Bottom panel: Corresponding bed elevations across the profile from the sonar data (red line, 2007) and model (black line, 2004).

feedback of k_s to `TELEMAC 2D` disabled. The ripple roughness $k_{s,r}$ is still calculated and used by `SISYPHE` for the sediment transport computation, but `TELEMAC 2D` only uses a constant total roughness (1cm). Sediment transport was calculated using the total load transport formula of Bijker (1968) in a current-only mode. This was chosen over the bed load formula of Van Rijn (1984a) due to the use of $k_{s,r}$ in Bijker's formula as well as being a more complete representation of sediment transport processes (total load as opposed to bed load only). Time series of free surface elevation z_s, velocity magnitude $\bar{U}$, bed shear stress τ_0, roughness components k_s and $k_{s,r}$ and sediment transport flux Q_s were taken from two point locations—the scour pit and a point mid-way up the main tidal channel (figure 5.21).

Figure 5.22 shows time series of model variables from point 'A' in the scour pit. Here flow velocities and depths are the highest in the estuary

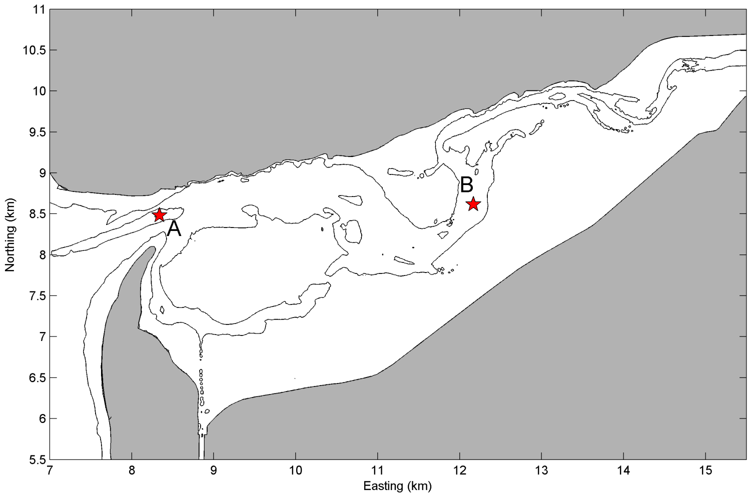

Figure 5.21 – Locations of extracted time-series A & B (figures 5.22–5.23) in relation to the Dyfi's main channel

and subsequently yield the highest calculated values of k_s. The addition of k_s feedback is manifest as a reduction in $\bar{U}$ of 8% on average. However the significant increase in bed friction arising from the calculated k_s (0.4m compared to 0.01m for the non-feedback case) leads to a significant rise in average τ_0 at the bottom of the scour pit of 122%. The increased bed shear stress and the presence of ripple roughness on the bed leads to an average increase of total sediment transport flux Q_s of 74%—a significant increase which in the long term could lead to extensive differences in morphological evolution.

Interestingly, the feedback does not always result in an increase in Q_s. Figure 5.23 shows time series from point 'B', half-way up the tidal channel. Here flow depths are shallower than in the previous example (maximum of 3.5m rather than 12m). Flow rates are also slower, with a maximum velocity of just over $0.5ms^{-1}$. The addition of k_s to the flow computation has a more pronounced effect due to the shallower flow, reducing velocities by 13% on average. The increase in τ_0 is much smaller here however at 29%, with a shift in the phase of peak stress of approximately $0.05T_{M2}$ (0.6 hours). However even with this increase in shear stress the k_s feedback model, in this case, produced a reduction in total sediment trasnport of 34%. This is due to the total-load sediment transport formulation of Bijker (1968) predicting the suspended load transport as the depth-integrated product of sediment volume concentration and velocity. The decrease in $\bar{U}$ in the k_s feedback case therefore has a greater impact in this shallow, low flow rate area than the increase in τ_0 through bed friction.

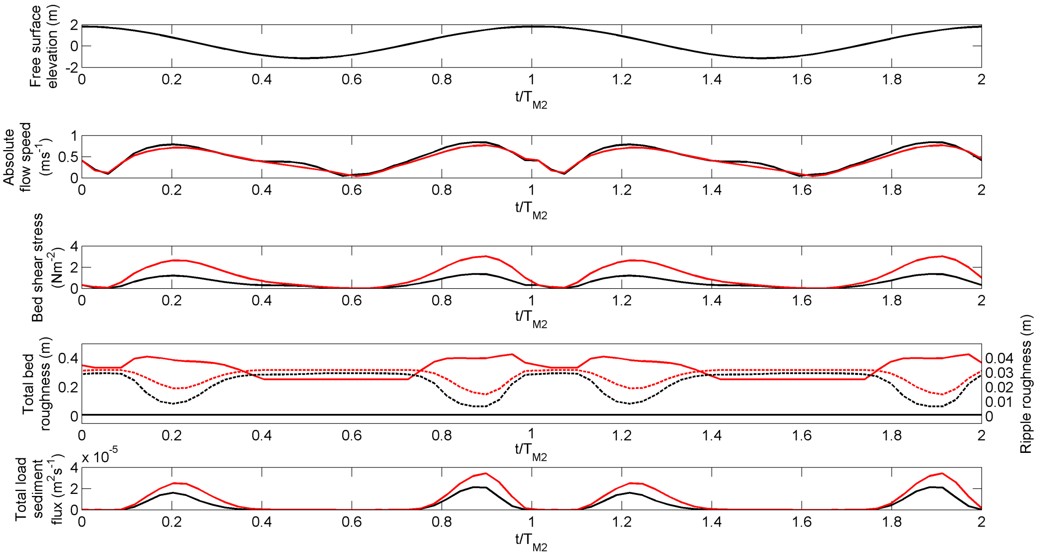

Figure 5.22 – Time series from point 'A' in the scour pit over two tidal cycles. Red lines denote results from model with k_s feedback and black without. From top to bottom: z_s, $\bar{U}$, τ_0, k_s (solid lines, left axis) and $k_{s,r}$ (dashed lines, right axis) and in the bottom panel Q_s.

5.6 Summary

The introduction of time-varying roughness (especially dune roughness) is an important addition to `TELEMAC 2D`. Although the impact on the depth-averaged flow speed may be relatively small the subsequent effect on bed shear stresses and sediment transport rates are significant. An important observation is that the impact of k_s feedback is both non-linear and variable with depth and flow rate to the point that in some areas sediment transport may be enhanced while in others it may be reduced. This suggests that the longer-term pattern of sediment transport, and therefore morphological

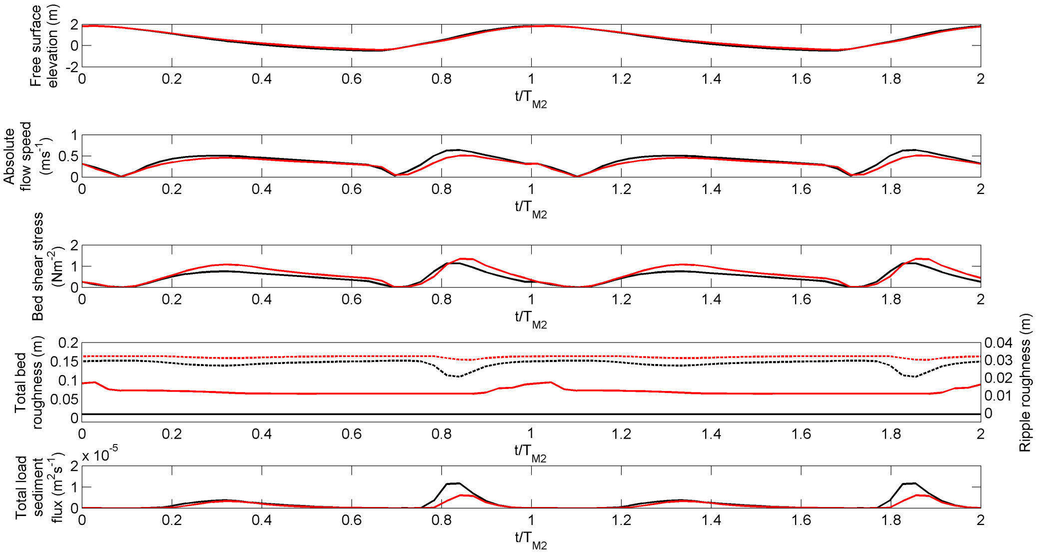

Figure 5.23 – Time series from point 'B' half way along the main tidal channel over two tidal cycles. Red lines denote results from model with k_s feedback and black without. From top to bottom: z_s, $\bar{U}$, τ_0, k_s (solid lines, left axis) and $k_{s,r}$ (dashed lines, right axis) and in the bottom panel Q_s.

evolution, may be altered significantly by the addition of roughness to the flow computation.

The presented model contains a number of simplifications and assumptions that should be noted when considering the simulation results presented in this chapter. As such there are six key areas where the model could be improved:

1. Van Rijn's method currently does not include bed form history effects, which are expected to reduce the calculated roughness as the bed forms may never reach equilibrium dimensions with the tidal flow.

2. The presented model considered a single, uniform grain size. The mean and median grain size is known to vary spatially in the Dyfi, which is expected to affect the predicted roughness through D_* and ψ. Cohesive sediments are also not accounted for.

3. The differences in bathymetry between 2004 (the LIDAR survey used for the model bathymetry) and the observation period in 2007 likely

contribute to the greatest source of error through differences in the position of the main channel, channel depth etc.

4. The inclusion of yearly-averaged flow rates for the rivers Dyfi and Leri rather than time-variable discharges introduced errors in the flow-rate of the main channel due to the occurrence of a river flood during the observation period. Time-varying river flow rates would improve the model predictions, especially if the differences in bathymetry can be resolved.

5. The omission of waves was necessary due to the lack of internal coupling between wave module `TOMOWAC`, `TELEMAC 2D` and `SISYPHE` at the time the present work was undertaken. Waves are known to be important at the mouth of the Dyfi and it is expected that the addition of waves will increase bed shear stresses at the mouth which will affect bed roughness predictions.

The validation of Van Rijn's 2007 bed roughness predictor with an extensive bed form data set is very encouraging, showing that although the simulation and observations operated under different conditions (both in terms of bathymetry and simplified model parameters) the general trend and magnitude of dune-scale bed roughness might be adequately estimated. As the resolution of the sonar data set could only resolve dune-type bed forms over 2m in length the agreement between simulation and observations might be due to the longevity of larger bed features which may not be so susceptible to decay or destruction by wave or river flood events. Further work should be conducted making sonar measurements over a number of tides, thus observing the evolution of dunes over time. This would also be useful in determining a suitable formulation of a 'history effect' to slow the growth and decay of calculated k_s per time step, thus providing a more realistic time-evolving bed roughness than the current equilibrium approach.

Chapter 6

Probabilism, history and divergent evolution in an open, dissipative system

6.1 Introduction

Geomorphological systems are comprised of a number of environmental controls and forcing factors and many feedback interactions (some of which can be strongly non-linear) in between them. This leads to multiple *degrees of freedom*—the 'choices' or 'paths' that a system can take—in response to one or more of its environmental controls (Phillips, 2007).

Dissipative systems are defined as systems where energy that could be used to perform work (e.g. kinetic) is converted via frictional processes to a 'non-useful' form, i.e. heat (Baas, 2002). Open, forced dissipative systems are classified as those that obtain their energy from an external source (e.g. the sun or the tide) and experience a free and open transfer of both mass and energy with the environment (i.e. outside the boundary of the system). A tidal estuary, for example, can be classified as an open dissipative system. This raises some interesting ideas and concepts that are investigated in this chapter.

The concept of self organisation was referred to in Chapter 4 where a complex morphological system was seen to evolve spontaneously from a flat bed via a regular and spontaneous morphological structure that was dubbed the 'brick pattern'. Importantly, self-organisation is better defined as the spontaneous re-organisation of a system where the original length-scales are 'forgotten'—that is to say the system evolves to a new state irreversibly. This new state may even require more energy to maintain than the previous one, a concept known as 'dissipative structures' (Prigogine & Stengers, 1984) which is impossible under a mechanistic, linear treatment of the physical environment. In a non-linear system with dynamic feedback mechanisms small changes in conditions can lead to large differences in system state, embodied by the concept of the so-called 'butterfly' effect (Lorenz, 1963). However, in a system that evolves in time and that comprises numerous, interacting non-linear feedback processes the history of past system states may be equally important as, or more important than, the initial conditions.

This is especially true in simulations involving a numerical model such as `TELEMAC 2D`. Here the system's history (i.e. the previous time-step) has a direct effect on the system's future. This fact, combined with the discrete, time-evolving nature of the morphological systems already described in `TELEMAC 2D` and `SISYPHE`, leads to the idea that the previous morphological history *before* the previous time-step has an impact on the system's future.

Natural dissipative systems, however, contain a seemingly infinite number of small-scale probabilistic processes which, at certain spatial and temporal scales, cause the system as a whole to appear non-deterministic. `TELEMAC 2D` is a mechanistic model however with each model process being entirely deterministic. This is unsurprising as numerical models are designed to be repeatable—uncertainty in the results is actively avoided rather than encouraged.

In this chapter a degree of probability is introduced into `SISYPHE` and the impacts of this are analysed over three repeat cases using three separate and independent system variables based on the bed morphology (bed length scales, energy dissipation and channel width). The hypothesis is explored that the inclusion of infinitesimal stochastic perturbations (using a perturbation to the critical bed shear stress) to the morphodynamic system can create bifurcations in system variables and self-organisation which are inherent to open, dissipative systems and dissipative structures.

6.2 Probabilism and the threshold of motion

Before any one sediment grain begins to move the forces of friction existing between the grain and others in contact with it must be overcome by the disturbing forces acting on it from the flow. Acting on a discrete grain of sand on the bed (under the action of the flow) are three principal forces in balance—the disturbing forces of lift and drag (F_L and F_D) and the stabilising force of the submerged weight of the grain F_W (figure 6.1). The submerged weight must be overcome by F_D and F_L if the grain is to begin moving (and thus the transport of sediment initiated). Shields (1936) resolved the moments of these forces acting around a discrete, spherical sand grain and produced the now classic shields parameter θ, which represents the ratio of these disturbing and stabilising forces. The critical threshold Shields parameter θ_{cr} represents the minimum disturbing force required to initiate sediment motion. There have been many studies which have related θ_{cr} to sediment properties (namely the dimensionless grain size D_*), resulting in a deterministic formulation for θ_{cr} based on an expansive spread of data (figure 6.2). There is significant scatter in figure 6.2 however, which is a product of the non-uniform nature of the grains themselves and the forces which act

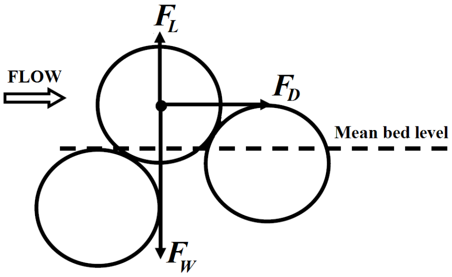

Figure 6.1 – A sediment grain in a flow on the bed experiences three principal forces—the disturbing forces of lift and drag (F_L and F_D) and the stabilising influence of the submerged weight of the grain F_W.

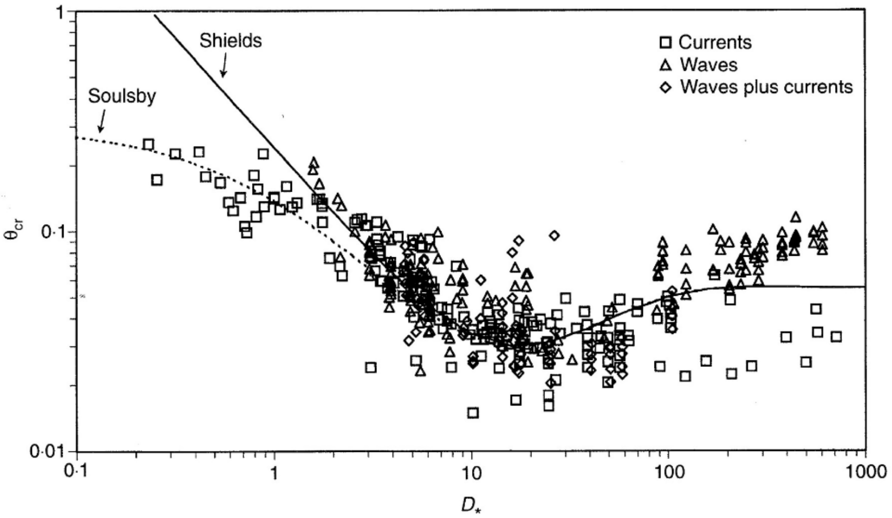

Figure 6.2 – The classical 'Shields curve', with data from the threshold of motion under waves, currents and waves plus currents. Note the scatter of points around the curve, providing evidence that θ_{cr} may be a stochastic variable. From Souslby, 1997.

upon them. Natural quartz sand grains, although relatively uniform, are not perfectly spherical. Imperfections in grain geometry and changes in size between grains on the bed will alter the degree of friction needed to be overcome by the disturbing forces in order to initiate motion. However the disturbing forces provided by the flow are not uniform either.

Close to the bed, turbulence causes fluctuations in the hydrodynamic forces which result in the magnitude of lift and drag forces acting on erodible grains to take the form of a stationary random function of time (Yalin, 1977). Einstein & El Samni (1949) showed that the form of the random lift force can be expressed as a normal (Gaussian) function. Cheng et al (2003) extended this further and showed that the probability function for the critical effective shear stress on a grain in rough-turbulent flow most likely follows a Raleigh distribution.

Therefore if both the stabilising and disturbing forces acting on a grain are non-uniform in space and time then the spread in figure 6.2 may be explained by the theory that the threshold of motion, characterised by θ_{cr}, is a stochastic process and thus the variable that describes it could be stochastic (both in space and time) also.

For simplicity and the purpose of this work it is assumed that a Gaussian probability distribution of θ_{cr} will suffice, with a mean value corresponding to the value of θ_{cr} calculated within `SISYPHE` using the formulae of Van Rijn (1993). The scatter around the centre portion of figure 6.2 (i.e. around $D_* = 3$ which corresponds to medium-grained sand) of approximately 30% was taken as the total variation in the Gaussian distribution, which is approached by two standard deviations in both directions from the mean.

Implementing a stochastic θ_{cr}

To implement a normally distributed random perturbation in the `FORTRAN` environment of `TELEMAC 2D` and `SISYPHE` it is necessary to use a random number generator. A ‘true’ random number is not possible in a deterministic computer, instead a pseudo-random number is picked from a ‘list’ of numbers in a specific range, the list of numbers being very large—for a 32-bit machine over 2^{32} numbers long. As the finite list is so long it is assumed for simplicity that the pseudo-random number is indeed random as to repeat the same number sequence at any one point in the model would take over 2^{32} iterations and thus can be considered impossible. The in-built random number generator in `FORTRAN 90` is the subroutine `RAN`, which produces a random number from an integer ‘seed’ (the index of the random number in the list) which is uniformly distributed in the range 0–1 with a mean value of 0.5. To transform this to a normal (Gaussian) distribution the trigonometric transformation of Box & Muller (1958) was applied, using the method outlined by Press et al (2007).

At each grid node and at each time step two random, uniformly distributed numbers, R_1 and R_2 are first generated by the `FORTRAN` function `RAN`. These are then combined to form a new number R'

$$R' = (2R_1 - 1)^2 + (2R_2 - 1)^2 \tag{6.1}$$

A check on the value of R' is then made. If $R' \geq 1$ then the process is repeated with two new random numbers until $R' < 1$. Once this is achieved then R' is transformed by

$$R'' = \frac{-2 \log R'}{R'} \tag{6.2}$$

The normally-distributed version of the uniformly-distributed random number R_1 is then found as

$$R_{norm} = R'' R_1 \tag{6.3}$$

where R_{norm} has a standard deviation σ of 1 and a mean of 0 (Figure 6.3). To convert R_{norm} into a real perturbation of θ_{cr} it must be transformed into a percentage deviation around its calculated value. A ±7.5% peturbation at one standard deviation was chosen to produce a 30% total variation in θ_{cr} at two standard deviations (or 98% of all instances). However at very low probability events it is technically possible for the variation to reach very high (i.e. $> 2\theta_{cr}$) or very low ($< 100\%$) levels. At very high levels there is no issue as this corresponds physically to an immobile grain. However for large reductions in θ_{cr} a spike in total available stress would result—causing a sudden spike in sediment transport which could lead to bed level instabilities. There is also the possibility of a negative value of θ_{cr} appearing which could potentially cause the computation to stop. Therefore a lower limit of $\theta_{cr} = 0$ was chosen in order to avoid any low-probability instabilities.

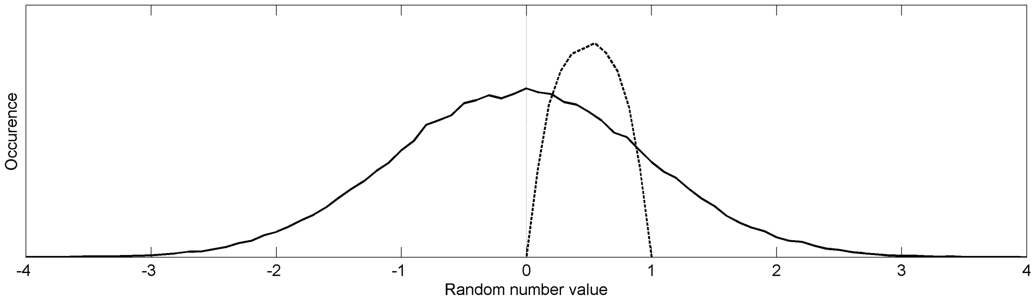

Figure 6.3 – Comparison of the uniform probability distribution of the `FORTRAN` in-built random number generator (dashed line) and the subsequent normal (Gaussian) distribution after the Box-Muller transformation is applied (solid line). The normal distribution is seen to have a standard deviation of 1, with 98% of the variation occurring within two standard deviations. The Occurrence levels for each distribution are not to scale.

The above procedure was programmed into the bed-load sediment transport formula of Van Rijn (1984a) within `SISYPHE` with a simple modification to the formula so that it reads

$$\Phi_b = 0.053{D_*}^{-0.3}\left(\frac{\theta' - (\theta_{cr} + \delta\theta_{cr})}{(\theta_{cr} + \delta\theta_{cr})}\right)^{2.1} \tag{6.4}$$

where $\delta\theta_{cr}$ is the perturbation to θ_{cr} as a result of the random number algorithm. When implemented, this method has been applied at every grid node and at every time-step, so that the variation in θ_{cr} is both stochastic in space as well as in time.

6.2.1 Sediment transport bias due to stochastic perturbation of θ_{cr}

It must be noted that the addition of a random element to θ_{cr} should also introduce a positive bias into the magnitude of the subsequently calculated sediment transport. Taking equation 6.4 as an example, the available shear stress $\theta' - \theta_{cr}$ is raised to some power (in this case 2.1). Due to this nonlinearity, reductions in θ_{cr} (and therefore increases in the available stress) will contribute to greater increases in the magnitude of sediment transport than the increases in θ_{cr}. As this is a stochastic process the net result will be an average increase in the net sediment transport rate.

To test the degree of bias introduced into the sediment transport rate through the perturbation of θ_{cr} the non-dimensional bed load transport rate Φ_b was calculated using Van Rijn's bed load transport formula (Equation 6.4) for a case with $D_* = 5$, $\theta' = 0.5$ and $\theta_{cr} = 0.047$. To capture the full distribution of the stochastic process the procedure was conducted for 10,000 iterations and at each iteration $\theta_{cr} + \delta\theta_{cr}$ was used to calculate a randomly perturbed transport rate Φ_r, with a standard deviation in $\delta\theta_{cr}$ of 7.5% to produce a 30% variance around θ_{cr} at two standard deviations.

Figure 6.4 shows the distribution of the transport bias Φ_r/Φ_b over the 10,000 iterations of the stochastic perturbation method. The distribution curve can be seen to be asymmetrical with a longer 'tail' in the region of positive bias ($\Phi_r/\Phi_b > 1$). This has the effect of forcing the mean of the curve into the area of positive bias also, so that the mean bias in this case is 1.022, or a 2.2% positive increase in mean sediment transport rate. It is the mean value which is of interest when applied to morphological modelling as the stochastic perturbation method will act over a great number of grid nodes and time-steps over the long-term.

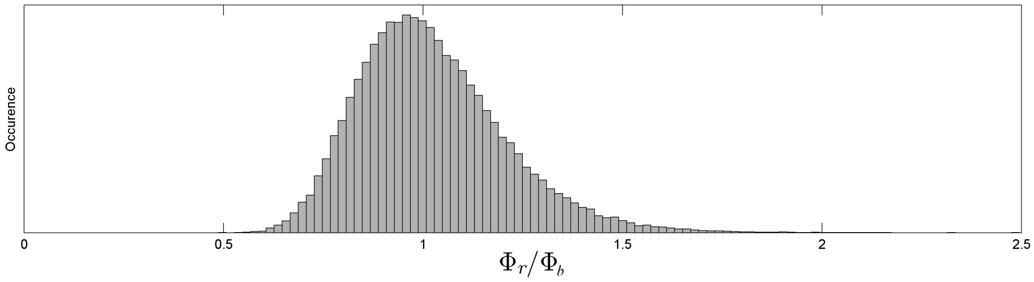

Figure 6.4 – Distribution of transport bias Φ_r/Φ_b over 10,000 iterations of the stochastic perturbation procedure. The original Gaussian distribution is modified by the nonlinear nature of equation 6.4.

The same process was repeated but for increasing θ' (figure 6.5). The procedure was conducted over 1,000 iterations and the average Φ_r/Φ_b taken at each value of θ'. The average bias can be seen to be between 2 and 3% for low to high- flow conditions ($\theta' > 0.15$). However at low values of θ' where $\theta' - \theta_{cr} \rightarrow 0$ the non-linear amplification of the stochasic perturbation of θ_{cr} appears to produce a greater bias—upwards of 15%. This is, however, a 15% increase in a very low transport rate as $\theta' \rightarrow \theta_{cr}$.

It is therefore concluded that, on average, the addition of a random perturbation of 30% (at two standard deviations) into θ_{cr} produces a net, positive bias in the sediment transport rate of between 2 and 3% when using the bed load transport formula of Van Rijn. It can be expected that the degree of bias will vary depending on the transport equation used as this will change the non-linear effect on $\theta' - \theta_{cr}$. As morphological evolution is a direct result of sediment transport a consistent, systematic increase in transport rates will have an effect on the modelled morphodynamics. Although 3% may not produce a significant change in morphology in the short-term the cumulative effect, combined with the deterministic, time-stepping nature of the numerical model will noticeably affect modelled morphology in the long-term.

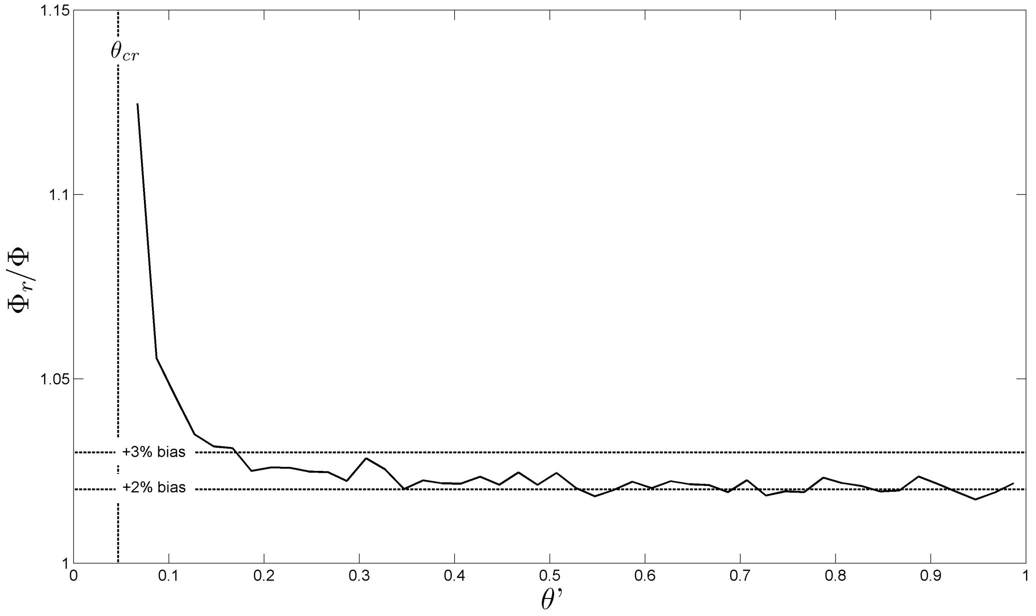

Figure 6.5 – Average sediment transport bias over 1,000 iterations Φ_r/Φ_b for increasing θ' (solid line) with positive bias values of 2% and 3% shown as dashed lines. The curve is not smooth as it represents an average of a stochastic process—the greater number of iterations the smoother it will become.

6.3 Simulation cases

Three model cases were used to investigate the effect of the addition of a stochastic formulation for θ_{cr} on aspects of system evolution. The model bathymetry was of the schematised long and narrow tidal basin of which 100 years of morphological evolution were discussed in Chapter 4. The same M_2 tidal input was used and all input settings (treatment for tidal flats, sediment slide, bed slope effects, etc.) were used also. The difference here is that the updated form of Van Rijn's bed load transport equation with a stochastic formulation for θ_{cr} is implemented (equation 6.4). Three simulation cases were devised, with identical inputs and starting bathymetry (the flat, sloping bed of the model in Chapter 4). However in each repeat case the initial seed integer input to the `FORTRAN` random number generator was different. In this way each case contained a different value of θ_{cr} at every node and at every time step.

To analyse the resulting morphological evolution of each repeat case three independent system variables (dissipation rate, FFT derived perturbation length scales and channel width) were investigated, the formulations for which are described in the following sections.

6.4 Dissipation and morphological evolution

Dissipation D is the rate of loss of energy to heat via the forces of friction and occurs as a result of every physical interaction. This transformation of the internal energy of a system from an ordered (e.g. kinetic) to a disordered form (i.e. the random motion of particles, otherwise known as heat) is in equilibrium with the work done on the system, forming the first law of thermodynamics: *Energy cannot be created nor destroyed, only conserved.* Therefore if the internal energy of the system is to remain constant and work is done on any part of that system then energy will be lost as heat via dissipation.

The degree of irreversibility in an interaction is measured by the entropy S. Entropy is defined as the product of the rate of change of energy $-D$ and the absolute temperature of the system T so that

$$S = -TD \tag{6.5}$$

So for an isothermal system an increase in entropy is directly proportional to the energy lost to heat via dissipation. The concept of Entropy is used most often to describe the future of a system evolving in time. It is a consequence of the second law of thermodynamics that the total entropy of a system will tend towards a maximum (unless the energy lost to frictional dissipation is replaced). It follows that if the equilibrium state of a system coincides with maximum total entropy then the production of entropy (i.e. dissipation) will minimize towards equilibrium (Yang, 1987).

6.4.1 Calculating the depth-mean dissipation

In a hydrodynamic context, the local dissipation of energy from the flow from its work done on the bed can be expressed simply as the product of the total bed shear stress τ_0 and depth-averaged flow speed U (Pugh, 1987) so that

$$D = \tau_0 U \tag{6.6}$$

The dissipation D here is in units of Wm^{-2} of bed surface. As D is related to the third-power of velocity (shear stress is proportion to U^2), dissipation is a very local phenomenon, which in the case of a tidal channel network will be restricted to the areas of highest velocity—i.e. the channels. However it is also heavily dependent on the flow depth h as this has a strong effect on the depth-averaged velocity. Therefore as channels become deeper we can expect the dissipation rate to decrease, and as the most dominantly dissipative areas will be the channels this will have a direct impact on the total dissipation rate of the system as a whole.

In the case of the model results used here the total bed shear stress and depth-averaged flow speed are taken from the output of `SISYPHE`. No extra consideration is necessary for grid nodes that become 'dry' during the tidal cycle as U is set to zero in this case and so erroneous measurements of dissipation over dry cells is not an issue. However, the calculation of D requires that the data be interpolated onto a regular grid as the units of D are per unit area of the bed. The issue arises due to the nature of hydrodynamic variables in `TELEMAC 2D` and `SISYPHE` and the non-uniform placement of mesh nodes and sizes of element areas. As equations are solved on the vertices of mesh elements rather than at their centres, the area that each mesh node is responsible is defined on a polygon with vertices corresponding to the element centres (figure 6.6). The area corresponding to each mesh node is therefore non-uniform and not simple to calculate. By interpolating the hydrodynamic data output from `SISYPHE` onto a regular grid with a set grid node spacing in the x and y directions (i.e. a square grid) the area corresponding to each grid node is uniform and can be treated as a constant.

With the data interpolated onto a regular grid, equation 6.6 was calculated for every point and then averaged across every point in the domain. Due to the choice of procedure for the treatment of tidal flats that was implemented dry grid nodes have zero velocity and therefore zero dissipation. As the tide advances and retreats there will be a continuous change in the inundated area of the basin and therefore the area of the domain with zero dissipation (dry nodes). This is important as an increase in the extent of intertidal flats (due to morphological evolution) will contribute to a reduction in the tidally-averaged rate of dissipation. This should not be ignored as the rate at which the system as a whole dissipates energy (and therefore creates entropy) is of primary interest. Due to the constant area of grid cells in the interpolated grid, the area is treated as a systematic constant and ignored as it will not have an impact on the relative change in dissipation rate with time.

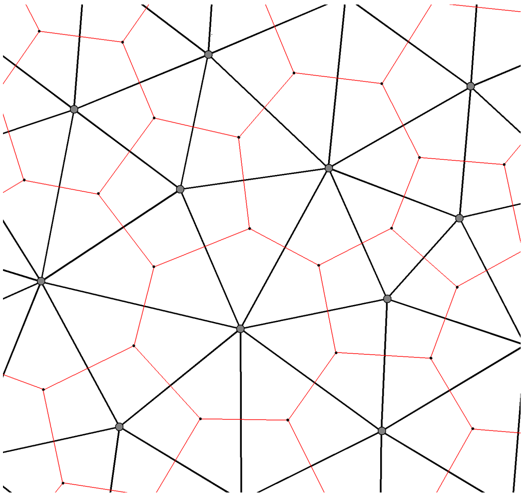

Figure 6.6 – An example of the impact of the non-uniform placement of mesh nodes (filled grey circles) in an finite element mesh (black lines) on the areas governed by each mesh node (red lines).

6.5 Quantifying the scale of bed perturbations

The automated measurement of morphological structures can be a complicated task, due in most part to the wide variety of spatial scales that can be generated on the seabed in the natural environment. Ripples and dunes, tidal channel networks and beach breaker-bars are examples of very different bed form structures which are all generated in the coastal environment and although generated by different physical processes they all share a common aspect. Morphological structures generated in the natural environment are all products of the non-linear feedback relationship between hydrodynamics and the underlying bed. The action of near-bed shear stresses generated by the flow and friction causes erodible sediments to move which shape the bed. This re-organisation of the bed then directly affects the overlying hydrodynamics, resulting in an alteration to the direction and strength of flow.

However, systematically quantifying the scales of bed forms which may or may not be superimposed on each other is no simple task as separating each 'form' of bed structure automatically and over wide areas of bed can be a subjective exercise. Taking a more statistical approach, however, may allow us to systematically measure general spatial properties of a morphodynamic system and if these measurements are made over time the evolution of these spatial properties can be observed.

6.5.1 The Fourier Transform

An aperiodic quantity which varies in space $f(x)$ can be represented as an integral of an infinite number complex harmonic wavenumbers k (with units of $1/x$) in what is known as the Fourier transform $F(k)$ so that (Champeney, 1973)

$$F(k) = \int_{-\infty}^{+\infty} f(x) e^{-ikx} dx \qquad (6.7)$$

with the inverse transform being

$$f(x) = \frac{1}{2\pi} \int_{-\infty}^{+\infty} F(k) e^{+ikx} dk \tag{6.8}$$

with the real and imaginary parts of $F(k)$ representing the amplitude and phase of the wavenumbers respectively. In this way the aperiodic function $f(x)$ can be separated into an infinite number of constituent harmonic waves represented by e^{ikx} which, via Euler's formula, can be further represented by a series of sine and cosine waves

$$e^{ikx} = \cos(kx) + i \sin(kx) \tag{6.9}$$

However the function $f(x)$, if representing data sampled in discrete steps, is difficult to transform using a continuous integral sum. In the case of sampled data, therefore, a different approach must be taken.

6.5.2 Discrete Fourier Transform analysis

The Discrete Fourier Transform (DFT) is a discrete, numerical approximation to the Fourier Transform over a set range of wavenumbers. Take a real (or complex), discretely sampled set of data $f(x)$ of N integer points in length defined on the axis $[x = 0, \delta x, \cdots, (N-1)\delta x]$ where δx is the sampling interval. Its DFT $F(k)$ is defined for $k = 0 : N-1$ as (Briggs & Henson, 1995)

$$F(k) = \frac{1}{N} \sum_{n=0}^{N-1} f(x) e^{-i(2\pi/N)nk} \tag{6.10}$$

and similarly its inverse transform (IDFT) can be written as

$$f(x) = \frac{1}{N} \sum_{n=0}^{N-1} F(k) e^{i(2\pi/N)nk} \tag{6.11}$$

This yields a set of complex wavenumbers $F(k)$ of length N. $F(k)$ contains the amplitudes (real part) and phases (imaginary part) of the modes of wavelengths contained in $f(x)$. The first entry into $F(k)$, i.e. for $k = 0$, represents the mean amplitude of the signal (known as the 'constant' or 'DC' component), followed by harmonic modes representing the data up to $(N-1)\delta x$ of increasing wavenumber. $F(k)$ is 'mirrored' across the point $F(k)_{k=N/2}$ with conjugate complex wavenumbers.

So far only 1-D data has been considered. Bed morphology, however, occupies a 2-D environment and therefore another dimension must be considered in the DFT. Consider a matrix comprising N integer points in x and M integer points in y containing regularly spaced real data points with constant sample spacing in the x and y directions, namely δx and δy respectively (figure 6.7). In two dimensions, the DFT $F(k_x, k_y)$ of bed elevations $z_b(x, y)$ is expressed

$$F(k_x, k_y) = \sum_{n=0}^{N-1} \sum_{m=0}^{M-1} z_b(x, y) e^{-i(2\pi/N)nk} e^{-i(2\pi/M)mj} \tag{6.12}$$

for $k = 0 : N-1$ and $j = 0 : M-1$. Note that $F(k_x, k_y)$ is also normalised for $N \times M$ data points. The inverse transform is

$$z_b(x, y) = \frac{1}{MN} \sum_{n=0}^{N-1} \sum_{m=0}^{M-1} F(k_x, k_y) e^{i(2\pi/N)nk} e^{i(2\pi/M)mj} \tag{6.13}$$

Implementing the DFT numerically in two dimensions is, in practice, a complicated and computationally expensive process. Therefore, fast algorithms for solving the 2D-DFT on discrete data sets have been developed—known Fast Fourier Transforms (FFT). In `Matlab` the standard FFT algorithm is that of Cooley & Tukey (1965), which is essentially a more computationally efficient implementation of equations 6.12 and 6.13. The main difference is that the algorithm gives best results if the input data $z_b(x, y)$ is interpolated onto a grid where N and M are both powers of two.

6.5.3 FFT coefficients

In `Matlab` the output matrix $F(k_x, k_y)$ is slightly complicated in its organisation and so requires some explanation. $F(k_x, k_y)$ is defined on a grid of N, M integer points. However the placement of harmonic coefficients in

k_x, k_y space, the wavenumber *spectra*, are repeated and mirrored within the matrix across the centre-point (figure 6.7). Similar to the 1D-DFT (equation 6.10), the first coefficient (in this case at matrix coordinates $N = 1, M = 1$) represents the sum of all coefficients in both x and y. The first row and column of the matrix contain the mean amplitudes of each column and row respectively. The space $(N = [1 : N/2 - 1], M = [1 : M/2 - 1])$ (lower-left quadrant of $F(k_x, k_y)$ in figure 6.7) is occupied by the spectrum of wavenumbers, mirrored diagonally across the matrix centre-point in the area $(N = [N/2+1 : N], M = [M/2+1 : M])$ with their conjugate coefficients mirrored similarly across the matrix centre-line. The row $(N = [1 : N], M = [M/2])$ and the column $(N = [N/2], M = [1 : M])$ contain conjugates to the mean amplitudes. The wavenumber spectrum is orientated so that low wavenumbers (long wavelengths) appear towards the corners of the matrix and high wavenumbers (short wavelengths) appear towards the centre.

The real part of the FFT matrix corresponds to the amplitude of each constituent wavelength. For example the peak amplitude in a quadrant of the FFT matrix relates to the most dominant wavelength present in the original signal, with each FFT coefficient representing a harmonic of the original data record. To convert the position of spectral peaks in the FFT matrix to peak wavelengths the indices $(k_x(2), k_y(2))$ to $(k_x(N/2 - 1), k_y(M/2 - 1))$ become $(2\delta xN, 2\delta yM)$, or the fundamental harmonics (the data record lengths) in both directions, to $(2\delta x, 2\delta y)$ so that the scaled axes take the form $2\delta xN, \frac{2\delta xN}{2}, \frac{2\delta xN}{3}, \cdots, 2\delta x$ and $2\delta yM, \frac{2\delta yM}{2}, \frac{2\delta yM}{3}, \cdots, 2\delta y$, respectively.

Quantifying basin morphology with a 2D FFT

Quantifying the spatial scales of complex morphologies such as meandering channel-bank systems is inherently difficult due to their tendency to be asymmetric and to have length scales which vary along-channel. The initial perturbations which ultimately create these more complex structures, however, are much more regular and so may be viable candidates for 2D-FFT analysis.

Figure 6.8 shows an example of the so-called ‘brick pattern’ , an initial,

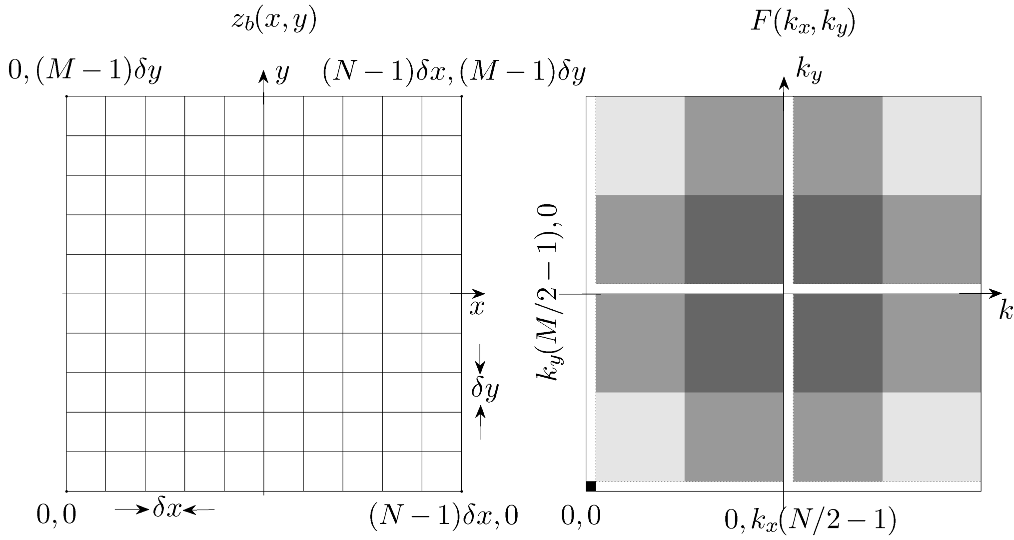

Figure 6.7 – Defined on a grid of integer points, the two-dimensional data set $z_b(x,y)$ is transformed by the 2D-FFT into an equally sized matrix of complex wavenumber coefficients $F(k_x,k_y)$. The wavenumber spectrum is mirrored diagonally across the centre-point and its conjugate mirrored across the centre-line. Low wavenumbers in k_x and k_y appear towards the corners of the spectral quadrants (light grey) and high wavenumbers towards the centre (dark grey). The first and centre rows and columns contain the average amplitudes. Adapted from Press et al (2007).

regular bed perturbation which is subsequently adapted by the flow into larger, more complex channel-bank systems. Figure 6.9 shows an example of the real part (i.e. the amplitudes) of the 2D FFT corresponding to figure 6.8. Note the axes of symmetry between the sets of complex coefficients and their orientation in the FFT matrix explained with reference to figure 6.7. As half of the FFT matrix is redundant (mirrored quadrants A' and B' in figure 6.9) only the lower two halves will be considered, A and B.

Multiplying the two spectra together, the resulting matrix of wavenumber amplitudes $F(\lambda_x,\lambda_y)$ can be plotted on axes scaled to wavelength (figure 6.10). Here we can see that although there is a degree of scatter there are defined peaks in the absolute amplitudes of a select few wavelengths. The actual value of amplitudes in the spectrum are not important here as we are only concerned with *where* in the spectrum the peaks lie.

To use the FFT spectrum to quantify wavelengths present in the bed

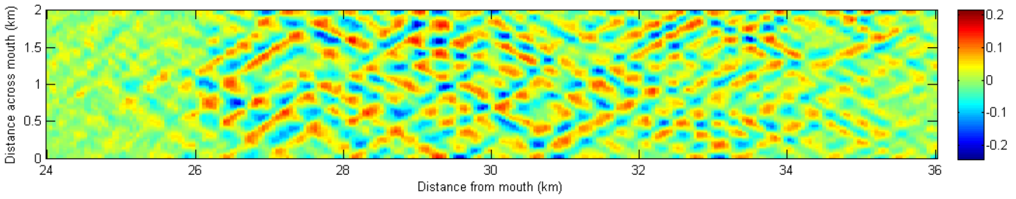

Figure 6.8 – Example of an initial 'brick pattern' on a section of the bed from Chapter 4. Bed elevations are in m, with the initial bathymetric slope removed.

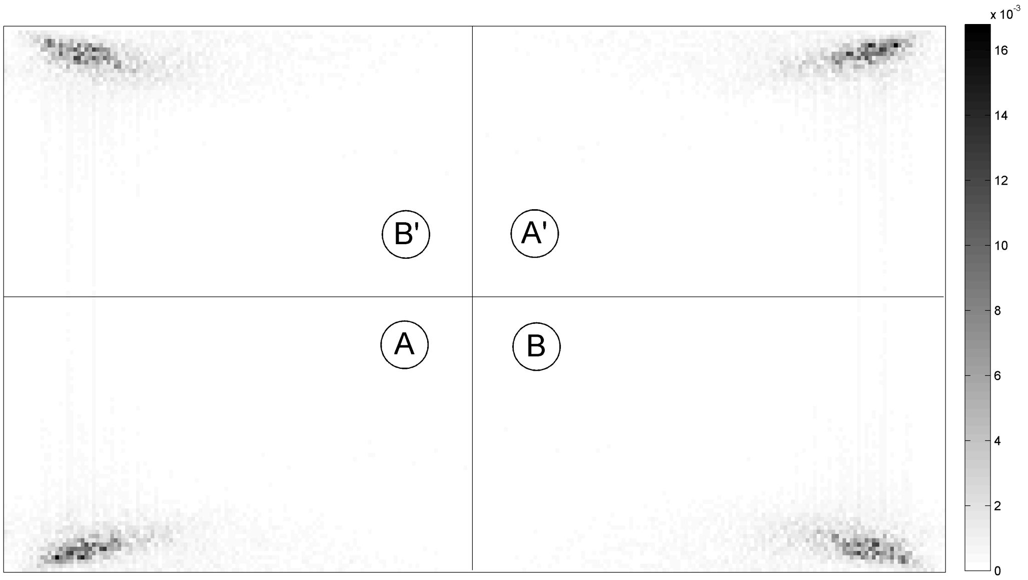

Figure 6.9 – Example of FFT amplitude spectra (absolute amplitudes) of $F(k_x, k_y)$ (units m^{-1}) from the 'brick-pattern' in figure 6.8. Quadrants A and B are conjugates, mirrored diagonally across the centre-point as quadrants A' and B'.

morphology a schematised example is presented. The initial 'brick pattern' can be described by a pair of (x, y) sinusoids interlaced in two dimensions so that

$$z_b = \cos\left(xk_x + yk_y\right) + cos\left(xk_x - yk_y\right) \tag{6.14}$$

where z_b is the bed level (in m) and k_x and k_y are the wavenumbers in x and y respectively. For example, if the wavelengths in the x and y directions were $32m$ and $16m$ (λ_x and λ_y respectively) then the corresponding 'brick

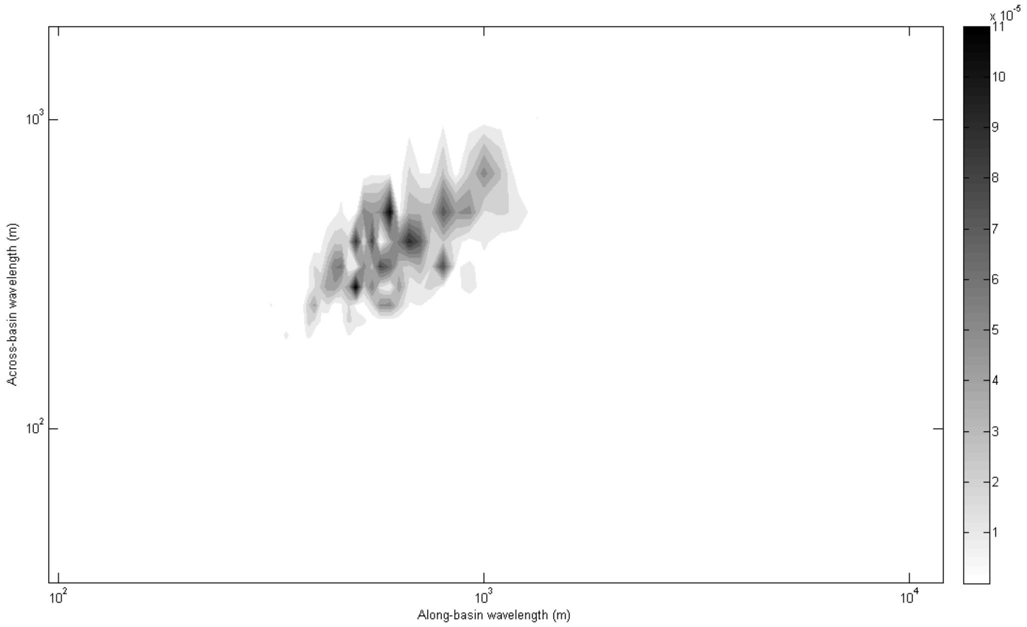

Figure 6.10 – Example of the FFT wavelength spectrum $F(\lambda_x, \lambda_y)$ (units m^{-1}) from figure 6.8.

pattern' would take the form in figure 6.11. The corresponding FFT spectrum is well defined (owing to the single, pure harmonics present in x and y), with a single peak appearing in (λ_x, λ_y) space. With correctly scaled axes the FFT spectrum is able to identify the two constituent wavelengths present in $z_b(x, y)$. The peak appears in both x and y as the FFT 'sees' two wavelengths in the bed. If, however, there was only a wave present in the x direction and none in y the peak would occur only in the first row of $F(\lambda_x, \lambda_y)$.

However, as seen in the spectrum in figure 6.10 (which corresponds to 'natural', and therefore more noisy, data) peak wavelengths are not as well defined and selecting the wavenumber with the largest amplitude (i.e. most dominant in the signal) might lead to a loss of information pertaining to other, less important (but still present) wavelengths in the system.

6.5.4 Centre-of-mass calculation

One potential solution is to take the centre-of-mass (or centroid) of the spectrum. The centroid is the sum of the 'mass' of each coefficient in $F(\lambda_x, \lambda_y)$

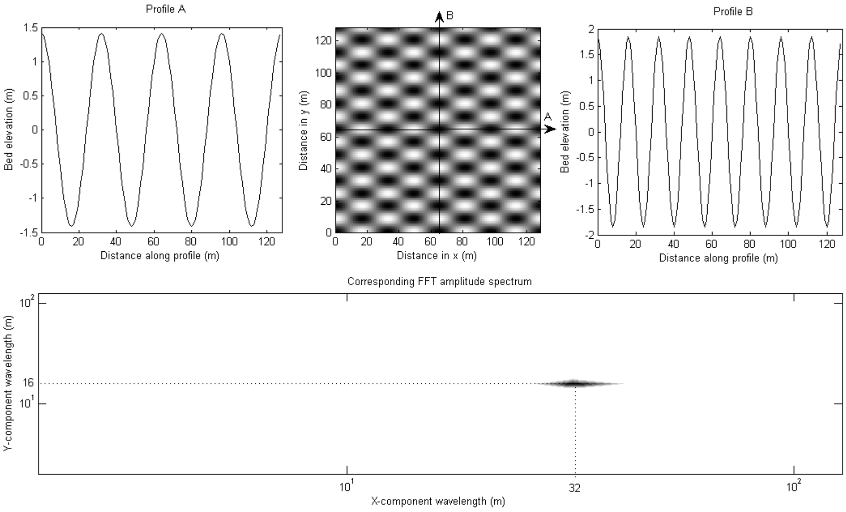

Figure 6.11 – Schematised example of a morphological ‘brick pattern’ (top-centre), constructed from two intersecting sinusoids shown in profiles A and B (top-left and top-right). The corresponding FFT derived wavelength spectrum (bottom) displays a single, well-defined peak (dark area of spectrum) with a position in wavelength space of both $32m$ in x and $16m$ in y (intercepting dotted line).

(their amplitudes) multiplied by their corresponding wavelength in (λ_x, λ_y) space, divided by the sum of all amplitudes so that the x and y components of the centroid ${}_c$ and Y_c are calculated as (Press et al, 2007)

$$X_c = \frac{\sum \lambda_x |F(\lambda_x, \lambda_y)|}{\sum |F(\lambda_x, \lambda_y)|}$$

$$Y_c = \frac{\sum \lambda_y |F(\lambda_x, \lambda_y)|}{\sum |F(\lambda_x, \lambda_y)|} \tag{6.15}$$

where the summation is across all points in $F(\lambda_x, \lambda_y)$ at a particular instance in time. The absolute value of the wavenumber amplitudes are used rather than their real components (thus conserving sign) as the contribution of each amplitude to the ‘mass’ of the spectrum is irrespective of sign. Figure 6.12 shows an example of the calculated centroid for the example wavelength spectrum in figure 6.10 created from the morphology in figure 6.8.

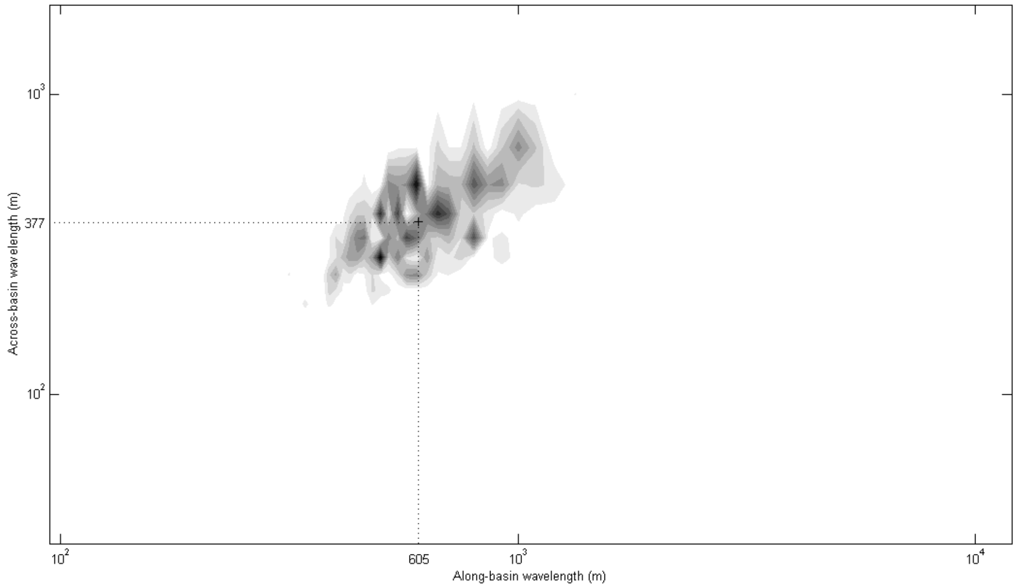

Figure 6.12 – FFT derived wavelength spectrum with position of calculated centroid (dotted lines). Note the positions of higher amplitude peaks with lower wavelengths in x and y contribute to the centroid's position towards the lower end of the spectrum.

6.5.5 FFT analysis method

For each saved time-step (equal to 1/17th of a tidal period) a section of the model bathymetry from x=24–26km (figure 6.13) was mapped onto a regular grid with dimensions N and M of 2^8 and 2^7 points respectively. The section was chosen as the area where the initial brick pattern emerges and so as not to introduce too much un-evolved bed which could skew the FFT towards higher wavenumbers (by trying to fit waves to a flat surface). Next the initial slope and across-basin average elevations were removed so as to consider only pure morphological evolutions from the initial condition. For each time-step the 2D-FFT was applied to the bed data and the wavelength spectrum centroids X_c and Y_c were recorded. For each of the three repeat cases (section 6.3), 1705 time-step instances were recorded.

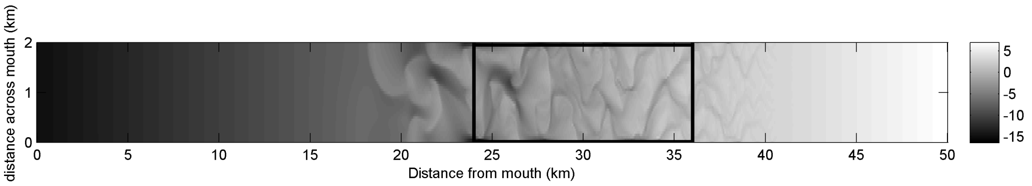

Figure 6.13 – Area of the domain bathymetry (in meters around MSL) covered by the FFT analysis (black rectangle).

6.6 Estimating the width of a tidal channel network

Tidal channel networks are characterised by complicated changes in channel geometry. This is mostly due to the action of braiding where smaller network channels (for example drainage channels from saltmarsh areas) break off from the main channel, resulting in a change of width as the effective flow volume is reduced.

In practice, making a measurement of channel width throughout a tidal network is a complicated task. If the channel bounds were well defined and there was no braiding or branching then the width may be taken as the half-length of a line with a gradient reciprocal to that of the channel bank. This simple method becomes more difficult if the channel banks are not well defined and is almost impossible once branching and braiding takes place. Therefore a more robust method of width estimation is required, and one that can be applied to the network as a whole. Such a method was proposed by Fagherazzi et al (1999) using a combination of the channel bathymetry and image processing techniques. The method was adopted for this analysis and is described in the following sections.

6.6.1 Defining the channel network

The first step in the process is to convert the domain into equally-sized pixels, i.e. to map the `TELEMAC 2D` bathymetric data on to a regular grid. The simplest method of defining channels is then to take any pixels with an elevation z_b below a certain threshold $z_{b,cr}$ to be channels and the rest as flats.

In the case of the model bathymetry, the initial slope was first subtracted from the bathymetry so that it varied around 0m. Figure 6.14 shows the estimated extent of the channel network at four different values of $z_{b,cr}$ for the model bathymetry at an arbitrary point in morphological time. Notice that lower critical elevations yield much smaller channel areas as the sloping banks of the channels increasingly constrain the channel set. An analogy is that the value of $z_{b,cr}$ represents a still water level and the channel pixel set contains only 'wet' bathymetric points. Importantly, the extent of the channel pixel set is directly related to the depth of the channel and the choice of $z_{b,cr}$. Fagherazzi et al (1999) chose a value of $z_{b,cr}$ based on the hypsometic geometry of the tidal basin. However for the purpose of this work a value of -0.1m was deemed sufficient to capture the majority of the tidal network without introducing low-lying tidal flats into the channel pixel set. Even so, fine-scale channel structures are not captured particularly well by the critical elevation method alone as their depths may be less than 0.1m.

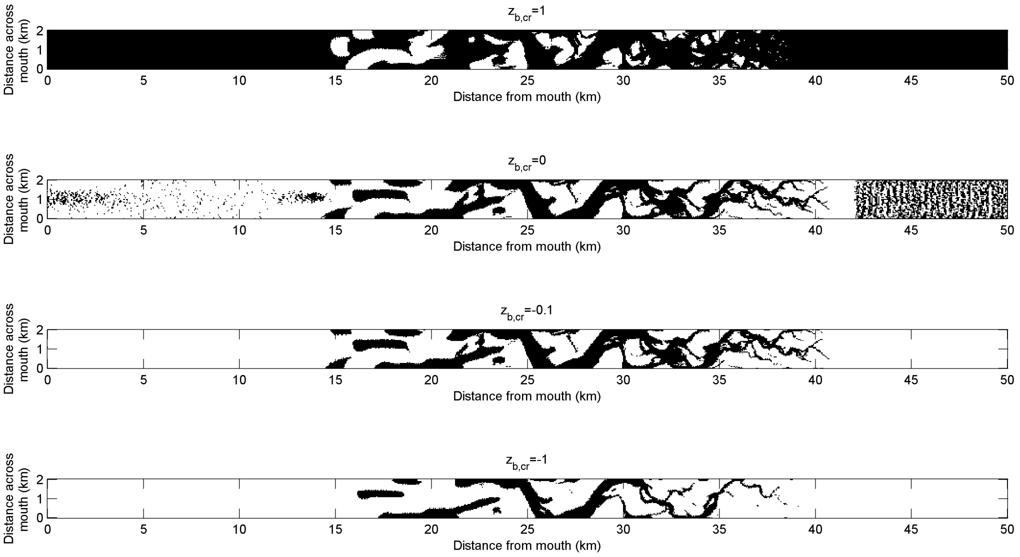

Figure 6.14 – Channel network sets (black pixels) of a tidal channel network for different threshold values of $z_{b,cr}$. Note that the first-order threshold of $z_{b,cr} = 0m$ is in this case not stringent enough and a value of -0.1m produces better results

6.6.2 Automated estimation of channel width

The width at any point in an arbitrarily orientated channel network can be approximated by the diameter of the largest circle inscribed within the channel pixels. Let P_c be a labelled set of size (n, m) of binary channel pixels. At each arbitrary pixel $p(n, m)$ a channel width $W_p(n, m)$ is defined as the the maximum diameter of all circles that can be inscribed in set P_c that includes $p(n, m)$. Figure 6.15 shows a example of the method. Here the diameter of the circle of radius $r = r_1$ describes the width of the channel at the branching point as it is the largest circle that does not cross the channel boundary at this location. However towards the left of the figure the channel is wider so a larger circle with radius $r = r_2$ can be inscribed within the channel. Although the circle diameter only truly represents the width of the channel drawn through the centre of the circle it can be noticed that all points within each circle lie in a portion of the channel with a width of approximately $2r$. In this way the inscription of circles of increasing radius can be used to estimate the width of all points of the channel network from the circle of maximum radius (i.e. not crossing the channel boundary) that can include each pixel p.

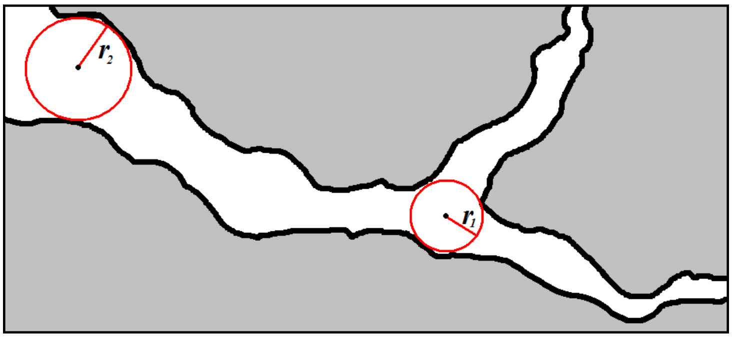

Figure 6.15 – An example of a section of tidal channel network within a domain (white and grey areas respectively) and the largest circles that can be inscribed in two different locations. In each case the areas within each circle lie in a section of the channel network with a width of twice the radius of the inscribed circle.

One way to accomplish this would be to manually inscribe circles of increasing diameter within the channel set and repeatedly check that they meet the criteria. However for large data sets and large channel widths this would be tremendously expensive computationally. To achieve this faster we can utilise some of the unique properties of sets and efficient image processing techniques known as ‘erosion’ and ‘dilation’.

Take a set of labeled channel pixels P_c (Figure 6.16 A). Set P_c is then ‘eroded’ by a circle of radius r. This process removes from the set any pixels which lie less than distance r away from the set boundary, i.e. any channel less than $2r$ in diameter (red pixels in figure 6.16 B) resulting in set P_c' (black pixels figure 6.16 C). P_c' is then ‘dilated’ (expanded) by distance r (red pixels figure 6.16 C) resulting in set W_r (figure 6.16 D). Set W_r is the union set of all circles of radius r that can be inscribed in set P_c and has a width attribute of $2r$. It can also be noted that by construction all channel pixels in W_r belong to P_c. To find a value of channel width W for each pixel p in a set we simply iterate the above process for increasing values of r and save the maximum value of W_r for each pixel. In set notation this can be written as

$$W_p = 2\max\{r : p \in W_r\} \tag{6.16}$$

i.e. W_p is twice the maximum radius r belonging to the set W_r containing pixel p. It follows from equation 6.16 and the discrete increments through which r must be cycled (due to the finite size of channel pixels) that only odd values of $2r$ are possible, as at each iteration of the method r is increased by one pixel and each circle is comprised of a single, whole centre pixel and therefore the possible channel widths follow the circle diameters of 1,3,5 etc. pixels (figure 6.17). The above method was applied to the three repeat cases (section 6.3). At each time instance a ‘map’ of W_p was constructed using equation 6.16. Each map is similar to the form of the ‘wet’ channel network area at each time instance (e.g. figure 6.14) but each channel pixel coincides with an estimate of W_p at each point.

Measurements of channel width W_p were made at each point in the record (every 263 time steps, or 22 minutes of hydrodynamic time) and then averaged into bins corresponding to one morphological year. The mean width of the entire network at each time instance was calculated from the mean

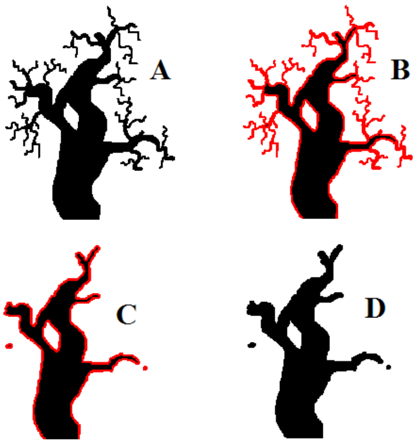

Figure 6.16 – Example of the image processing method of Fagherazzi et al (1999) to estimate channel width in all points of a network. Pixels belonging to the channel network (A) are eroded by a circle of radius r (B, red pixels), resulting in a new set (C, black pixels). This set is then dilated by a circle of radius r (C, red pixels) to form the set W_r (D).

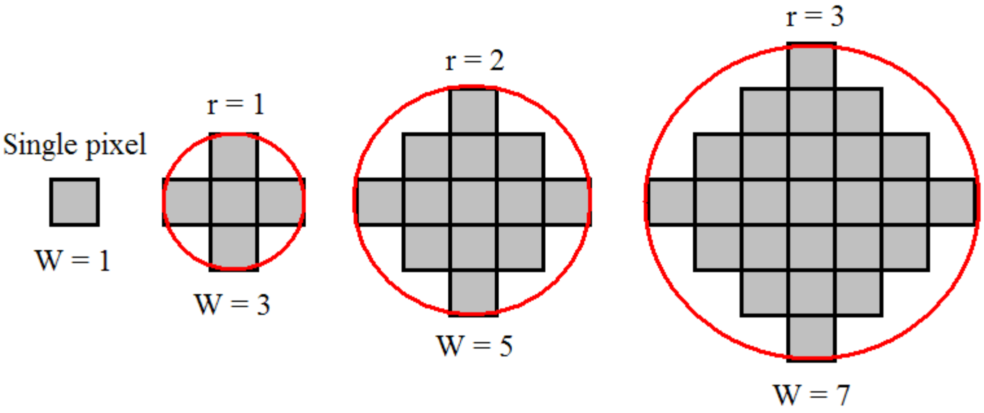

Figure 6.17 – The radius of circles inscribed in pixellated channel data must take into account the initial (centre) pixel. As such, each increase in r must correspond to the addition of pixels around the centre to approximate a circle—i.e. only odd values for W are possible.

width of all channel pixels in each set. The original bathymetric data from `SISYPHE` was interpolated onto a square grid with a resolution (in both the x and y directions) of 50m, corresponding to the mesh resolution of the model. The channel widths were therefore found to be odd integer multiples of 50m (i.e. 50m, 150m, 250m etc.). A finer model grid resolution would allow the identification of narrower channels but in the present model the mesh resolution was deemed as fine as possible in order to keep the node count to a reasonable minimum (due to the size of the domain).

6.7 Method

In each repeat case the initial bathymetry was identical, with the bed sloping linearly from -15m at the mouth to +7m at the head. Each repeat shared the same initial geometry and conlim files, tidal input conditions and general sedimentological parameters and procedures such as grain size, bed slope effects and sediment transport routine (that of Van Rijn, 1984a).

The difference between each repeat case was introduced as a change in the initial 'seed' integer entered into the `FORTRAN` random number generator outlined in section 6.2. This is essential as the random number generator is in fact a string (albeit a very long one) of pseudo-random numbers and if each repeat began on the same number in the sequence every perturbation in θ_{cr} at every grid node and time step would be identical between each repeat. By starting at a different initial seed for each repeat case the perturbation in θ_{cr} was different at every grid node and time step. The exact choice of initial seed is not important, but to avoid introducing any systematic bias the three initial seed integers were chosen to be as 'random' as possible.

Each repeat case was run with a time step of 10s for a period of 100 tidal cycles with an MF number of 705.3456, which combined with the adapted M_2 tidal period (see Chapter 4) of 44710s produces a morphological speed-up of exactly 1 year for every tidal cycle. Due to the scaling of M_2 one tidal period repeats precisely every 17 result print-out periods of 263 time steps. It is important that a tidal period fits into an integer number of time steps which in turn is a factor of the print-out period in order to make it possible to average results over a tidal period exactly and not to introduce any residual effects that could obscure the real, averaged variable result.

The x- and y-component centroids from FFT analysis, basin-averaged dissipation per unit area of bed and basin-averaged channel width were all calculated for each morphological year in the 100 year simulation.

6.8 Results

6.8.1 Morphological evolution

Figures 6.18, 6.19 and 6.20 show the evolution of the bed (initially flat) at intervals of 10, 50 and 100 years of morphological time respectively, with each figure showing comparisons between the three repeat cases at each point in time. Each case can be seen to be very similar by eye, each displaying the evolution of the 'brick pattern' at approximately 10 years morphological time (figure 6.18) which is subsequently adapted by ebb-constrained tidal currents (as in Chapter 4) into complex channel-shoal patterns (6.19) which then persist in their general form and grow into deeper water (6.20). However, at all stages in the evolution of each repeat case, although the general form appears similar, specific differences in morphology can clearly be seen by eye. For example the position of erosional pits and depositional mounds in the initial brick pattern appear in different locations for each repeat case. Later in the evolution of each case the positions of the deeps created by the interaction of the main tidal channel and the domain solid boundary all appear in different positions from each other, although the general depth and form of each is broadly similar.

The regular plan form morphology of the brick pattern is shared between each of the three repeats (figure 6.18), despite the fact that the stochastic perturbation of θ_{cr} leads to random fluctuations in Q_s in both space and time. This shows two things: firstly that the existence of the brick pattern in this system is a product of self-organisation and not initial bed conditions, and secondly that the pattern is more robust than the action of the random perturbation of θ_{cr}—i.e. it is a product of a wavelength of fastest growth, a concept which is explored later.

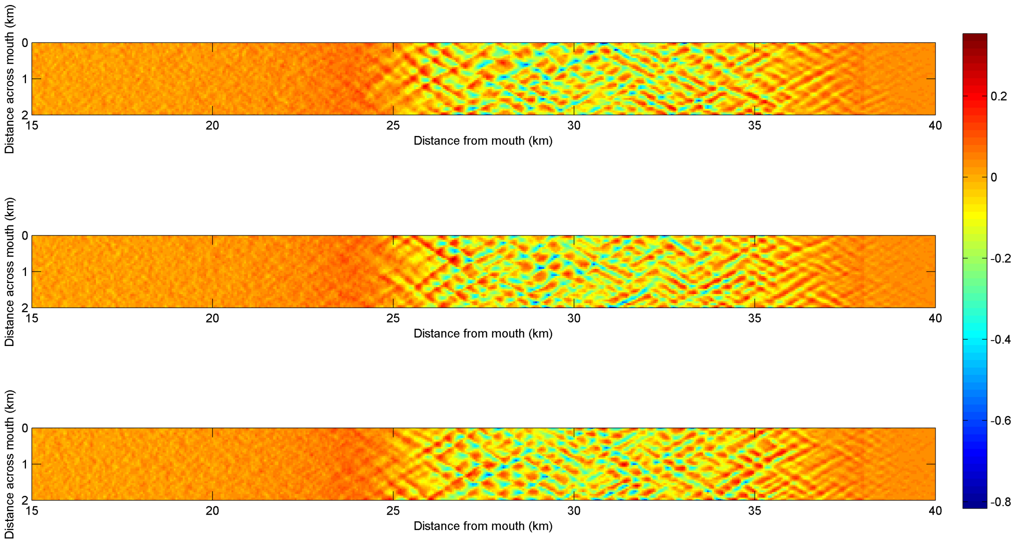

Figure 6.18 – Section of bed elevation z_b from the centre of the model basin for repeat 1 (top panel), repeat 2 (mid panel), and repeat 3 (bottom panel) at 10 years of morphological time. Bed elevations are in meters with the initial slope removed.

6.8.2 Dissipation

Figure 6.21 shows the tide- and basin-averaged dissipation per unit area of bed for the three repeat cases over the 100 year morphological simulation. In each case one tide in hydrodynamic time represents a year in morphological time. Although dissipation is a heavily local phenomenon (related to U^3) the general trend of dissipation rate of the system as a whole is represented by the basin-averaged values. Attention is first drawn to the initial 7 years in each repeat case. Here the average dissipation rate increases to a maximum value common to all three cases in a smooth curve. This is the effect of self-organisation from a flat bed and the emergence of the 'brick pattern'. Dissipative structures are defined as structures (in this case morphological elements) that emerge as the result of spontaneous self-organisation and require more energy to maintain than the structures which they replace (Prigogine & Stengers, 1984). Here the initial, flat bed is out of equilibrium with the external forcing of the tide and so the system strives to re-adjust. However the system does not adjust linearly, as the spontaneous organisation of the

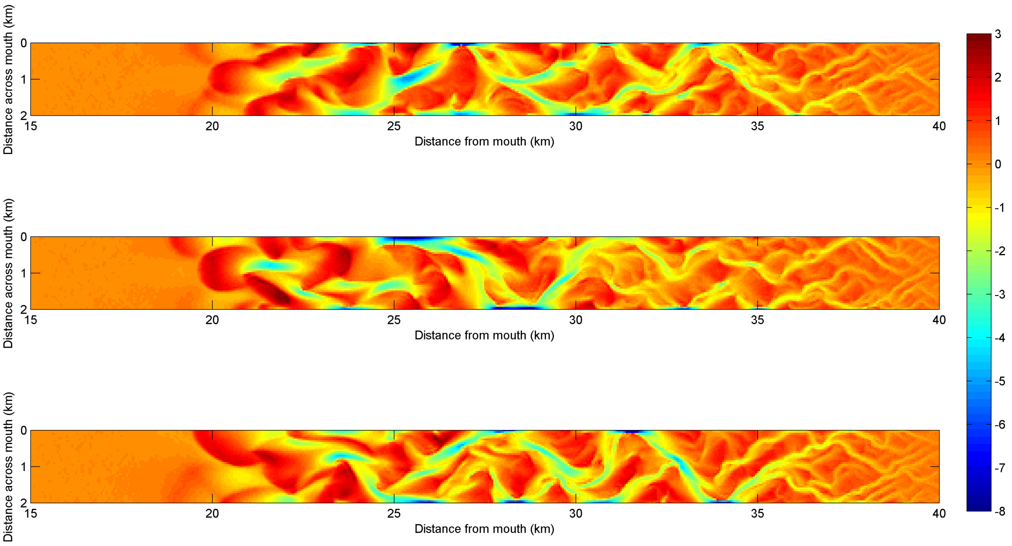

Figure 6.19 – Section of bed elevation z_b from the centre of the model basin for repeat 1 (top panel), repeat 2 (mid panel), and repeat 3 (bottom panel) at 50 years of morphological time. Bed elevations are in meters with the initial slope removed.

brick pattern requires a greater amount of energy to produce (through the transport of sediment) than the initial flat bed. Although the pattern is technically different in each case (figure 6.18) the amount of energy dissipated by each system is almost identical and follows the same trend during self-organisation which suggests the brick pattern is highly regular between each system.

Upon the peaking of basin dissipation at approximately 7 years of morphological time slight differences become evident between each system. This point in time (approx 10 years) corresponds with the constriction of the ebbing tide into the troughs of the brick pattern, creating meandering channels which drain the area on the ebb. From this point onwards each system follows a general trend of decreasing dissipation with time. However each system follows a different 'path' of dissipation—each originating and diverging from the same peak at around 7 years. The trend of generally decreasing dissipation rate shows that each system is striving towards a state of equilibrium with the flow, and not away from it (Yang & Song, 1979). What is interesting, however, is that at some points in the evolution of each system

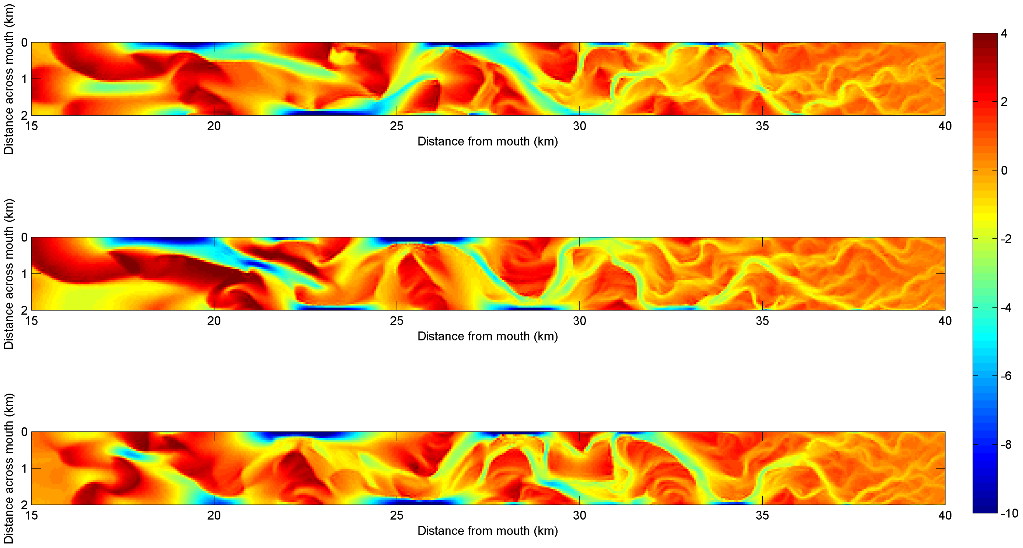

Figure 6.20 – Section of bed elevation z_b from the centre of the model basin for repeat 1 (top panel), repeat 2 (mid panel), and repeat 3 (bottom panel) at 100 years of morphological time. Bed elevations are in meters with the initial slope removed.

dissipation increases for short periods of time. The transport of sediment is proportional to the dissipation of energy at the bed and therefore these increases in the rate of dissipation must coincide with short-term periods of channel-shoal readjustment. An example one of these increases in dissipation rate appears to be shared across all three systems (at approximately 47 years of morphological time) where each systems follows the same 'hump' in the dissipation curve. There is no significant change in bed morphology around this time which suggests this may be coincidental and would not be noticeable in the long term. The divergence of each system from a single point is evidence that an infinitesimal change, in this case random in both space and time, can create significant differences in the future states of systems evolving in time. This may be viewed as chaotic behavior as the general form of each system is similar on the large scale, but significantly different at the small-scale. Critically, the divergence of each system from a single point in time shows dynamically unstable behavior as each system has variable modes of adjustment and different outcomes for similar changes in disturbance (Phillips, 2007).

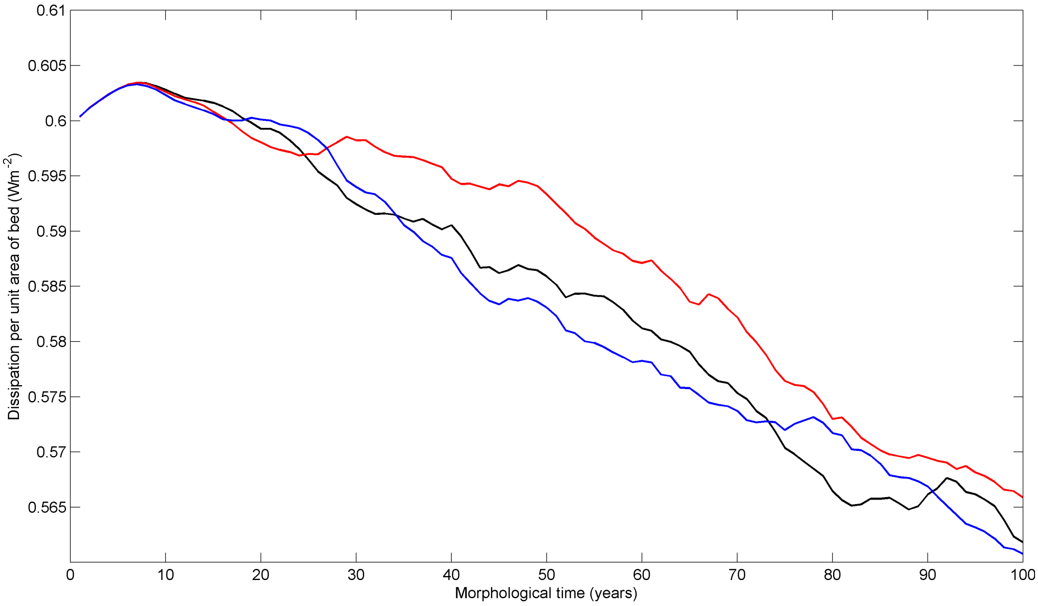

Figure 6.21 – The tide- and basin-averaged dissipation per unit area of bed (Wm^{-2}) for repeat cases 1, 2 and 3 (black, red and blue lines respectively). Due to the effect of the morphological factor, each tide represents one year of morphological time.

Entropy is directly related to the rate of dissipation and as a system approaches a degree of local equilibrium the rate of entropy production (and therefore dissipation) should reach a minimum. As can be seen from section 6.8.1 the channel shoal system has not filled the entire domain by 100 years morphological time. Without extending the simulation into the future it cannot be seen if energy dissipation will reach a minimum, however from the results of Van der Wegen et al (2008) and Van der Wegen (2010) it can be expected that the rate of dissipation will minimise (albeit on the time scale of 1000 years), a topic which should be considered for future investigation. This is also coincident with the degrees of freedom of this particular tidal basin system. From the current results at least three degrees of freedom can be noted (i.e. three curves diverging from a single point). Whether there is a finite or infinite number of degrees of freedom can not be determined from the current work. However if there is a finite number of system configurations, multiple repeats of the same simulation will eventually produce an identical (or very similar) configuration to one that has been produced in a previous simulation.

6.8.3 FFT length scale analysis

The use of FFT analysis on aperiodic, noisy (i.e. ‘natural’) data often produces results that are heavily dependent on data sequence length and the treatment of the ‘ends’ of the data set. It is therefore inadvisable to view the FFT analysis as a way of calculating the wavelength of tidal channels. The centroid of the wavelength spectrum as a whole, however, will be more robust to small changes in morphology which could shift the peak wavenumber as the remainder of the ‘cloud’ of wavenumbers still holds influence over the centroid position. In this way, the centroid should be viewed not as a direct measure of bed form wavelengths, but a general indication of the length scales of bed perturbations in the x- and y-directions as they evolve in time.

Figure 6.22 shows the relative evolution of the x- and y- components of the FFT wavelength spectra centroids for each repeat case. The time component of the plot runs left to right with each curve ending at the right hand of the figure at a point corresponding to 100 years of morphological time. The initial position of the centroids in each repeat case, after a short period of adjustment, lie in a similar area of X_c, Y_c space, with along- and across-basin length scales of approximately 600 and 400 meters respectively. This coincides with the formation of the brick pattern and the peak in energy dissipation before system divergence seen in figure 6.21. Just as in the evolution of the dissipation rate with time, the FFT derived length scales can be seen to diverge, with each system ultimately (at least after 100 years morphological time) ending with significantly different centroid positions than at the beginning. All three evolving paths show increases in both the along- and across-basin perturbation length scales with time. However the FFT analysis assumes a periodic morphology in both directions and therefore very large perturbations (e.g. from the deep pits formed at the boundary of the model in figure 6.20) will be treated as periodic. The size of the domain (in both x and y) provides an upper limit on the scale of the wavelength spectrum (and therefore X_c and (Y_c)). The deep pits at the edge of the domain are interpreted by the FFT as large amplitude, long-wavelength periodic waves that force the centroid to the upper limit of Y_c, i.e. 2km. Two of the three repeats can be seen to reach this upper limit in Y_c by the end of the simulation. However, as stated previously, the FFT analysis is not suitable for measuring bed form geometry and as such the FFT output should be viewed as a relative change in the length scales of along- and across- basin bed perturbations with time. The most important result is that after a period of spontaneous re-organisation bed perturbations grow in time and that the relative scale and rate of growth of these perturbations is different for each repeat case.

This supports the previous finding that each system is morphologically different from one and another. As the tidal energy input is identical in each three cases at all points in time, the differences in dissipation rate must be due to differences in morphology. Although each system appears to share the same general characteristics, the differences in morphology have lead to statistical differences in bed level which create the divergence in centroid position of the FFT wavelength spectra. Although the FFT analysis is not suitable for accurately *measuring* the wavelengths of bed forms such as tidal channels, the statistical robustness of the FFT combined with the systematic method of application to the morphological results of these three repeat cases leads to the conclusion that the differences in centroids represent real differences in general morphology between each system.

6.8.4 Channel Width

A more accurate measure of the morphological elements in each system is the channel width. Here the estimated channel width is based on the 'wet' area of the channel network, averaged over a tidal cycle. Figure 6.23 shows maps of the estimated channel width across the whole system (in this case for repeat number 1) at different points in the 100 year simulation period. From the initial flat bed (0 years, top panel) the system can be seen to evolve through the brick pattern phase (10 years) where the minimum possible channel width of 50m (one pixel) begins to appear in the image. From here the channel

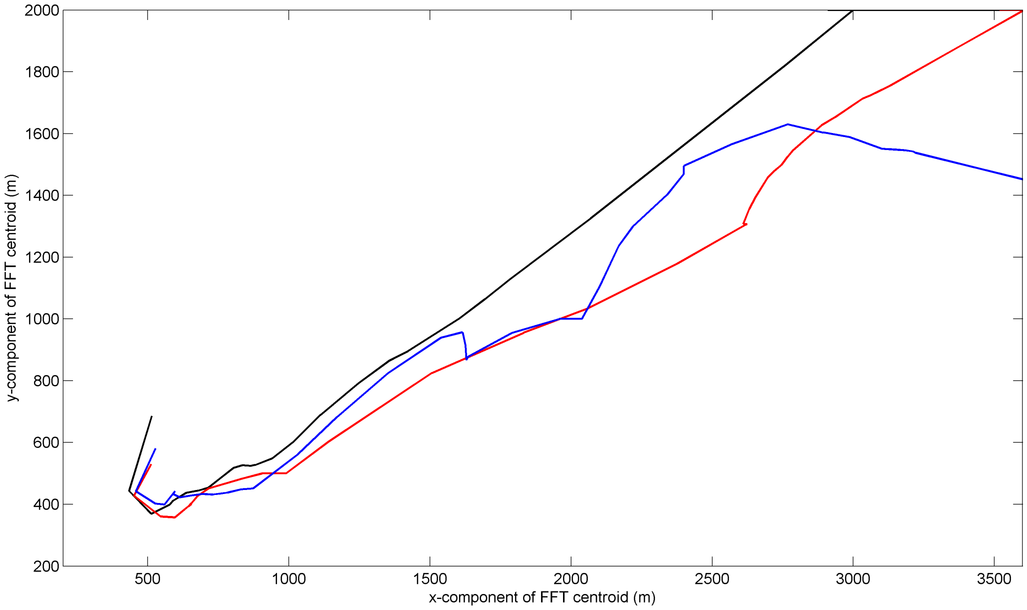

Figure 6.22 – x- vs. y-components (averaged over each morphological year) of the FFT derived wavelength spectra for repeats 1, 2 and 3 (black, red and blue lines respectively) over the 100 morphological years simulation time. Each curve begins at the left of the figure and moves to the right with time (the end of each curve corresponds to 100 years of morphological time).

network migrates towards the basin mouth while existing channels increase in width as they are progressively eroded by tidal currents. In practice, the cross-sectional area of the channel is not simply attained from the product of the channel width and the depth interpolated from the bathymetric data as the width of the channel is recorded at both the channel centre-line and at its banks (due to the circular nature of the estimation method, section 6.6.2). Fagherazzi et al (1999) proposed an algorithm to extract the channel cross-section from the skeletal structure of channel centre-lines, but this has not been attempted in the current work. To compare the effect of system divergence evident from figures 6.21 and 6.22, the tide- and basin-averaged channel width was calculated for each repeat case (figure 6.24). The general trend for each system is a steady increase in channel width (as can be seen in figure 6.23), with each system diverging from a single point at approximately 7 years, consistent with the observed trends in dissipation seen in figure 6.21. The initial increase in channel width has a shallower slope than the

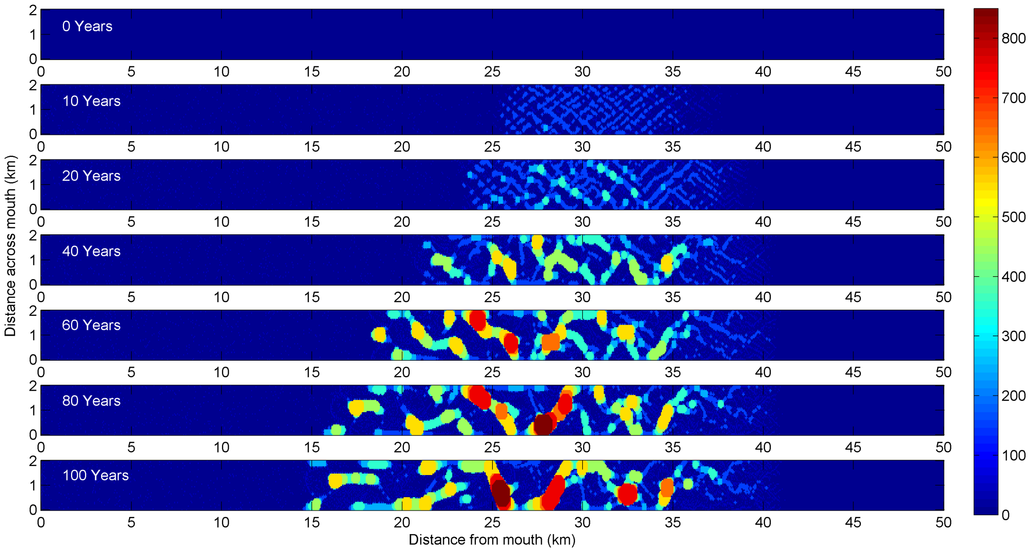

Figure 6.23 – Images of the estimated channel width (m) from repeat 1 for different instances in the 100 year simulation period. Note the circular nature of the channel width estimates which allows for varying channel width and braiding.

resulting increase after divergence (at around 10 years). This period of time is coincident with the spontaneous self-organisation of the bed into the initial brick pattern. This is also supported by the dissipation results which showed a markedly different nature of dissipation (i.e. an increase with time) during the self-organisation phase (figure 6.21).

As in the previous results the three systems can be seen to diverge in their average channel width, with the difference in width increasing between each system over time. Whether this difference continues to grow or subsequently converges with further evolution is not known from this study. However it can be expected that as the channel network fills the remainder of the model domain the average channel width will tend to become steady with time.

The final (after 100 years morphological time) difference in channel width between the three systems supports the end result of the FFT analysis in figure 6.22 which suggested that the diverging differences in dissipation between each system is due to a diverging difference in morphology. From figure 6.24 it is concluded that that the channel plan form morphology is indeed different after 100 years of evolution between the three systems. As mentioned previously the use of the channel cross-sectional area algorithm of Fagherazzi et al (1999) could be applied in the future. This would elucidate whether or not the difference in channel width between each system after 100 years is balanced by a difference in average channel depth—i.e. narrow, deep channels as opposed to wide, shallow channels.

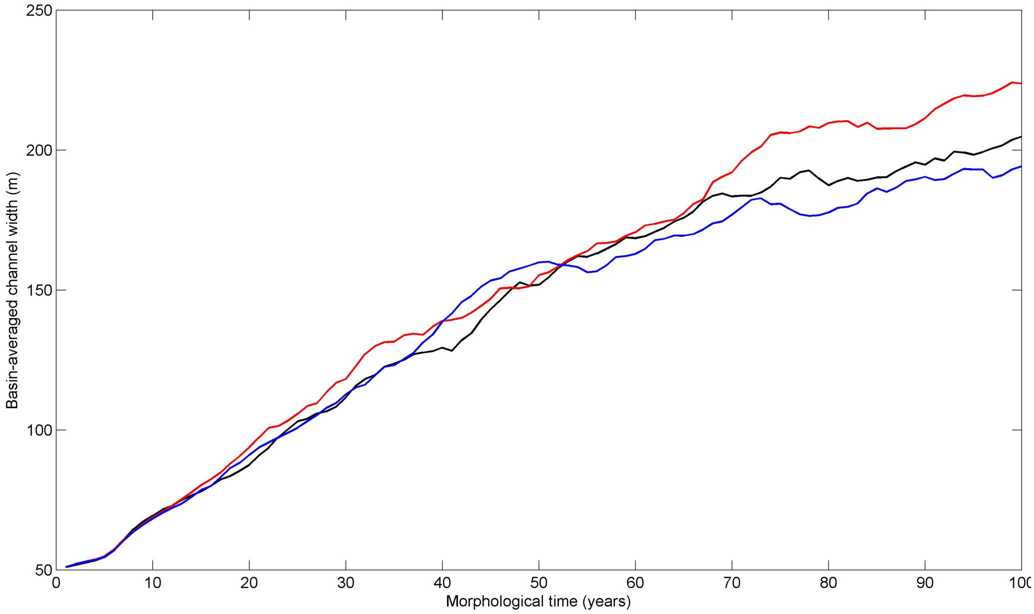

Figure 6.24 – The tide-and basin-averaged tidal channel width for repeat cases 1, 2, and 3 (black, red and blue line respectively) over the 100 year simulation period.

6.9 Summary

In this chapter the effect of an infinitesimal, random perturbation has been investigated on a deterministic morphological system in the `TELEMAC 2D` model environment. Through three separate, independent system variables (dissipation, FFT spectrum centroid and channel width) phenomena have been observed which are inherent to open, dissipative systems. From an initially flat bed and with identical tidal forcing throughout their evolution, three independent systems are seen to display the spontaneous self-organisation of a regular morphological pattern at the same point in their evolutionary history. From this point on, however, small changes in morphology between the three systems lead to significant differences after 100 years of morphological evolution, visualised through a divergence in the time-evolution of the basin-averaged dissipation rate, bed length-scales derived from FFT analysis and the estimated average channel width of the 'wet' tidal channel network.

Although it is arguable whether the addition of a stochastic threshold of motion is desirable for the purpose of morphological prediction, it is clear that, in a coupled modelling system such as `TELEMAC 2D` and `SISYPHE`, infinitesimal changes may have a significant impact on the end result. This realisation of the 'butterfly effect' of Lorenz (1963) implies that a deterministic system can display elements of chaos when a small element of probability is included, even at the lowest level. Importantly, this shows that time-evolving, non-linearly interacting morphological systems can be sensitive to very small changes in morphology—a concept that should be taken into account when interpreting the results of a morphological prediction. Although the model is, at its very core, entirely deterministic a slight change in the depth of a single point in a channel network, for example, may produce a different morphological outcome. It may be advisable, then, to conduct multiple morphological simulations with a probabilistic perturbation such as the threshold of motion (which has a physical underpinning) to receive an understanding of the general form and degrees of freedom that a particular morphological system might exhibit.

Chapter 7

Discussion

7.1 Aims of the Thesis

The main aim of this thesis was to explore the use of `TELEMAC 2D` and `SISYPHE` to model the long-term morphological evolution of tidal basins such as the Dyfi Estuary. As a depth-averaged (2DH) model, `TELEMAC 2D` is unable to simulate certain aspects of estuaries which are perceived as being important in the long term—namely the dilution of salinity by fresh water river input and its associated effect on the residual estuarine circulation. It was interesting, then, to witness a complex tidal channel system form in a highly schematised, 2DH morphological model with simplified input conditions. It is clear that certain aspects of sandy tidal basins, although complicated in appearance, are formed by relatively simple hydrodynamic processes.

There were a number of physical processes that were deliberately omitted from this study, namely the simulation of waves and suspended sediment transport. Both processes are expected to contribute significantly towards morphological development and dynamics but unfortunately their inclusion in the presented models was not possible. However, as seen in Chapter 6, infinitesimal changes in the initial conditions of a deterministic model can have significant effects on the end result. It is therefore vitally important to treat *all* modelled results with suspicion (especially from long-term simulations), regardless of how complete or complicated the physical parameterisations may be. The inclusion of waves in coupled `TELEMAC 2D+SISYPHE` runs will be possible in future releases of the `TELEMAC` distribution however, which opens up a number of avenues of research for the future.

It is important to state that the simulations described in Chapters 4 and 6 should not be used for predictive purposes—the deliberately high MF coefficients and use of a solely bed load sediment transport predictor greatly oversimplify the processes involved. Considering the divergent evolution of three models described in Chapter 6, however, the sensitivity to initial conditions which is inherent to such a complicated, process-based and time-stepping coupled model affect its use as a predictive tool. In fact, it is argued that all deterministic systems are inherently unpredictable solely because of their sensitivity to initial conditions and lack of any random elements (Kellert, 1993). Although elements of random chance may appear unpredictable, they follow set distributions of probability in both time and space, which gives them a degree of predictability. With every error, no matter how infinitesimal, the future outcome of a deterministic process will change. Great care must therefore be exercised in the interpretation of model results such as those from a deterministic coastal area morphological model. However, the *general form* of the outcome may be properly ascertained if multiple simulations are conducted.

The validation of Van Rijn's roughness prediction method in the Dyfi Estuary was highly successful given the number of omitted physical processes and known errors in model bathymetry. The success of the analysis was largely due to the use of the Swathe Sonar bathymetric data collected in the 2007 Dyfi Estuary survey. The use of this type of data should certainly be exploited in the future—even with a simple turning points algorithm over 2,700 individual bed forms were identified and measured from a single survey. One of the biggest issues with the results of Chapter 5 was the lack of bed form history effects, due to the absence of a usable parameterisation in the literature. The lack of research into dune history effects will benefit from the use of these Sonar surveys, being relatively cheap and simple to conduct (requiring only a small vessel). Surveys conducted over multiple tides will help to understand the intra-tidal development of dunes, which in turn will supply the data essential to forming a usable parameterisation for models such as `SISYPHE`. The use of a coherent bed roughness for both flow and sediment transport computation has been overlooked in past investigations. Most importantly the influence of sub-grid scale dunes on sediment transport rates through their effect on the flow computation is not a well-studied area of coastal modelling research. In the present body of work it was concluded that the feedback of dune-scale roughness (varying in both time and space) to the flow computation has a significant and varied impact on the magnitude (and even sign) of the subsequently calculated rate of sediment transport. This implies that in the medium- to long-term the k_s feedback method will have a significant effect on morphological development, in both the rate and pattern.

The so-called ‘brick pattern’ described in Chapters 4 and 6 is undoubtedly a spatially regular morphological pattern that is significant in the sense that all future morphological development is subsequent to it. The three parallel simulations described in Chapter 6 showed that even with a spatially stochastic perturbation to the sediment transport routine the pattern was consistent in form between the three repeat cases. It is unlikely that it is merely a consequence of the unstructured, finite element mesh as images in Van der Wegen (2010) show patterns of channel development similar to those that formed subsequently from the brick pattern described in this body of work (and on a similar time scale of approximately 20 years). The models of Van der Wegen were conducted in Delft 3D (albeit the 2DH implementation), which runs on a regular grid. However this does not rule out mesh dependence. A full investigation of the brick pattern would require a test of sensitivity to mesh resolution, basin geometry, bed slope and tidal period. Whatever the physical basis for the pattern, its presence in the model required a greater amount of energy to create and sustain than the flat bed which is contrary to a mechanistic, linear description of the problem.

7.2 Future work

The work described in this thesis has created the following avenues of possible future research which could be explored:

'Brick pattern' morphology

From the evidence (particular the dissipation results) presented in Chapter 6 it was concluded that the highly regular morphological pattern first described in Chapter 4 is indeed a self-organised, dissipative structure. Due to the time-stepping nature of the numerical model the initial 'brick pattern' is undoubtedly responsible for all further morphological evolution in the simulation. However, it remains unknown whether the morphological pattern is physical or a numerical artifact. The dependence on the formation of the pattern on mesh resolution and geometry as well as the tidal environment of the basin should be investigated.

Effect of waves

The planned future releases of `TELEMAC 2D` are to feature full, internal coupling with the wave module `TOMOWAC`. To feature waves in a coupled morphological model of the scope described in the present body of work full internal coupling between `TELEMAC 2D`, `SISYPHE` and `TOMOWAC` would be essential. The effect of waves will be important in models of natural, 'real-world' tidal basins, so this is an important issue that should be addressed with future research.

k_s history effects

Currently, the implemented k_s prediction and feedback method assumes that the bed forms are in equilibrium with the flow conditions at every computational time step. This is contrary to the behaviour of natural bed forms that undergo changes in geometry at a rate that is determined by the relative strength of the flow. History effects could therefore be introduced into the k_s prediction code by means of a developmental time-scale, possibly similar to that proposed by Soulsby & Whitehouse (2005). The developmental time for ripples is well documented (Baas, 1999), however a similar literature for subaqueous dunes in a tidal environment is less developed. The use of swathe sonar bathymetric surveying in this thesis could be extended to study the development of an area of dunes (e.g. at the present study side in the Dyfi Estuary) over a suitable period of time with coincident hydrodynamic measurements or modelling. It is hypothesised that the addition of history effects to the k_s prediction code will reduce the maximum calculated roughness in all areas (due to a lack of time for dunes to develop fully), while raising the minimum and average roughness as dunes will be able to remain for greater periods due to the history effect.

Advection-diffusion schemes and the MF method

The apparent incompatibility of the Advection-Diffusion (A-D) scheme for suspended sediment transport in `SISYPHE` is a practical problem that should be addressed if the MF method is to be used for research concerning bathymetric prediction in environments where suspended sediment transport is thought to be significant for morphological development (e.g. in areas with a low grain size). The CFL-type instabilities that were encountered in the work conducted for this thesis lead to the formulation of a predictor for the threshold bed evolution when the MF method and A-D scheme were combined. Although the results suggest the current A-D scheme coded into `SISYPHE` is incompatible with the MF method, it is possible that either the A-D code or the implementation of the MF method could be altered to accommodate the other. Rigorous testing is also required to determine the root cause of the instabilities.

Degrees of freedom

In Chapter 6 a model was introduced that contained an inherent, stochastic process. Through this small inclusion of probabilism, the modelled morphology was seen to behave in a dynamic manner, with all three simulations diverging from a single point in time and (in the 100 year simulation) never re-converging. This is behaviour inherent to a field of mathematical study known as chaos theory. Chaos theory embodies the concept that systems that are sensitive to initial conditions can display widely differing evolved states (the 'butterfly effect' of Lorenz, 1963). An example of a simple deterministic (and linear) system is the logistic growth model of May (1976) which determines the growth of population P with time, based on a growth rate r_g so that

$$P_{t+1} = r_g P(t)\,(1 - P_t) \tag{7.1}$$

Equation 7.1 shows increasingly dynamic behaviour as r_g increases. Iterating the model for 500 steps and varying values of r_g and $P_{t=0}$ a bifurcation diagram can be produced of the final population values for each initial condition (figure 7.1). As r_g is increased the system shows increasingly dynamic behaviour, with stable bimodal population oscillations for $3 < r_g < 3.4$. The modes of stable oscillation increase until $r_g \approx 3.6$ where the system becomes chaotic. However within this 'cloud' of seemingly random points (each representing the final population after 500 iterations) there are areas of increased probability where points can be seen to group in curve-like paths.

To create figure 7.1 over 800,000 runs of 500 iterations were done to determine the final system population. In Chapter 6, three simulations were run that showed different resultant values for three system state indicators. It would take a vast amount of computational effort to perform, but it would technically be possible to investigate the true number of degrees of freedom in the modelled tidal basin by iterating the 100 year morphological simulation for varying initial conditions. This may be feasible with the use of high performance computing—machines with over 100,000 processors that can be used in parallel.

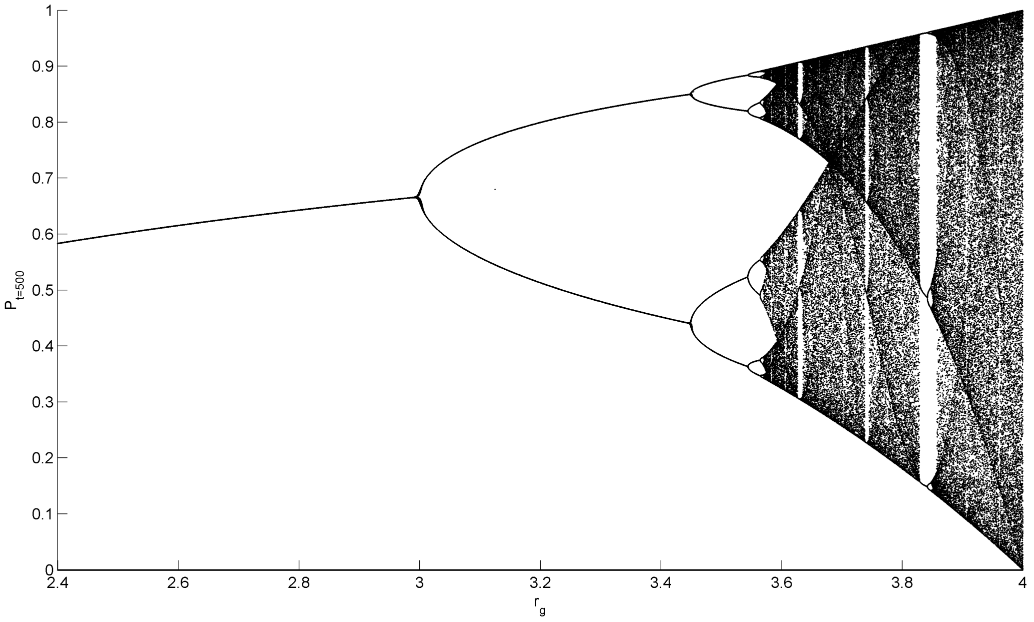

Figure 7.1 – Bifurcation diagram of values of P after 500 iterations from equation 7.1 for varying r_g and $P_{t=0}$

Chapter 8

Final conclusions

8.1 Conclusions from Chapters 3 and 4

Long-term morphological modelling in `TELEMAC 2D` and `SISYPHE` with the MF method

In chapter 4 a coupled morphological model of a schematised, long and narrow tidal basin and the results of 100 years of morphological evolution was described. This was a test simulation to asses the compatibility of `TELEMAC 2D` and `SISYPHE` with the Morphological Factor (MF) method of bed-update speed up. It is concluded that `TELEMAC 2D` and `SISYPHE` are stable when using relatively high values of the MF coefficient using an equilibrium morphological model.

Suspended transport and instabilities

The use of an Advection-Diffusion (A-D) scheme for suspended sediment transport was found to introduce numerical instabilities that render the MF factor approach unusable in its current implementation. A stability criterion based on the CFL number and the suspended sediment transport equation used within `SISYPHE` was derived and initial findings show it to successfully delineate stable and unstable runs.

Evidence of spontaneous self-organisation

With a single tidal harmonic (M_2) and additional no time-fluctuating energy inputs (such as wave events or river input), a highly ordered, symmetrical and robust morphological pattern was found to spontaneously form from a flat bed within 10–20 years of morphological time. Due to the simplicity and consistent input of energy to the model it is concluded that the so-called ‘brick pattern’ is a spontaneous, self-organised morphological pattern.

8.2 Conclusions from Chapter 5

Validating bed roughness prediction in the Dyfi Estuary

A set of formulae to predict the hydraulic roughness of the bed (Van Rijn, 2007) was implemented in `SISYPHE` and at regular intervals the roughness due to dunes was passed back to `TELEMAC 2D` for use in the flow computation of the subsequent time step. This method was applied in a model of the Dyfi Estuary where a swathe sonar bathymetric survey had been conducted in 2007. Simulating the hydrodynamic conditions of the survey period, the calculated total roughness of the bed was compared to the height of bed forms (dunes) extracted from the sonar bathymetry data set. Good agreement was found between simulation results and the data along two profiles once a suitable scaling factor was taken into account. It was concluded that the roughness formulation did well to describe the magnitude and spatial behaviour of bed roughness in the Dyfi, even though significant assumptions and omissions were present in the model.

Effect of roughness feedback on hydrodynamics and sediment transport

Using a test case simulation of the Dyfi Estuary with an M_2 tide, the effect of bed roughness feedback to `TELEMAC 2D` was investigated. The inclusion of dune roughness was seen to slow current speeds while increasing the total bed shear stress through an enhanced bed drag coefficient. Compared to a control case with bed roughness calculated but not fed back to `TELEMAC 2D`, the resulting sediment transport rate (using a total load transport formula) was seen to increase in some areas while decrease in others. It was concluded that the physically important inclusion of time-varying dune roughness into the `TELEMAC 2D` flow computation can have a significant, yet varied, effect on the magnitude of sediment transport and thus morphological evolution.

8.3 Conclusions from Chapter 6

Stochastic implementation of θ_{cr}

The addition of a stochastic element to the threshold of sediment motion θ_{cr} was shown to introduce a positive bias to the calculated rate of bed load sediment transport. Due to the non-linear nature of the predictive formula used (Van Rijn, 1984a) and the choice of probability distribution for the stochastic perturbation of θ_{cr} (Gaussian distribution of ±15% at two standard deviations) the bias was found to be between +2–3% for most flow situations. However, due to the arrangement of θ_{cr} in the formula the bias was seen to rise significantly at low flow states which are near the threshold of motion, with a maximum positive bias of +12% near threshold.

Morphological evolution

Three identical, simultaneous morphological simulations were conducted using the stochastic implementation of θ_{cr} in the bed load transport formula. In each case the morphological evolution was seen to repeat that seen in chapter 6. All three cases exhibited the self-organised brick pattern. From this it is concluded that the brick pattern is inherent to the system and robust enough to be insensitive to initial fluctuations. The morphological evolution over a 100 year period was described, with each repeat case showing similar, but not identical, resulting morphologies.

Dissipation

The basin- and yearly-averaged dissipation rate per unit area of bed was generally found to be reduced over 100 years of morphological time in a schematised, rectangular tidal basin. Over three repeat cases with a randomly perturbed θ_{cr} (over both time and space) in the bed load sediment transport formula the dissipation rate was found to differ over time, although all cases displayed the same general trend of dissipation reduction. During a period of spontaneous self-organisation of morphology from a flat bed, the dissipation rate in all three cases was seen to increase. However, the final dissipation rate calculated for each repeat case differed, providing evidence for divergent evolution. It is concluded that the tidal basin model can be classified as an open, dissipative system and the ‘brick pattern’ morphology classified as a dissipative structure.

Bed perturbation length scales

A 2D-FFT analysis was performed on a section of bed morphology in the three repeat cases. The centre of mass (centroid) of the absolute amplitude of the FFT wavelength spectrum was calculated for each time-instance. In each repeat case the x and y centroid components were shown to increase in scale over the 100 year morphological simulation period. Although the FFT analysis was found to be unsuitable to measure the scale of bed features, it was concluded that the general along- and across basin bed perturbation length scales increase over time as the system morphology evolved. The three repeat cases showed different FFT wavelength spectra at 100 years of morphological time, providing evidence for divergent evolution.

Channel width analysis

The method of Fagherazzi et al (1999) for the estimation of channel width within a channel network using image processing techniques was implemented. For each of the three repeats the basin- and yearly-averaged channel width was seen to increase steadily. As with the dissipation and perturbation length scale analyses, the basin-averaged channel with was seen to differ between the three repeat cases at the end of the 100 year morphological simulation, providing supporting evidence for divergent evolution.

Divergent evolution

In the initial 20 years of morphological time which coincided with the spontaneous evolution of the self-organised brick pattern all three repeat cases showed almost identical rates of dissipation and magnitude of the estimated channel width. As soon as the initial pattern begins to form into channel structures the traces of dissipation and channel width over time are seen to diverge from a common point and never re-converge for any of the three repeat cases over a 100 year simulation period. It was concluded that the brick pattern is inherent to and dynamically identical in all three repeat cases. However the inclusion of infinitesimal differences between the three cases through the stochastic implementation of θ_{cr} produced a phenomenon similar to the 'butterfly effect' of Lorenz (1967). It is concluded that infinitesimal, stochastic perturbations to a deterministic, time-evolving coupled morphological model can produce divergent evolution.

Chapter 9

References

Baas, C.W. (2002). Chaos, fractals and self-organization in coastal geomorphology: simulating dune landscapes in vegetated environments. *Geomorphology* **48**, 309–328

Baas, J.H. (1994). A flume study on the development and equilibrium morphology of small-scale bedforms in very fine sand. *Sedimentology* **41**, 185–209

Baas, J. (1999). An empirical model for the development and equilibrium morphology of current ripples in fine sand. *Sedimentology* **46**, 123–138

Bagnold, R.A. (1946). Motion of waves in shallow water: Interaction of waves and sand bottoms. *Proceedings of the Royal Society of London* **A197**, 1–15

Bagnold, R.A. (1956). The flow of cohesionless grains in fluids. *Philosophical Transactions of the Royal Society, London* **964**, **vol.249**, 235–297

Bijker, E.W. (1968). Mechanics of sediment transport by the combination of waves and current. In: *Design and Reliability of Coastal Structures, 23rd International Conference on Coastal Engineering*, 147–173

Box, G.E.P. & Muller, M.E. (1958). A note on the generation of random normal deviates. *Annals of Mathematical Statistics* **29**, 610–611

Briggs, W.L. & Henson, V.E. (1995). The DFT: An owner's manual for the Discrete Fourier Transform. *Society for Industrial and Applied Mathematics, Philadelphia*

Brown, J.M. (2007). Coastal area modelling: Sand transport and morphological change. *Unpublished PhD thesis, University of Wales, Bangor*

Brown, J.M. & Davies, A.G. (2007). Field measurement and modelling of scour pit dynamics in a sandy estuary. Coastal Sediments 07: proceedings of the 6th International Symposium on Coastal Engineering and Science of Coastal Sediment Processes 2007, New Orleans, *American Society of Civil Engineers*, 1609-1622

Brown, J.M. & Davies, A.G. (2009). Methods for medium-term prediction of the net sediment transport by waves and currents in complex coastal regions. *Continental Shelf Research* **29**, 1502-1514

Brown, J.M. & Davies, A.G. (2010). Flood/ebb tidal asymmetry in a shallow sandy estuary and the impact on net sand transport. *Geomorphology* **114**, 431–439

Cayocca, F. (2001). Long-term morphological modeling of a tidal inlet: the Arcachon Basin, France. *Coastal Engineering* **42**, 115-142

Champeney, D.C. (1973). Fourier transforms and their physical applications. *Academic Press, London*

Cheng, N.S., Law, A.W.K. & Lim, S.Y. (2003). Probability distribution of bed particle instability. *Advances in Water Resources* **26**, 427–433

Coeveld, E.M., Hibma, A. & Stive, M.J.F. (2003). Feedback mechanisms in channel-shoal formation. *Coastal Sediments, Clearwater Beach, Florida, U.S.A.*

Cooley, J.W. & Tukey, J.W. (1965). An algorithm for the machine computation of the complex Fourier series. *Mathematics of Computation* **19**, 297–301

Courant, R., Friedrichs, K. & Lewy, H. (1967). On the partial difference equations of mathematical physics. *IBM Journal* **11**, 215–234

De Vriend, H.J., Capobianco, M., Chesher, T., De Swart, H.E., Latteux, B. & Stive, M.J.F. (1993). Approaches to long-term modelling of coastal morphology: a review. *Coastal Engineering* **21**, 225–269

Dollman, J. (2008). Sediment transport pathways and dispersal patterns in the Dyfi estuary, Wales. *Unpublished MSc thesis, University of Bangor, U.K.*

Dronkers, J. (1986). Tidal asymmetry and estuarine morphology. *Journal of Sea Research* **20**, 117–131

Dronkers, J. (2005). Dynamics of Coastal Systems. *World Scientific, Hackensack*

Dyer, K.R. (1986). Coastal and estuarine sediment dynamics. *Wiley-Interscience, Chichester, New York*

Einstein, H., & El-Samni, E.A. (1949). Hydrodynamic forces on a rough wall. *Reviews of Modern Physics* **21**, 520-524

Fagherazzi, S., Bortoluzzi, A., Dietrich, W.E., Adami, A., Lanzoni, S., Marani, M. & Rinaldo, A. (1999). Automatic network extraction and preliminary scaling features from digital terrain maps. *Water Resources Research* **35**, 3891–3904

Fortunato, A.B. & Oliveira, A. (2005). Influence of intertidal flats on tidal asymmetry. *Journal of Coastal Research* **21**, 1062–1067

Friedrichs, C.T. & Aubrey, D.G. (1996). Uniform bottom shear stress and equilibrium hypsometry of intertidal flats. In: Pattiaratchi, C. (Ed.), Mixing Processes in Estuaries and Coastal Seas. Coastal and Estuarine Studies Series. *American Geophysical Union, Washington, D.C*, 405-429

Galland, J.C., Goutal, N. & Hervouet, J.M. (1991). TELEMAC: A new numerical model for solving shallow water equations. *Advances in Water Resources* **14**, 138–148

Haynes, J. & Dobson, M. (1969). Physiography, Foraminifera and sedimentation in the Dyfi Estuary. *Geological Journal* **6**, 217–256

Hervouet, J.-M. & Bates, P. (2000). Special Issue: The TELEMAC Modelling System. *Hydrological Processes* **14**(13), 2207–2364

Hervouet, J.-M. (2007). Hydrodynamics of free surface flows. *Wiley, Chichester, UK*

HIBMA, A., DE VRIEND, H.J. & STIVE, M.J.F. (2003). Numerical modelling of shoal pattern formation in well-mixed elongated estuaries. *Estuarine, Coastal and Shelf Science* **57**, 981–991

HIBMA, A., SCHUTTELLAARS, H.M. & DE VRIEND, H.J. (2004a). Initial formation and longterm evolution of channel-shoal patterns. *Continental Shelf Research* **24**, 1637–1650

HIBMA, A., STIVE, M.J.F. & WANG, Z.B. (2004b). Estuarine morphodynamics. *Coastal Engineering* **51**, 765–778

HUGGETT, R. (2007). A history of the systems approach in geomorphology. *Géomorpologie: relief, processus, environnement* **2**, 145–158

JAGO, C.F. (1980). Contemporary accumulation of marine sand in a macrotidal estuary, Southwest Wales. *Sedimentary Geology* **26**, 21–49

JONES, A.D. (1969). Aspects of comparative air photo-interpretation in the Dyfi Estuary. *The Photogrammetric Record* **6**, 291–305

KELLERT, S.H. (1993). In the Wake of Chaos: Unpredictable Order in Dynamical Systems. *University of Chicago Press*

KOCH F.G. & FLOKSTRA C. (1981). Bed level computations for curved alluvial channels. *19th Congress of the International Association for Hydraulic Research, New Delhi India*

LATTEUX, B. (1995). Techniques for long-term morphological simulation under tidal action. *Marine Geology* **126**, 129-141.

LESSER, G.R., DE VROEG, J.H., ROELVINK, J.A., DE GERLONI, M. & ARDONE, V. (2003). Modelling the morphological impact of submerged offshore Breakwaters. *Proceedings of Coastal Sediments 2003, Clearwater Beach, Florida, USA*

LORENZ, E.N. (1963). Deterministic nonperiodic flow. *Journal of the Atmospheric Sciences* **20**, 130–141

MARCIANO, R., WANG, Z.B., HIBMA, A., DE VRIEND, H.J. & DEFINA, A. (2005). Modelling of channel patterns in short tidal basins. *Journal of Geophysical Research* **110**, F01001, doi:10.1029/2003JF000092

MAY, R.M. (1976). Simple mathematical models with very complicated dynamics. *Nature* **261**, 459–475

MEADE, R.H. (1972). Transport and deposition of sediments in estuaries. *Geological Society of America*, Memoir **133**, 91–120

MEYER-PETER, E. & MÜLLER, R. (1948). Formulas for bed-load transport. *Rep. 2nd. Meet. Int. Assoc. Hydraul. Struct. Res.*, Stockholm, 39–64

NATURE CONSERVANCY COUNCIL (1983). The Wildlife of the Dyfi Estuary.

NIELSEN, P. (1992). Coastal bottom boundary layers and sediment transport. *World Scientific, Singapore, Advanced Series on Ocean Engineering*

PHILLIPS, J.D. (1999). Divergence, convergence and self-organisation in landscapes. *Annals of the Association of American Geographers* **89**, 466–488

PHILLIPS, J.D. (2007). The perfect landscape. *Geomorphology* **84**, 159–169

PRANDLE, D. (2006). Dynamical controls on estuarine bathymetry: Assessment against U.K. database. *Estuarine, Coastal and Shelf Science* **68**, 282–288

PRESS, W.H., TEUKOLSKY, S.A., VETTERLING, W.T. & FLANNERY, B.P. (2007). Numerical recipes third edition. *Cambridge University Press*

PRIGOGINE, I. & STENGERS, I. (1984). Order out of Chaos: Man's new dialogue with nature. *Flamingo, Collins Publishing Group, London UK*

PRITCHARD, D.W. (1964). What is an estuary: physical viewpoint, pp. 3-5 In: *G. H. Lauf (ed.) Estuaries. American Association for the Advancement of Science, Washington, D.C.*

PUGH, D.T. (1987). Tides, surges and mean sea-level: a handbook for engineers and scientists. *Wiley, Chichester, UK*

RANASINGHE, R., SWINKELS, C., LUIJENDIJK, A., ROELVINK, D., BOSBOOM, J., STIVE, M. & WALSTRA, D. (2011). Morphodynamic upscaling with the MORFAC approach: Dependencies and sensitivities. *Coastal Engineering* **58**, 806–811

Robins, P.E. (2008a). Present and Future Flooding Scenarios in the Dyfi Estuary, Wales, U.K. *Centre for Applied Marine Science, Bangor University, Interim Report Volume* **1**

Robins, P.E. (2008b). Present and Future Flooding Scenarios in the Dyfi Estuary, Wales, U.K. *Centre for Applied Marine Science, Bangor University, Interim Report Volume* **2**

Robins, P.E. & Davies, A.G. (2010). Morphological controls in sandy estuaries: the influence of tidal flats and bathymetry on sediment transport. *Ocean Dynamics* **60**, 503–517

Robins, P.E., Davies, A.G. & Jones, R. (2011). Application of a coastal model to simulate present and future inundation and aid coastal management. *Journal of Coastal Conservation* **15**, 1–14

Roelvink, J.A. (2006). Coastal morphodynamic evolution techniques. *Coastal Engineering* **53**, 277–287

Roelvink, J.A., Walstra, D.J.R. & Chen, Z. (1994). Morphological modelling of Keta lagoon case. *Proceedings of the 24th International Conference on Coastal Engineering. ASCE, Kobe, Japan*

Russell, R.J. (1964). Origins of Estuaries, In: *Estuaries. American Association for the Advancement of Science, Washington, D.C.*

Schuttellaars, H.M. & De Swart, H.E. (1999). Initial formation of channels and shoals in a short tidal embayment. *Journal of Fluid Mechanics* **386**, 15–42

Seminara, G. & Tubino, M. (1998). On the formation of estuarine free bars. In: *In J. Dronkers, & M. Scheffers (Eds.), Physics of estuaries and coastal seas, Rotterdam: Balkema.* 345-353)

Seminara, G. & Tubino, M. (2001). Sand bars in tidal channels. Part one: free bars. *Journal of Fluid Mechanics* 440, 49–74

Shi, Z. (1991). Tidal bedding and tidal cyclicities within the intertidal sediments of a microtidal estuary, Dyfi River Estuary, West Wales, U.K. *Sedimentary Geology* **73**, 43–58

Shi, Z. (1993). Recent saltmarsh accretion and sea level fluctuations in the Dyfi Estuary, central Cardigan Bay, Wales, U.K. *Geo-Marine Letters* **13**, 182–188

Shi, Z. & Lamb, H.F. (1991). Post-glacial sedimentary evolution of a microtidal estuary, Dyfi Estuary, west Wales, U.K. *Sedimentary Geology* **73**, 227–246

Shi, Z., Lamb, H.F. & Collin, L. (1995). Geomorphic change of saltmarsh tidal creek networks in the Dyfi estuary, Wales. *Marine Geology* **128**, 73–83

Shields, A. (1936). Anwendung der ähnlichkeits-mechanik und der turbulenzforschung auf die geschiebebewegung. *Preussische Versuchsanstalt für Wasserbau und Schiffbau* vol. **26**, *Berlin*

Sleath, J.F.A (1984). Sea bed mechanics. *Wiley-Interscience, New York, USA*

Soulsby, R.L (1997). Dynamics of marine sands. *Thomas Telford, London*

Soulsby, R.L. & Whitehouse, R.J.S. (2005). Prediction of Ripple Properties in Shelf Seas, Mark 1 Predictor. *Technical Report TR150. HR Wallingford Ltd., U.K.*

Speer, P.E. & Aubrey, D.G. (1985). A study of non-linear tidal propagation in shallow inlet/estuarine systems. Part II: theory. *Estuarine Coastal and Shelf Science* **21**, 207–224

Van der Wegen, M. (2010). Modelling morphodynamic evolution in alluvial estuaries. *CRC Press / Balkema*

Van der Wegen, M. & Roelvink, J.A. (2008). Long-term morphodynamic evolution of a tidal embayment using a two-dimensional, process-based model. *Journal of Geophysical Research* **113**, C03016

Van der Wegen, M., Wang, Z.B., Savenije, H.H.G. & Roelvink, J.A. (2008). Long-term morphodynamic evolution and evergy dissipation in a coastal plain, tidal embayment. *Journal of Geophysical Research* **113**, F03001

Van Rijn, L.C (1984a). Sediment transport: Part I: bed load transport. *J. Hydraul. Div., Proc. ASCE* **110** (HY10), 1431–1456

Van Rijn, L.C. (1984b). Sediment transport: Part 2: Bedforms and alluvial roughness. *J. Hydraul. Div., Proc.* ASCE **110**, 1733–1754

Van Rijn, L.C. (1993). Principles of sediment transport in rivers, estuaries, and coastal seas. *Aqua Publications, Blokzijl, The Netherlands*

Van Rijn, L.C. (2007). Unified view of sediment transport by currents and waves. I: Initiation of motion, bed roughness and bed-load transport. *Journal of Hydraulic Engineering* **133**, 649–667

Van Rijn, L.C. & Havinga, F.J. (1995). Transport of fine sands by currents and waves. *Journal of Waterway, Port, Coastal and Ocean Engineering* **121**, 123-133

Van Rijn, L.C., Walstra, D.J.R., Grasmeijer, B., Sutherland, J., Pan, S. & Sierra, J.P. (2003). The predictability of cross-shore bed evolution of sandy beaches at the time scale of storms and seasons using process-based profile models. *Coastal Engineering* **47**, 295–327

Van Veen, J., Van der Speck, A.J.F., Stive, M.J.F. & Zitman, T. (2005). Ebb and flood channel systems in the Netherlands tidal waters. *Journal of Coastal Research* **21**, 1107–1120

Villaret, C., Hervouet, J.M., Huybrechts, N., Van, L.A. & Davies, A.G. (2009). Effect of bed friction on morphodynamic modelling: Application to the central part of the Gironde estuary. *Proceedings of River, Coastal and Estuarine Morphodynamics 2009, Santa Fe City, Argentina*, 899–905

Villaret, C., Huybrechts, N., Davies, A.G. & Way, O. (2011). Effect of bed roughness prediction on morphodynamic modelling : Application to the Dee estuary (U.K.) and to the Gironde estuary (France). *34th IAHR, Brisbane, Australia*

Von Bertalanffy, L. (1950). The theory of open systems in physics and biology. *Science* **111**, 23–29

Webster, F. (1929). The River Dee reclamations and the effect upon navigation. *Transactions of the Liverpool Engineering Society*, 63–100

Wilks, P.J. (1979). Mid-Holocene sea-level and sedimentation interactions in the Dovey Estuary area, Wales. *Palaeogeography, Palaeoclimatology, Palaeoecology* **26**, 17–36

Yalin, M.S. (1977). Mechanics of sediment transport, 2nd edition. *Pergamon Press, Oxford, UK*

Yang, C.T. (1987). Energy dissipation rate approach in river mechanics Sediment Transport in Gravel-Bed Rivers. *John Wiley & Sons, New York*, 735–766

Yang, C.T. & Song, C.S. (1979). Theory of minimum rate of energy dissipation. *Journal of the Hydraulics Division, ASCE* **105**, 769–784

Xu, J.P. (2004). Observations of plan-view sand ripple behaviour and spectral wave climate on the inner shelf of San Pedro Bay, California. *Continental Shelf Research* **25**, 373–396

Zyserman , J.A. & Fredsøe, J., (1994). Data analysis of bed concentration of suspended sediment. *Journal of Hydraulic Engineering* **120**, 1021–1042

APPENDIX I

The following is an example of a boundary condition ('conlim') file from the Dyfi Estuary model described in Chapter 3. The final column (B) contains the corresponding boundary point number (consecutively numbered anti-clockwise from the bottom-left hand corner of the mesh) for each mesh node (column N) lying on the domain boundary. The boundary conditions for free surface (z_s), velocity components (U and V) and bed evolution (z_b) are identified by an integer number where 5 = prescribed value, 4 = free value and 2 = solid boundary (no flux, no slip). Starting anti-clockwise from the bottom-left hand corner of the mesh, the outer (sea-ward) boundary is met, where the boundary condition is set to have a prescribed free surface level (value corresponding to the tidal elevation calculated by `BORD`) and free flux of fluid across the boundary. The bed level condition is also set to 'free', which allows the bed level on the boundary node based on a free sediment flux across the boundary (calculated by sediment flux gradients). The domain solid boundary begins at boundary number 8 which continues until it is interrupted by the liquid boundaries corresponding to the Rivers Leri and Dyfi. At boundary number 1630, for example, the River Dyfi boundary begins. Here the free surface is set to 'free', being calculated by the prescribed U and V fluxes (value set in the steering file) and the gradient in free surface across the boundary. The bed evolution condition is also set to 'free'. The solid boundary continues anti-clockwise around the domain until it meets the northern extent of the sea-ward open boundary at point number 2644. Critically, the 'boundary' is defined as the line drawn between two boundary nodes. Liquid boundaries are of higher order than solid boundaries, so the line between a liquid and solid boundary point exists as a liquid boundary. The entries in columns 4–7 and 9–11 can be used to prescribe values to each boundary node if the condition it set to 5. They are not used in the present body of work as values are either considered 'free' or prescribed in either `BORD` (in the case of tidal free surface elevation) or in the steering file (in the case of river flows).

Example boundary conditions file for the Dyfi Estuary model grid

z_f	U	V					z_b				N	B
5	4	4	0.000	0.000	0.000	0.000	4	0.000	0.000	0.000	16	1
5	4	4	0.000	0.000	0.000	0.000	4	0.000	0.000	0.000	39	2
5	4	4	0.000	0.000	0.000	0.000	4	0.000	0.000	0.000	89	3
5	4	4	0.000	0.000	0.000	0.000	4	0.000	0.000	0.000	158	4
5	4	4	0.000	0.000	0.000	0.000	4	0.000	0.000	0.000	249	5
5	4	4	0.000	0.000	0.000	0.000	4	0.000	0.000	0.000	392	6
5	4	4	0.000	0.000	0.000	0.000	4	0.000	0.000	0.000	627	7
2	2	2	0.000	0.000	0.000	0.000	2	0.000	0.000	0.000	953	8
2	2	2	0.000	0.000	0.000	0.000	2	0.000	0.000	0.000	1355	9
2	2	2	0.000	0.000	0.000	0.000	2	0.000	0.000	0.000	3879	10
⋮	⋮	⋮	⋮	⋮	⋮	⋮	⋮	⋮	⋮	⋮	⋮	⋮
2	2	2	0.000	0.000	0.000	0.000	2	0.000	0.000	0.000	90766	1627
2	2	2	0.000	0.000	0.000	0.000	2	0.000	0.000	0.000	90765	1628
2	2	2	0.000	0.000	0.000	0.000	4	0.000	0.000	0.000	90284	1629
4	5	5	0.000	0.000	0.000	0.000	4	0.000	0.000	0.000	89801	1630
4	5	5	0.000	0.000	0.000	0.000	4	0.000	0.000	0.000	89316	1631
4	5	5	0.000	0.000	0.000	0.000	4	0.000	0.000	0.000	88829	1632
2	2	2	0.000	0.000	0.000	0.000	4	0.000	0.000	0.000	88340	1633
2	2	2	0.000	0.000	0.000	0.000	2	0.000	0.000	0.000	87967	1634
⋮	⋮	⋮	⋮	⋮	⋮	⋮	⋮	⋮	⋮	⋮	⋮	⋮
2	2	2	0.000	0.000	0.000	0.000	2	0.000	0.000	0.000	554	2641
2	2	2	0.000	0.000	0.000	0.000	2	0.000	0.000	0.000	491	2642
2	2	2	0.000	0.000	0.000	0.000	2	0.000	0.000	0.000	423	2643
5	4	4	0.000	0.000	0.000	0.000	4	0.000	0.000	0.000	353	2644
5	4	4	0.000	0.000	0.000	0.000	4	0.000	0.000	0.000	230	2645
5	4	4	0.000	0.000	0.000	0.000	4	0.000	0.000	0.000	142	2646
5	4	4	0.000	0.000	0.000	0.000	4	0.000	0.000	0.000	79	2647
5	4	4	0.000	0.000	0.000	0.000	4	0.000	0.000	0.000	32	2648
5	4	4	0.000	0.000	0.000	0.000	4	0.000	0.000	0.000	1	2649
5	4	4	0.000	0.000	0.000	0.000	4	0.000	0.000	0.000	2	2650
5	4	4	0.000	0.000	0.000	0.000	4	0.000	0.000	0.000	3	2651
5	4	4	0.000	0.000	0.000	0.000	4	0.000	0.000	0.000	4	2652

APPENDIX II

BOundarY COndiTions for Telemac (`BOYCOTT`) is a program written in the `Matlab` code environment to provide a means of applying boundary conditions by means of a simple graphic user interface (GUI) to a finite element mesh constructed in `BlueKenue`. This was necessary as at the time the present body of work was conducted there was no simple, open source program to assign boundary conditions to a mesh and there was no built-in function within `BlueKenue`.

The method is entirely implicit—i.e. the mesh produced in `BlueKenue` must adhere to certain stringent quality controls if `BOYCOTT` is to operate properly. This is mainly due to the formation of the array `IPOBO` in the formatted mesh file. `IPOBO` contains the node 'type' of every node in the domain. A value of 1 is given to boundary nodes and a value of 0 is given to interior nodes. However, `BlueKenue` does not necessarily enforce this rule and can assign any integer number to the `IPOBO` array. The boundary tracing routine requires this list of boundary points to be correct—any break in the boundary results in the tracing routine to crash. A fully explicit version of BOYCOTT is planned for the future which will not require a correct `IPOBO` array from `BlueKenue`.

The program also requires the functions `telheadr` and `telstepr`, written by T. Benson at Hydraulics Research Wallingford, U.K. The functions are used to read in a `SELAFIN` format mesh file into Matlab.

The program proceeds as follows. Upon initialisation the user is prompted to input the name of the mesh file to which boundary conditions are to be assigned. The program then identifies boundary nodes (using `IPOBO`) and then proceeds to trace around the boundary points anticlockwise from the bottom-left-hand node. This is accomplished by the use of the connectivity array `IKLE` which contains the node vertices of each mesh element. Once the boundary has been traced to the initial origin, the code searches for any unused boundary nodes, corresponding to any islands present in the domain.

These are included by repeating the tracing algorithm on the left-over points. If there are any left over nodes after one island is connected then the process is repeated until all points in `IPOBO` are present in the ordered boundary points array.

The user is then asked to input the number of liquid boundaries and to enter the start and end node number of each boundary in turn using a simple GUI (in fact a `Matlab` figure window that can be manipulated on screen). The code assumes that all non-liquid boundaries are to be solid boundaries. The chosen boundary line is then highlighted (figure III-A) to check for correct boundary placement. This process continues until all liquid boundaries have been set. At each instance, the user is asked to input the boundary condition for each liquid boundary. Once the placement process is completed the program creates a correctly formatted ‘conlim’ file, assuming the condition `2-2-2-2` for every solid boundary point (figure III-B)

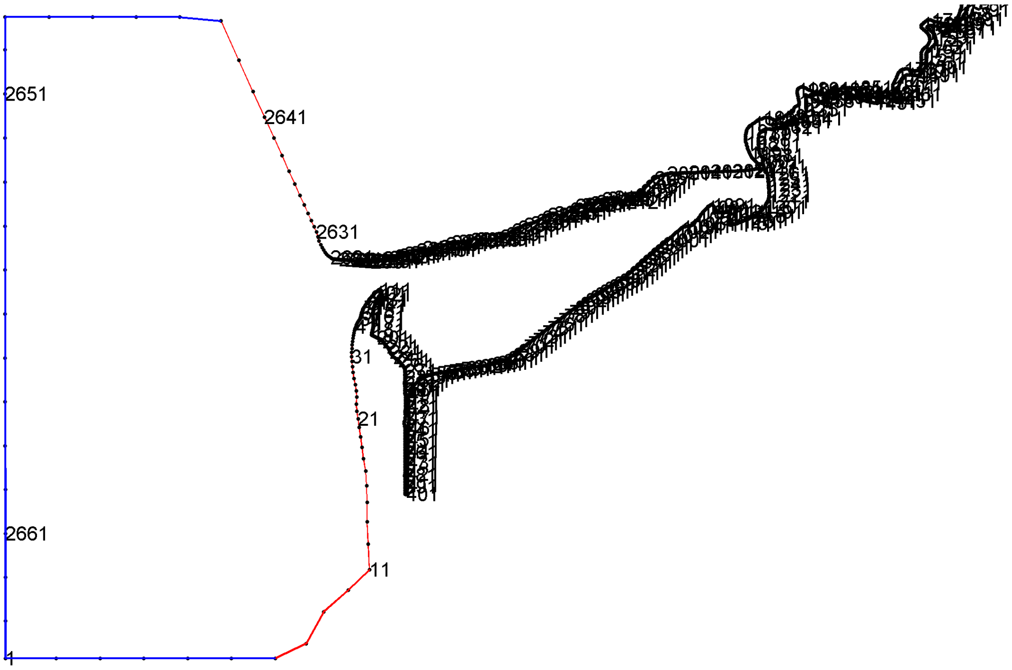

Figure III-A – Screen-shot of the `BOYCOTT` interface during boundary assignment. The numbers correspond to boundary point numbers (labeled every 10 points). The red line represents the default, closed boundary condition and the blue line represents a liquid boundary chosen by the user.

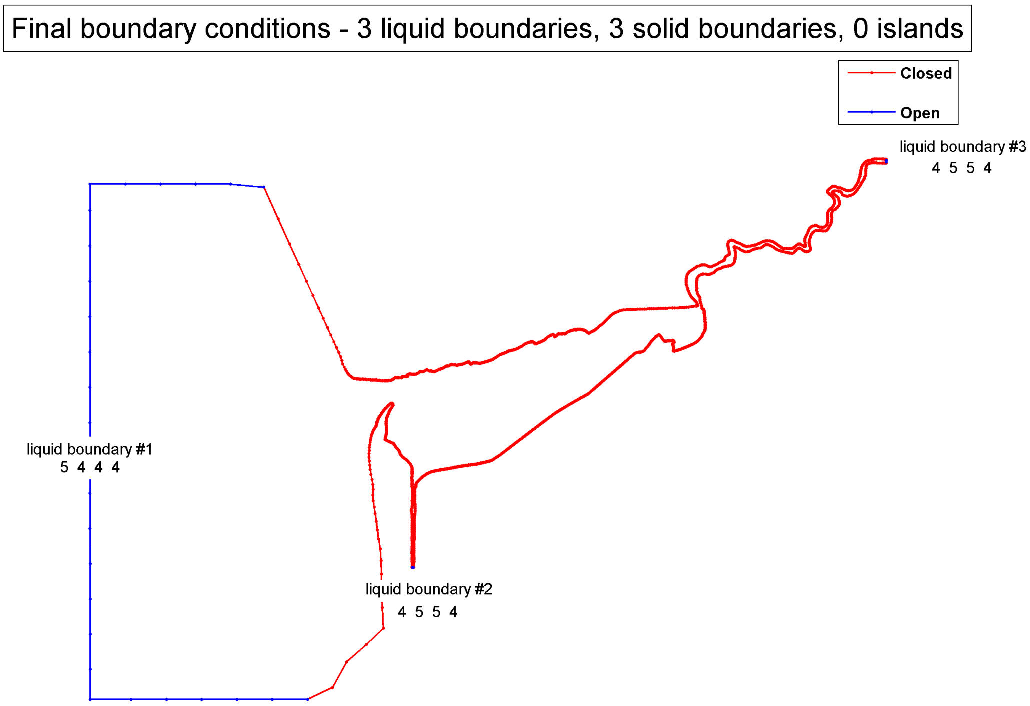

Figure III-B – Screen-shot of the `BOYCOTT` interface at the end of boundary assignment. Solid boundaries are highlighted in red and liquid boundaries in blue, with their associated boundary conditions and liquid boundary numbers.

APPENDIX III

The following are examples of a `TELEMAC 2D` and a `SISYPHE` steering (‘cas’) file. The keywords (the commands read by `TELEMAC 2D` and `SISYPHE` upon initialization) and input choices are in a `Type writer` font (keywords are in `CAPS`. *Italicised* comments are included for explanation of specific keywords. It must be noted that not all of the options available in `TELEMAC 2D` and `SISYPHE` are listed in the following steering files as not all of the options were used in the body of work presented in this thesis. Any keyword that is not listed subsequently can therefore be assumed to be set to the default value (or choice) in both `TELEMAC 2D` and `SISYPHE`.

Example steering file for `TELEMAC 2D`

`RELEASE = V5P9`—*Version of code to be run*
`PARALLEL PROCESSORS = 8`—*Number of parallel processors to be implemented*
`STEERING FILE = telemac.cas`—*Name of TELEMAC 2D ‘cas’ file*
`FORTRAN FILE = ks_feedback.f`—*Name of user FORTRAN file*
`BOUNDARY CONDITIONS FILE = dyfi.conlim`—*Name of ‘conlim’ file*
`GEOMETRY FILE = dyfi.geo`—*Name of mesh file*
`COMPUTATION CONTINUED = YES`—*Allows continuation from a previous run*
`PREVIOUS COMPUTATION FILE = ks_spinup.r2d`—*Name of result file to continue from*
`RESULTS FILE = ks_test.r2d`—*Name of result file (for this run)*
`INITIAL TIME SET TO ZERO = NO`—*Can be used to reset time counter*
`COUPLING WITH = ’INTER-SISYPHE’`—*Internal coupling with SISYPHE*
`COUPLING PERIOD = 1`—*Period to couple with SISYPHE (1 = every time step)*
`SISYPHE STEERING FILE = sisyphe.cas`—*Name of SISYPHE ‘cas’ file*
`EQUATIONS = ‘SAINT-VENANT EF’`—*Type of hydrodynamic equations*
`VARIABLES FOR GRAPHIC PRINTOUTS = ‘U,V,H,S,B,M,W’`—*Variables to be saved in the results file (choices below)*

U	*Velocity along the x-axis*	(ms^{-1})
V	*Velocity alng the y-axis*	(ms^{-1})
H	*Water depth*	*(m)*
S	*Free surface elevation*	z_s *(m)*
B	*Bottom elevation*	z_b *(m)*
M	*Scalar velocity*	(ms^{-1})
W	*Bed roughness*	k_s *(m)*

`TIME STEP = 5`—*Length of time step (in seconds)*

`NUMBER OF TIME STEPS = 4500`—*Length of simulation in time steps*

`GRAPHIC PRINTOUT PERIOD = 100`—*Period to save to results file*

`LISTING PRINTOUT PERIOD =10`—*Period to print results to screen*

`INITIAL CONDITIONS = 'CONSTANT ELEVATION'`—*Constant elevation over domain at start of simulation*

`INITIAL ELEVATION = 2.25`—*Free surface at start of run (spin-up)*

`PRESCRIBED FLOWRATES = 0; 1.5; 17`—*Flow rates at open boundary, River Leri and River Dyfi*

`LAW OF BOTTOM FRICTION = 5`—*Nikuradse bed roughness scheme*

`FRICTION COEFFICIENT = 0.01`—k_s *(constant for domain)*

`FRICTION COEFFICIENT VARIABLE IN SPACE = YES`—*Activates the subroutine STRCHE*

`TIDAL FLATS = YES`—*Activates 'wetting and drying'*

`MASS-BALANCE = NO`

`TURBULENCE MODEL = 1`—*Constant diffusivity*

`ADVECTION = YES`

`TYPE OF ADVECTION = 1;5`

`ADVECTION OF U AND V = YES`

`ADVECTION OF H = YES`

`NUMBER OF SUB-ITERATIONS FOR NON-LINEARITIES = 1`

`PROPAGATION = YES`

`SOLVER = 1`

`TREATMENT OF THE LINEAR SYSTEM = 2`

`SOLVER OPTION = 2`

`SOLVER ACCURACY = 1.E-4`

`MAXIMUM NUMBER OF ITERATIONS FOR SOLVER = 500`

`PRECONDITIONING = 2`

`MASS-LUMPING ON H = 1.0`

`SPHERICAL COORDINATES = NO`

`BOTTOM SMOOTHINGS = 0`

`ZERO = 1.E-10`

```
CORIOLIS = NO
AIR PRESSURE = NO
WATER DENSITY = 1027
```

Example steering file for `SISYPHE`

`RELEASE=V5P9`—*Version of code to be run*

`GEOMETRY FILE = dyfi.geo`—*Name of mesh file*

`BOUNDARY CONDITIONS FILE = dyfi.conlim`—*Name of 'conlim' file*

`RESULTS FILE = sisyphe_ks2.res`—*Name of SISYPHE results file*

`COMPUTATION CONTINUED = YES`—*Allows continued computation from previous run*

`PREVIOUS SEDIMENTOLOGICAL COMPUTATION FILE = sisyphe_ks2.res`—*Name of previous results file for continuation*

`VARIABLES FOR GRAPHIC PRINTOUTS = U,V,S,H,B,M,N,P,X,E,KS,TOB`—*Choice of output variables for results file (choices below)*

U	*Velocity along x axis*	(ms^{-1})
V	*Velocity along y axis*	(ms^{-1})
S	*Free surface elevation*	(*m*)
H	*Water depth*	(*m*)
B	*Bottom elevation* z_b	(*m*)
M	*Bed-load discharge*	(m^2s^{-1})
N	*Bed-load discharge along x axis*	(m^2s^{-1})
P	*Bed-load discharge along y axis*	(m^2s^{-1})
E	*Bottom evolution*	(*m*)
KS	*Bed friction coefficient* k_s	(*m*)
TOB	*Total bed shear stress* τ_0	(Nm^{-2})

`LAW OF BOTTOM FRICTION = 5`—*Nikuradse relation for* k_s

`FRICTION COEFFICIENT = 0.05`—*Value of* k_s

`MASS-BALANCE = TRUE`

`STEADY CASE = NO`—*SISYPHE uses TELEMAC 2D output every time step*

`MASS-LUMPING = NO`

`SLOPE EFFECT = YES`—*Slope effect of Koch & Flokstra*

`SEDIMENT SLIDE = YES`—*Maximum bed slope angle implemented*

`ZERO = 1e-10`—

`TETA = 0.5`

`WATER DENSITY = 1027`—*Value for* ρ

`CRITICAL EVOLUTION RATIO = 1.0`

`SUSPENSION = NO`—*Deactivation of Advection-Diffusion scheme*
`TYPE OF ADVECTION = 6`
`BED-LOAD TRANSPORT FORMULA = 4`—*Choice of sediment transport formula (choices below)*

1	*Meyer-Peter & Muller*	*(bed load)*
2	*Einstein & Brown*	*(bed load)*
3	*Engelund-Hansen*	*(VERSION 5.3)*
30	*Engelund-Hansen*	*(total load)*
4	*Bijker*	*(total load)*
5	*Soulsby-Van Rijn*	*(total load)*
6	*Hunziker*	*(only for sand grading)*
7	*Van Rijn*	*(bed load)*
8	*Bailard*	*(total load)*
9	*Dibajnia & Watanabe*	*(total load)*

`MEAN DIAMETER OF THE SEDIMENT = 0.00022`—*Value of* D_{50}
`COEFFICIENT FUNCTION OF THE POROSITY = 1.67`—*Value of porosity* n
`BETA = 1.3`—*Slope coefficient* β *for Koch & Flokstra's bed slope formula*

APPENDIX IV

The following is the adapted section of the main `SISYPHE` code (‘`sisyphe.f`’) that was adapted for the MF method of bed level update. Line numbers are included to relate the code segment to the main subroutine, but for reference the following code appears immediately after the bed load and suspended load transport rates have been calculated. Also included is the adaptation to the bed load transport code pertaining to Van Rijn’s sediment transport formula, adapted for a stochastically varying θ_{cr} from Chapter 6. It must be noted that the new sections of code are based on version `V5.9` of the `TELEMAC 2D` and `SISYPHE` sources and therefore may be out of date at the time of reading. The `FORTRAN` code is presented in `CAPS`.

In the section of the `SISYPHE` main `FORTRAN` code adapted for the MF method `E` = total bed evolution, `ZF_C` = bed evolution due to bed load transport, `ZF_S` = bed evolution due to suspended transport and bed load transport, `T1` = working array for sediment slide routine and `I` = integer counter. Between lines `1168` and `1171` the bed evolution is set to the calculated value after the sediment transport routines. A loop from `1:NPOIN` is entered at line `1177` and at line `1178` the total evolution `E` at each grid node is multiplied by the MF coefficient (here set to `705.3456`). Checks are subsequently made that the evolution is not greater than the local water depth `HN`. If so, `E` is set to `HN` and the sediment transport rate `QS` is set to zero.

In the section of `SISYPHE` main FORTRAN code adapted for a stochastic implementation of θ_{cr} `DENS` = ρ, `GRAV` = g, `DM` = D_{50}, `DSTAR` = D_*, `AC` = θ_{cr}, `TETAP` = θ', `CFP` = skin friction C_D, `UCMOY` = $\bar{U}$ and `QSC` = Q_b. The adapted section of the subroutine is between lines `81` and `92`. The uniformly distributed random number `RAND1` from the `FORTRAN 90` function `RAN` is converted via a Box-Müller transformation into the normally distributed random number `RANDN`. The standard deviation of `RANDN` is then set to `0.075` (7%). The critical shields parameter `AC` is then converted to $\theta_{cr} + \delta\theta_{cr}$. This value of θ_{cr} is then used in the calculation of Q_b (line `108`).

Section of the `SISYPHE` main `FORTRAN` code adapted for the MF method

```
!  CALCUL DES EVOLUTIONS SUR CE (SOUS) PAS DE TEMPS
!
    CALL OS(’X=0 ’,X=E)
    IF(CHARR) CALL OS(’X=X ’,X=E,Y=ZF_C)
    IF(SUSP) CALL OS(’X=X ’,X=E,Y=ZF_S)
    IF(SLIDE) CALL OS(’X=X ’,X=E,Y=T1)
!
!  DLM MORPHOLOGICAL FACTOR
!
!  EVOLUTION DES FONDS : NE PAS DEPASSER LA HAUTEUR D’EAU
!
    DO I = 1, NPOIN
        E%R(I)=E%R(I)*705.3456
        IF(E%R(I).GE.HN%R(I)) THEN
            IF(HN%R(I).GE.0.D0) THEN
                E%R(I) = HN%R(I)
            ENDIF
            QS%R(I) = 0.D0
        ENDIF
    ENDDO
```

Section of the `SISYPHE` main `FORTRAN` code adapted for a stochastic implementation of θ_{cr}

```
C1 = DENS * GRAV * DM
C2 = 0.053D0 * SQRT(DM**3.0D0*DENS*GRAV) * DSTAR**(-0.3D0)

DO I = 1, NPOIN
    W=1

    DO
        IF(W.LT.1)EXIT
        RAND1=2.0*RAN(SEED)-1
        RAND2=2.0*RAN(SEED)-1
        W=(RAND1**2)+(RAND2**2)
    ENDDO
    W=SQRT((-2.0*LOG(W))/W)
    RANDN=RAND1*W
    RANDN=RANDN*0.075D0
    AC=AC+(AC*RANDN)
    !  ********************** !
    !  I -ADIM. SKIN FRICTION ! (_IMP_)
    !  ********************** !
    TETAP = 0.5D0 * CFP%R(I) * UCMOY%R(I)**2 / C1
    !  ****************************** !
    !  II - TRANSPORT STAGE PARAMETER ! (_IMP_)
    !  ****************************** !
    IF (TETAP <= AC) THEN
        T=0.D0
    ELSE
        T = (TETAP-AC)/MAX(AC,1.D-06)
    ENDIF
    !  ***************************** !
    !  III - BED LOAD TRANSPORT RATE ! (_IMP_)
    !  ***************************** !
    QSC%R(I) = C2 * (T**2.1D0)

ENDDO
```